INFORMATION TO USERS

This material was produced from a microfilm copy of the original document. While the most advanced technological means to photograph and reproduce this document have been used, the quality is heavily dependent upon the quality of the original submitted.

The following explanation of techniques is provided to help you understand markings or patterns which may appear on this reproduction.

1. The sign or "target" for pages apparently lacking from the document photographed is "Missing Page(s)". If it was possible to obtain the missing page(s) or section, they are spliced into the film along with adjacent pages. This may have necessitated cutting thru an image and duplicating adjacent pages to insure you complete continuity.

2. When an image on the film is obliterated with a large round black mark, it is an indication that the photographer suspected that the copy may have moved during exposure and thus cause a blurred image. You will find a good image of the page in the adjacent frame.

3. When a map, drawing or chart, etc., was part of the material being photographed the photographer followed a definite method in "sectioning" the material. It is customary to begin photoing at the upper left hand corner of a large sheet and to continue photoing from left to right in equal sections with a small overlap. If necessary, sectioning is continued again — beginning below the first row and continuing on until complete.

4. The majority of users indicate that the textual content is of greatest value, however, a somewhat higher quality reproduction could be made from "photographs" if essential to the understanding of the dissertation. Silver prints of "photographs" may be ordered at additional charge by writing the Order Department, giving the catalog number, title, author and specific pages you wish reproduced.

5. PLEASE NOTE: Some pages may have indistinct print. Filmed as received.

Xerox University Microfilms
300 North Zeeb Road
Ann Arbor, Michigan 48106

74-25,810

ALTIERO, Nicholas James, Jr., 1947-
FRACTURE INITIATION AND PROPAGATION IN NONUNIFORM COMPRESSIVE STRESS FIELDS.

The University of Michigan, Ph.D., 1974
Engineering Mechanics

University Microfilms, A XEROX Company, Ann Arbor, Michigan

THIS DISSERTATION HAS BEEN MICROFILMED EXACTLY AS RECEIVED.

FRACTURE INITIATION AND PROPAGATION IN NONUNIFORM COMPRESSIVE STRESS FIELDS

by
Nicholas James Altiero, Jr.

A dissertation submitted in partial fulfillment
of the requirements for the degree of
Doctor of Philosophy
(Aerospace Engineering)
in The University of Michigan
1974

Doctoral Committee:

Associate Professor David L. Sikarskie, Chairman
Associate Professor Anthony G. Atkins
Professor Joe G. Eisley
Associate Professor John E. Taylor
Associate Professor Alan S. Wineman

ACKNOWLEDGMENTS

The author wishes to express his sincere appreciation to Professor David L. Sikarskie for his guidance during the course of this investigation. The advice of Professors J.G. Eisley, J.E. Taylor, A.S. Wineman and A.G. Atkins, members of the doctoral committee, is also appreciated. The typing of the manuscript was done by Ms. Margaret Fillion.

Financial support for this research was provided by the National Science Foundation under grant numbers GK-17101 and GK-37289 and the Horace H. Rackham School of Graduate Studies under grant number 360283.

Special thanks to my family and to Linda for their encouragement and for the genuine interest they have always shown in my work.

TABLE OF CONTENTS

		Page
ACKNOWLEDGMENTS		ii
LIST OF TABLES		iv
LIST OF FIGURES		v
LIST OF APPENDICES		viii
LIST OF SYMBOLS		ix
INTRODUCTION		1
CHAPTER I -	PRELIMINARIES	14
I.1.	Introductory Remarks	14
I.2.	The Fracture Criterion	15
I.3.	An Integral Equation Method	17
CHAPTER II -	FRACTURE ANALYSIS	26
II.1.	Introductory Remarks	26
II.2.	Stress Analysis	30
II.3.	Fracture Analysis - Linear Criterion	39
II.4.	Numerical Results and Discussion	42
II.5.	Fracture Analysis - Nonlinear Criterion	55
II.6.	Numerical Results and Discussion	62
CHAPTER III -	EXPERIMENT	67
III.1.	Introductory Remarks	67
III.2.	The Experiment	69
III.3.	Theoretical Results	78
III.4.	Experimental Results	83
CLOSURE		89
APPENDICES		91
REFERENCES		123

LIST OF TABLES

Table		Page
2.1	The Exact Solution of the Problem of Figure 8 . .	34
2.2	Dependence of Integral Method Solution on Boundary Cut-off	36
2.3	Integral Method Solution Using Mesh Spacing of Figure 9	38
2.4	Fracture Initiation Results for Blair Dolomite and Quartzite; m = 5, μ_f = 0.0	63
3.1	Experimental Results (Uniform Displacement) . .	84
C.1	Points Obtained from Mohr Envelope of Blair Dolomite	107
C.2	Points Obtained from Mohr Envelope of Quartzite .	108
C.3	Coefficients of Least Squares Polynomial Fits for Blair Dolomite and Quartzite	109
E.1	Traction Components on Truncated Edge Due to Uniform Displacement Condition	118
E.2	Comparison of Finite Element Solution and Integral Equation Solution at Selected Points in Test Geometry	122

LIST OF FIGURES

Figure		Page
1.	Mohr Fracture Envelope	3
2.	Crack Propagation From a Critical Griffith Crack .	8
3.	Mohr Envelope and Modified Griffith Criterion for Norite	11
4.	Relationship Between Axial Stress and Axial, Lateral and Volumetric Strain for Quartzite in Uniaxial Compression	16
5.	Real Body "Embedded" in Fictitious Half Planes .	19
6.	Line Load Acting on the Boundary of a Half Plane at the Point of Tangency to the Real Body	21
7.	Boundary Value Problem Geometry	27
8.	Stresses in a Quarter Plane due to a Line Load Applied at the Apex	32
9.	Boundary Mesh Spacing	37
10.	Coulomb-Mohr Fracture Envelope	41
11.	Location and Direction of Critical Cracks; $\theta = 45^{\circ}$, $\mu_f = 0.0$	43
12.	Location and Direction of Critical Cracks; $\theta = 45^{\circ}$, $\mu_f = 0.1$	44
13.	Dependence of Fracture Initiation on Traction Distribution for $\theta = 45^{\circ}$, $\mu_f = 0.0$	45
14.	Dependence of Fracture Initiation on Traction Distribution for $\theta = 45^{\circ}$, $\mu_f = 0.1$	47
15.	Effect of Wedge Angle on Fracture Initiation; $m = 5$, $\mu_f = 0.0$	48
16.	Contour Map of the Fracture Function $F(\sigma_1, \sigma_2; \mu)$; $m = 5$, $\mu_f = 0.0$, $\mu = 0.6$, $\theta = 45^{\circ}$ . .	50

17. Enlarged View of Fracture Initiation Region; $m = 5$; $\mu_f = 0.0$, $\mu = 0.6$, $\theta = 45^o$ 51

18. Value of Fracture Function along the Fracture Path 54

19. Mohr Envelopes for Blair Dolomite and Quartzite . 56

20. Fracture Initiation Points for Blair Dolomite and Quartzite; $m = 5$, $\mu_f = 0.0$, $\theta = 45^o$ 58

21. Contour Map for Blair Dolomite at Zero Confining Pressure; $m = 5$, $\mu_f = 0.0$, $\theta = 45^o$ 64

22. Contour Map for Blair Dolomite at Moderate Confining Pressure (3 kb); $m = 5$, $\mu_f = 0.0$, $\theta = 45^o$ 65

23. Test Specimens for Determination of Material Properties of Plaster 71

24. Stress-Strain Curve for Plaster 72

25. Coulomb-Mohr Fracture Envelope for Plaster . . 74

26. Plaster Model in Loading Fixture 76

27. Schematic Diagram of Recording System 77

28. Contour Map for Plaster; Uniform Displacement of Truncation Edge 80

29. Contour Map for Plaster; Uniform Traction Distribution along Truncation Edge 82

30. Typical Force-Displacement Plot of Uniform Displacement Test on Plaster Model 85

31. Photograph of Complete Chip. 87

B-1. Refinement of Field in Vicinity of F_{max} (K_{min}) . . 105

E-1. Node and Element Labels for Finite Element Analysis of Mixed Boundary-Value Problem 116

E-2. Enlargement of Region from Figure E-1 117

E-3. Traction Distribution on BA Due to Uniform Displacement Condition 119

E-4 Location of Points for Comparison of Finite Element Solution and Integral Method Solution . . 120

LIST OF APPENDICES

Appendix		Page
A	A Necessary and Sufficient Condition for the Stress Normal to a Plane in a State of Plane Strain to be the Intermediate Principal Stress . .	91
B	"Fracture" Computer Program - Linear Fracture Envelope	94
C	Polynomial Fits of $\overline{\sigma}(\overline{\sigma}_m)$ and $\overline{\tau}(\overline{\sigma}_m)$ for Blair Dolomite and Quartzite	106
D	"Fracture" Computer Program - Nonlinear Fracture Envelope	110
E	Finite Element Solution to Mixed Boundary-Value Problem	115

LIST OF SYMBOLS

C	$\bar{\tau}$ - intercept of linear Coulomb-Mohr envelope
μ	slope of linear Coulomb-Mohr envelope
$\bar{\sigma}$, σ	normal stress, dimensionless normal stress on critical plane
$\bar{\tau}$, τ	shear stress, dimensionless shear stress on critical plane
$\bar{\sigma}_{1,2}$, $\sigma_{1,2}$	principal stresses, dimensionless principal stresses in plane ($\bar{\sigma}_1 > \bar{\sigma}_3 > \bar{\sigma}_2$)
S_t	tensile strength
ψ_c	angle between direction of $\bar{\sigma}_2$ and critical Griffith plane
S_c	compressive strength
$\bar{\mu}$	coefficient of friction between faces of Griffith crack
$\bar{\sigma}_c$	stress necessary to close Griffith crack
$G_{ij;q}$	ij th stress component due to a unit line load acting in the q direction (Green's function); with respect to local coordinates
$\Phi_{ij;q}$	Green's function with respect to global coordinates
$\bar{\sigma}_{ij}, \sigma_{ij} = \frac{\bar{\sigma}_{ij} L}{P}$	stress components, dimensionless stress components
t_q , t_q^*	real, fictitious traction components in the q direction
s	measure of length along boundary
x, y	coordinates in integral method stress analysis and in fracture analysis
P, P_1	field and boundary points, respectively
$\bar{B}$	bounding surface of region
n_i	direction cosines of boundary

$d\underset{\sim}{P}^*$	line load acting on boundary of half plane
$\underset{\sim}{\bar{r}}$	dimensional vector defining distance from point of application of line load
$\underset{\sim}{e}_i$	unit vector in i-direction
$\bar{r}, \phi$	coordinates on half plane
$\bar{r}_x, \bar{r}_y$	x,y distances from field point to boundary point
$r_x, r_y = \frac{\bar{r}_x}{L}, \frac{\bar{r}_y}{L}$	dimensionless x,y distances from field to boundary points
P	total vertical line load on truncated quarter plane; characteristic load for problem
L	length of truncated boundary, characteristic length for problem
p_q, p_q^*	real, fictitious dimensionless traction components in the q direction
$S = s/L$	dimensionless length measure along boundary
P_{xi}, P_{yi}	real line load components in the i th interval
P_{xi}^*, P_{yi}^*	fictitious line load components in the i th interval
N	number of boundary subdivisions
r_{xij}, r_{yij}	x,y distances between subdivisions i and j
A_{ij}, B_{ij}, C_{ij}	coefficients in linear system of equations generated by integral equation method
α	convergence parameter
P_i	fracture initiation load
P_f	chip formation load
p	scalar reference pressure
ξ	length coordinate along slanted face BA of truncated quarter plane
μ_f	coefficient of friction between wedge-shaped indentor and truncated quarter plane

m	traction "form" parameter
ϕ_f	external friction angle ($\mu_f = \tan \phi_f$)
θ	half wedge angle (truncation angle)
Q	line load applied at apex of quarter plane
ρ , δ	coordinates on quarter plane
η , ξ	coordinates on quarter plane
$\psi_{1,2}$	angles between x-axis and normals to critical planes
$\gamma_{1,2}$	angles between x-axis and normals to principal planes
ϕ	angle of Coulomb-Mohr envelope with respect to x axis ($\mu = \tan \phi$)
$F(\sigma_1, \sigma_2 ; \mu)$	"fracture function" of linear theory
$\beta = CL/P$	dimensionless "cohesion"
F_{max}	maximum of linear fracture function; defines point of fracture initiation in linear theory
$\hat{s}$	length measure along fracture path
$\hat{S} = \hat{s}/L$	dimensionless length measure along the fracture path
$\mu(\bar{\sigma}_m)$	slope of linear envelope tangent to the Mohr envelope at the point at which the mean stress is $\bar{\sigma}_m$
$C(\bar{\sigma}_m)$	$\bar{\tau}$ - intercept of a linear envelope tangent to the Mohr envelope at the point at which the mean stress is $\bar{\sigma}_m$
$\bar{\sigma}_m = \frac{\bar{\sigma}_1^T + \bar{\sigma}_2^T}{2}$	mean stress
α_i	coefficients in polynomial fit for $\bar{\tau} = \bar{\tau}(\bar{\sigma}_m)$
β_i	coefficients in polynomial fit for $\bar{\sigma} = \bar{\sigma}(\bar{\sigma}_m)$
$\bar{\sigma}_{1,2}^T$	total principal stresses ($\bar{\sigma}_1^T > \bar{\sigma}_2^T$)
$\bar{\sigma}^H$	hydrostatic stress

$\phi(\bar{\sigma}_m)$	$\mu(\bar{\sigma}_m) = \tan\phi(\bar{\sigma}_m)$
$K(\bar{\sigma}_1^T, \bar{\sigma}_2^T; \mu(\bar{\sigma}_m), C(\bar{\sigma}_m))$	"fracture function" of nonlinear theory
K_{min}	minimum of nonlinear fracture function; defines point of fracture initiation in nonlinear theory
C_A	asymptotic value of Mohr envelope
E	Young's modulus
ν	Poisson's ratio
$\tilde{x}, \tilde{y}$	coordinates for finite element stress analysis
Δ	depth of chip in experimental problem

INTRODUCTION

In 1638, Galileo proposed a "new science" to be concerned with "the resistance which solid bodies offer to fracture" [1]. In the past three centuries, there have been a large number of contributors to this science, but the phenomenon of fracture is still not wholly understood. For example, fracture in bodies subjected to compressive stresses received relatively little attention until the past decade, and fracture in the presence of non-uniform compressive stress fields has not been dealt with at all. It is the purpose of this dissertation to develop a theory applicable to fracture initiation and propagation in a non-uniform compressive stress field.

The first criterion of fracture was postulated in 1776 by C.A. Coulomb [2]. Coulomb suggested that fracture would occur in a solid body when the shear stress on some plane in that body was large enough to overcome the sum of the "cohesive strength," C, and the frictional stress, $-\mu\bar{\sigma}$, caused by the compressive stress, $-\bar{\sigma}$, normal to that plane. Thus Coulomb's criterion can be expressed as:

$$|\bar{\tau}| = C - \mu\bar{\sigma}$$

This criterion is sometimes referred to as the Coulomb-Navier criterion, possibly due to Navier's treatment of this theory some fifty years later [3].

In 1900, Mohr proposed a criterion of the form [4]:

$$|\bar{\tau}| = f(\bar{\sigma}) \qquad (1)$$

where $f(\overline{\sigma})$ would be determined experimentally from a series of triaxial tests. The Mohr's circle describing the state of stress at fracture is plotted for each test. The function $f(\overline{\sigma})$ is then defined by the envelope which is tangent to the set of Mohr's circles determined in this way (see figure 1). Note that in the case of the Mohr envelope being linear, it can be written as:

$$|\overline{\tau}| = C - \mu \overline{\sigma} \tag{2}$$

which is identical in form to the Coulomb criterion. Thus in the linear case, the criterion is referred to as the Coulomb-Mohr criterion whereas the more general non-linear envelope is called the Mohr criterion.

The first triaxial tests were conducted by von Kármán [5] and Böker [6] in 1911 and 1915, respectively. These tests were performed on cylindrical specimens of marble and sandstone. The applied axial loads were compressive. They concluded that the fracture strengths could be approximated by Mohr envelopes.

The Mohr criterion is empirical. Thus, although it is applicable, quantitatively, in predicting macroscopic fracture, it contributes little to an understanding of the mechanism of fracture. In papers published in 1921 and 1924, A.A. Griffith proposed a fracture mechanism [7,8] which presently enjoys widespread acceptance. Griffith hypothesized that materials contain microscopic flaws (now referred to as "Griffith cracks") at which fracture initiates. Assuming that these flaws are elliptical in shape, Griffith employed Inglis' solution [9] for the stress

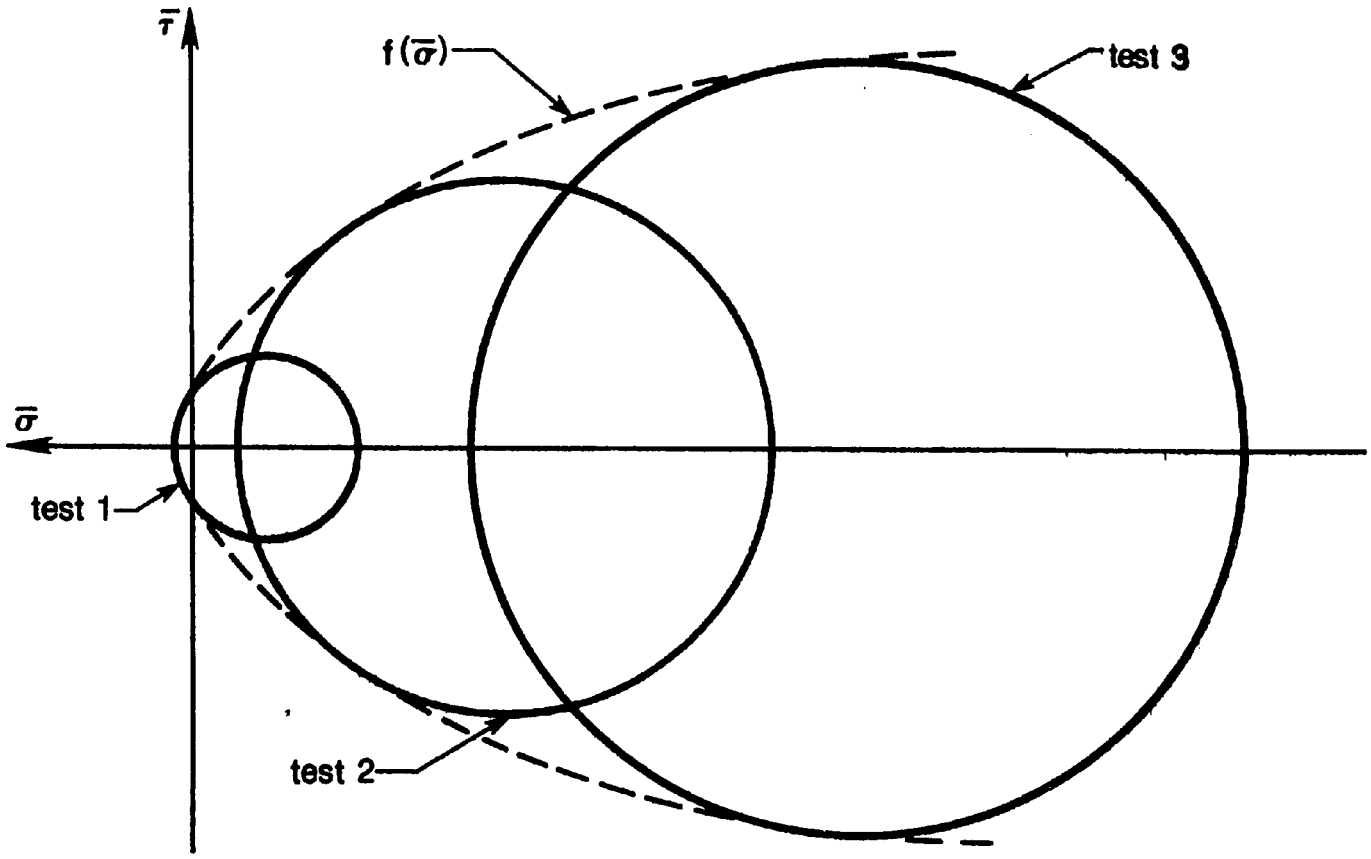


FIGURE 1 MOHR FRACTURE ENVELOPE

distribution about an elliptic slit in a plane elastic body to show that stress concentrations develop near the crack tips. Based on energy considerations, he derived a criterion for fracture initiation at these tips. For a predominately compressive stress field ($\bar{\sigma}_1 / \bar{\sigma}_2 \geq -1/3$ everywhere), this criterion is

$$(\bar{\sigma}_1 - \bar{\sigma}_2)^2 / (\bar{\sigma}_1 + \bar{\sigma}_2) = -8 S_t \tag{3}$$

where $\bar{\sigma}_1 > \bar{\sigma}_3 > \bar{\sigma}_2$ algebraically and S_t is the tensile strength of the material. Griffith assumed that fracture is independent of intermediate stress, $\bar{\sigma}_3$ (note that in Mohr's theory this assumption is inherent). Griffith also determined that the condition (3) would be satisfied at a preferentially-oriented flaw in the material inclined at the angle ψ_c with respect to $\bar{\sigma}_2$ defined by

$$\cos 2\psi_c = (\bar{\sigma}_1 - \bar{\sigma}_2) / 2 (\bar{\sigma}_1 + \bar{\sigma}_2) \tag{4}$$

Murrell [10] later demonstrated that the fracture criterion described by equations (3) and (4) can be written in the form of a parabolic Mohr's envelope

$$\bar{\tau}^2 + 4 S_t \bar{\sigma} = 4 S_t^2 \tag{5}$$

kindling the hope that the two criteria are, in fact, equivalent. However, the Griffith theory yields a very curious result. If, in equation (3), the case of $\bar{\sigma}_1 = 0$, $\bar{\sigma}_2 = -S_c$ is considered where S_c is the material's compressive strength, it follows that

$$S_c = 8 S_t$$

Thus Griffith's theory predicts that, regardless of material, the compressive strength is eight times the tensile strength; a result which is obviously incorrect.

This discrepancy led F.A. McClintock and J.B. Walsh, in 1962, to a modification of Griffith's theory [11]. They suggested that under compressive stresses, the "Griffith cracks" in the material close and that Griffith should therefore have considered friction between the crack faces. Based on this consideration, a new criterion was derived (again for $\bar{\sigma}_1/\bar{\sigma}_2 \geq -1/3$):

$$\bar{\mu}(\bar{\sigma}_2 + \bar{\sigma}_1 - 2\bar{\sigma}_c) + (\bar{\sigma}_1 - \bar{\sigma}_2)(1+\bar{\mu}^2)^{\frac{1}{2}} = 4S_t(1 - \bar{\sigma}_c/S_t)^{\frac{1}{2}}$$

where $\bar{\sigma}_c$ is the stress necessary to close a "Griffith crack" and $\bar{\mu}$ is the coefficient of friction between the crack faces (not to be confused with the slope, μ, of the Coulomb-Mohr criterion).

Brace [12] determined that the stress, $\bar{\sigma}_c$, required to close a "Griffith crack" is extremely small and thus can be quantitatively neglected. The criterion then reduces to:

$$\bar{\mu}(\bar{\sigma}_1 + \bar{\sigma}_2) + (\bar{\sigma}_1 - \bar{\sigma}_2)(1+\bar{\mu}^2)^{\frac{1}{2}} = 4S_t \tag{6}$$

This can be re-written in the form of a Mohr envelope:

$$|\bar{\tau}| = 2S_t - \bar{\mu}\bar{\sigma} \tag{7}$$

which again led to the erroneous belief that the two criteria are equivalent.

If a range of $\bar{\mu}$ is considered, say $.1 \leq \bar{\mu} \leq 1.0$, equation (6) yields

$$4.4S_t \leq S_c \leq 10S_t$$

Although this is a more realistic result than that obtained by Griffith, it does not compare favorably to experimental results. In general, the modified Griffith theory predicts a ratio of compressive strength to tensile strength considerably less than what is determined in the lab [13] (in the case of many rocks, this ratio has been found to be two or three times larger than predicted by the modified Griffith theory). Thus, although the modified Griffith theory provides a plausible (and generally accepted) mechanism of fracture initiation, it fails to predict macroscopic fracture quantitatively in a compressive stress field. Conversely, the Mohr envelope provides a reasonable criterion for macroscopic fracture in compression, but is empirical in nature and thus provides no understanding of the mechanism involved. This apparent dilemma led investigators to undertake two experimental studies. One of these studies was a reassessment of the triaxial test. Cook and Fairhurst [14, 15] asserted that triaxial test results obtained previously were erroneous since the stress distribution in the specimens was not uniform. They suggested load platens with the same lateral expansion ν/E as the specimens. In 1964, Brace [16] proposed a "dogbone" specimen to be used for triaxial testing. The thinner middle section was loaded hydraulically producing both radial compression and axial tension in this section of the specimen. The specimen was also subjected to a compressive axial load. Thus tests could be performed for a range of axial stresses spanning tension and compression. For

each material, Brace ran a series of tests (varying the confining pressure). He determined that the fracture data found in this way could be accurately expressed by a Mohr envelope. These envelopes, contrary to the modified Griffith theory, were not necessarily linear. Furthermore, Brace found the damage to be extensive throughout the specimen thus confirming the uniformity of the stress field. Perhaps the most significant observation made by Brace is that this extensive damage appeared in the specimen prior to actual failure. This damage appeared as a system of micro-cracks growing out of grain boundaries. Brace suggested that these micro-cracks ultimately coalesced to form the macroscopic fracture surface. This coalescence mechanism appeared in the compressive fields only. In tension, the ultimate fracture appeared to grow from a single crack. Finally, he observed that prior to ultimate failure, the volume of the specimen relative to elastic changes tended to increase.

Concurrent with the triaxial test experiments was another interesting study. In 1963, Brace and Bombolakis [17] cut an elliptical slit inclined at approximately 30° to the axis of compression in a photoelastic material. Upon increasing the compressive load, they observed that crack growth initiated near the ends of the slit initially propagating normal to the slit faces (see figure 2). As the compression was further increased, the crack propagated in a stable manner, slowly aligning with the direction of the applied compressive stress. Hoek and Bieniawski [18] performed similar experiments in biaxial compression

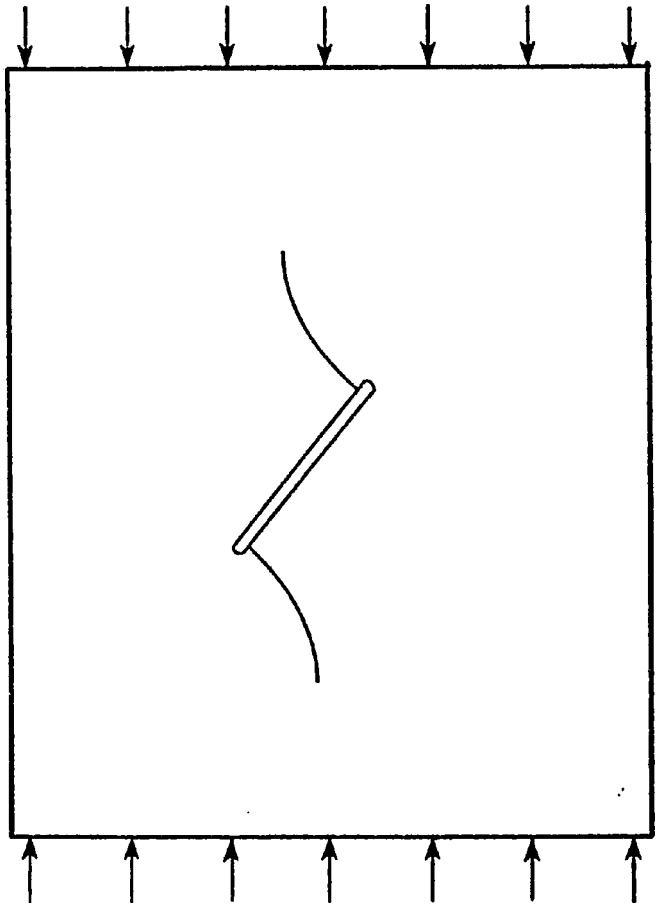


FIGURE 2 CRACK PROPAGATION FROM A CRITICAL GRIFFITH CRACK

and found the same results where here the final alignment was with the larger of the principle compressive stresses. They also determined that fracture initiation near the tips of such a flaw could be predicted by the modified Griffith criterion. They then considered various "arrays" of slits and found that propagations from parallel "Griffith cracks" tend to coalesce. Propagation from "Griffith cracks" alligned "end-to-end" did not coalesce. Bieniawski, in a later paper [19], studied crack propagation from flaws in more detail. He determined that these cracks grow in a stable manner from flaw tips until a critical energy release, at which point they lose stability and grow rapidly to coalesce with other cracks.

In 1966, Brace et. al. [20] measured the volume changes of specimens during deformation in triaxial compression up to failure. They determined that at one-third to two-thirds of the fracture stress, the volume of the specimens increased relative to elastic volumetric strain. This effect, termed dilatancy, represents an increase in the porosity of the material and was traced to open cracks which formed generally parallel to the direction of maximum compression. This study and experiments by Cook [21] showed that this dilatancy is pervasive throughout a sample loaded uniformly. Thus, according to these results, the compressive stress necessary to cause failure of a "dogbone" compression specimen is approximately two to three times the compressive stress necessary to initiate micro-damage in the specimen. Thus the "compressive strength" predicted by the modified

Griffith theory is actually the compressive stress required to initiate damage and is quantitatively one-third to two-thirds of the actual compressive strength of the material. This apparently explains the discrepancy between the modified Griffith theory and experimental results. The implications of this with regard to a fracture initiation criterion will be discussed further in Chapter I. In figure 3, the Mohr criterion and modified Griffith "criterion" are shown for Norite.

Finally, in 1972, Brace et. al. [22], employing a new technique, were able to observe "Griffith flaws" in several rock specimens. They found that grain boundaries are preferred sites for these cracks but that they also exist within the grains themselves.

Two excellent review articles have been published recently by Paul [23] and Obert [24] and the reader is referred to them for more detailed accounts of the history of this topic.

At this point, the process of fracture in a uniform multiaxial stress field is fairly well understood. The Griffith theory provides a description of the fracture mechanism and the Mohr criterion appears to adequately predict the occurrence of macroscopic fracture and strength failure. In this dissertation a theory is advanced, the intent of which is to extend this understanding of the fracture process to non-uniform compressive stress fields applicable to the solution of boundary-value problems.

In Chapter I, two very important preliminary topics are discussed. First, it is shown that, in boundary-value problems, the

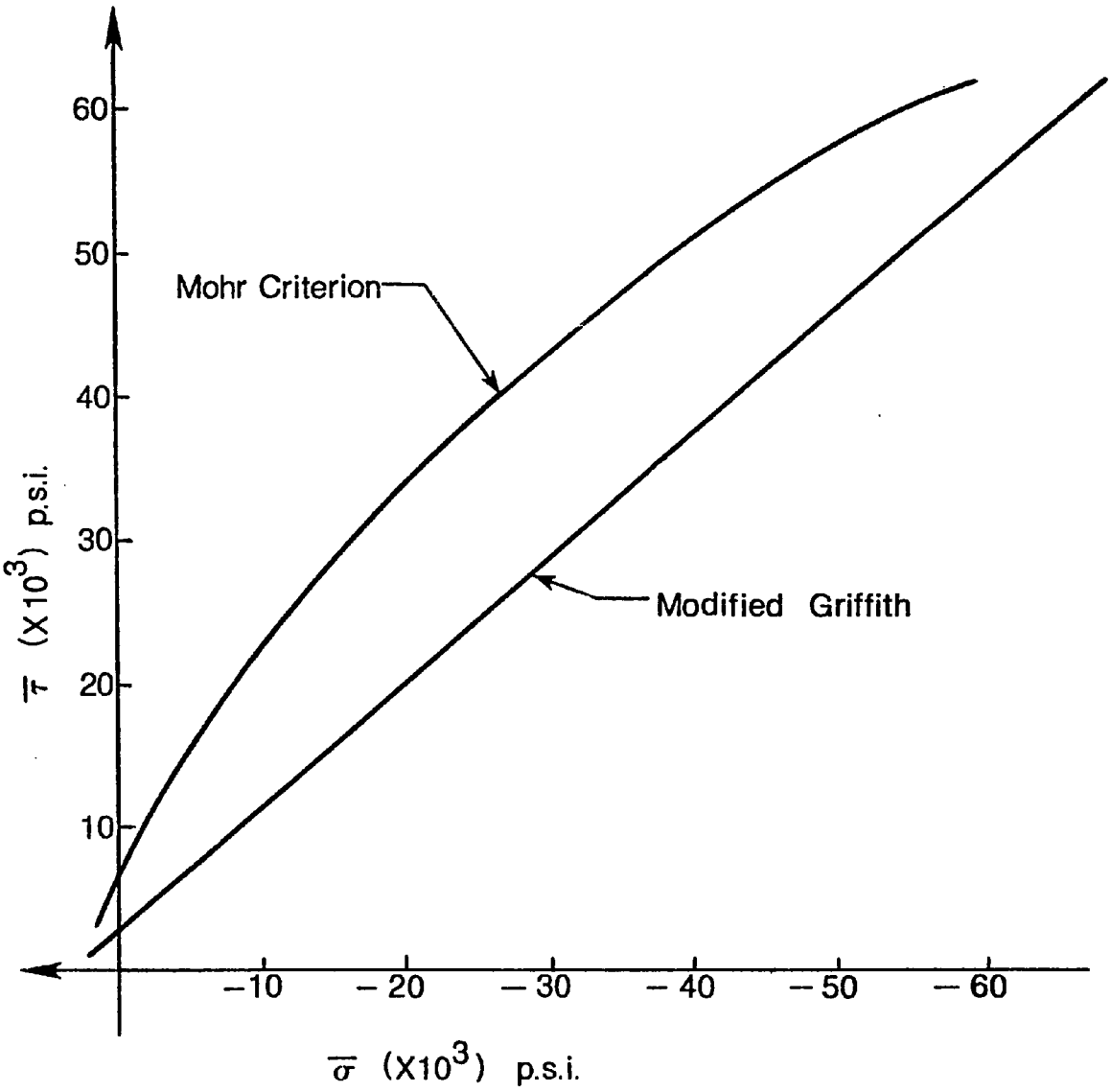


FIGURE 3 MOHR ENVELOPE AND MODIFIED GRIFFITH CRITERION FOR NORITE, following [19]

modified Griffith theory as elaborated by Brace, Bieniawski, et. al. provides a most reasonable model of the mechanism of the fracture process. However, macroscopic fracture is defined by crack coalescence and, therefore, Mohr's criterion is applicable to macroscopic fracture initiation. Second, a method for stress field determination is presented which involves the solution of a coupled set of integral equations [25, 26]. It is shown that this method is more compatible with this type of analysis than the finite element method.

In Chapter II, the theory is outlined and applied to a specific boundary-value problem. This problem has been motivated by the familiar "penetration problems" of rock mechanics [27]. The solution of such a problem first requires a determination of the stress field. The integral equation method is employed and its accuracy is assessed by comparison to a similar problem for which an exact solution is available. Once the stresses are known, a fracture analysis is done. Based on Mohr's criterion, a "fracture function" is defined, a contour map of which can be drawn throughout the body. The "peak" of this fracture function defines the location of fracture initiation. Crack growth is initiated at several points in the vicinity of this "peak" and growth is in accordance with the modified Griffith theory. Crack coalescence marks the onset of macroscopic fracture propagation. It is shown that this propagation is directed along the minimum gradient of the fracture function. Clearly, the presence of this fracture and the neighboring damage alters the original stress field. Thus, accurate

determination of subsequent growth of the fracture surface would require a continuous modification of the stresses as the fracture propagation proceeds. At present, such a modification is not possible since there is as yet no measure of the effect of such a process on the stresses in the undamaged regions of the body. However, a fracture function based on the stress field of the pre-fractured body is used to approximate ultimate fracture behavior and to gain further insight into the process itself. This fracture function provides estimates of both "damaged region" and "relative fracture velocity," useful concepts for predicting ultimate fracture behavior.

A parametric study is first presented using the Coulomb-Mohr (linear Mohr) criterion to determine the effects of load, geometric and material parameters. The analysis is then expanded to include the more general non-linear Mohr envelope. An iterative technique based on a series of linear fracture envelopes is employed. The problem is considered for two rock materials and the effects of confining pressure are included.

Finally, in Chapter III, an experimental study is outlined in which specimens, trapezoidal in shape, were loaded in compression. The theory is employed to predict fracture initiation location and load and to estimate the final fracture path and ultimate load. These values are then measured experimentally and are found to be in excellent agreement with the theoretical predictions.

CHAPTER I

PRELIMINARIES

1. Introductory Remarks

The solution of a boundary-value problem in fracture mechanics involves several stages. It is first necessary to determine the stress field. Then by comparing the stress field with a fracture criterion, the region is searched for the location of the fracture initiation and the initial direction of the fracture propagation. The final step is to trace the path of the stable fracture growth up to the point of instability and ultimate rupture of the body. The applied loading at the moment of the instability is usually defined as the ultimate fracture load.

In the analysis which will be presented in Chapter II, the following results will be obtained: a determination of the pre-fracture stress field, the location of fracture initiation, the fracture initiation load, the direction of initial fracture propagation, an approximation of the final fracture geometry, and an approximation of the ultimate fracture load.

To perform this analysis, two basic tools are required: a fracture criterion and a method for the determination of the stress field. The fracture criterion on which the "fracture function" of Chapter II is based is Mohr's criterion. The significance of this criterion is discussed in section I.2. The method used for the stress determination is an integral equation method [25, 26], which is developed in section I.3.

2. The Fracture Criterion

Mohr fracture envelopes have been used extensively in the study of fracture of brittle materials [23]. In general, these envelopes are developed phenominologically, i.e., the Mohr's circles to which the envelope is tangent are defined by "strength failure" of cylindrical test specimens under axial load and varying confining pressure. A criterion developed in this way does not define fracture initiation in the Griffith sense. It has been shown, however, [16, 19] that it is not fracture initiation in the Griffith sense but rather crack coalescence which defines the onset of macro-fracture.

In order to understand the basic fracture mechanism, it is useful to consider the lateral, volumetric and axial strain plotted versus axial stress. In figure 4, such a plot is shown for quartzite under zero confining pressure [19]. Of particular significance is the volumetric strain curve. This is interpreted as follows. Axial stresses in the vicinity of point A are sufficient to initiate growth at a number of critically oriented Griffith cracks. The stress field is assumed to be globally uniform* (uniaxial) and the Griffith flaws are randomly distributed being located, for example, at grain boundaries [22]. As the stress increases, these cracks continue to grow. Such growth is indicated by a deviation from linearity of the volumetric strain, i.e.,

---

*Most compression tests, in fact, produce non-uniform "global" stress states. The test specimens introduced by Brace [16] and used in [19] closely approximate a uniform stress state as evidenced by the uniform damage distribution in the specimen.

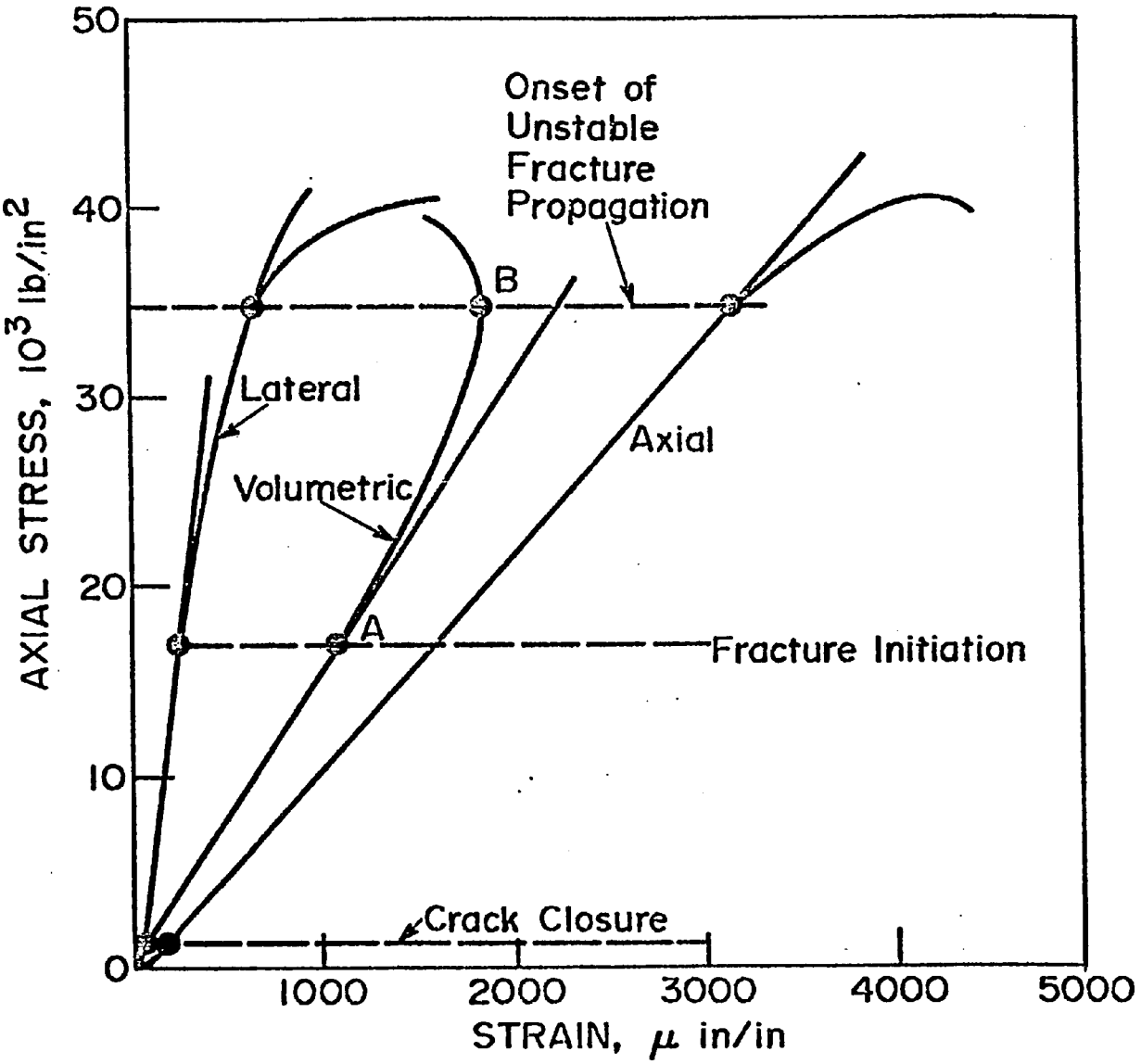


FIGURE 4 RELATIONSHIP BETWEEN AXIAL STRESS AND AXIAL, LATERAL, AND VOLUMETRIC STRAIN, FOR QUARTZITE IN UNIAXIAL COMPRESSION, following [19]

dilatancy. This dilatancy is an increase in porosity which is a reflection of internal damage resulting from crack growth. Further increase in stress begins to produce coalescence of these cracks. For stresses beyond point B, crack coalescence is extensive throughout the specimen, as evidenced by large increases in dilatancy. This widespread damage is preliminary to the coalescence which forms the final fracture surface resulting in strength failure of the specimen. Thus the Griffith theory gives the stress level at which preferentially oriented cracks begin to grow while the final Mohr envelope indicates when such cracks have sufficiently coalesced to cause final strength failure. In the boundary value problem under consideration (non-uniform global stress field) of interest is the onset of the fracture forming the resultant chip. This fracture initiation is characterized by crack coalescence (as differentiated from initiation in the Griffith sense) and is most closely represented by the material strength failure (Mohr fracture envelope).

3. An Integral Equation Method

A method for stress field determination [25, 26] is presented here which will be used in the fracture analysis. The accuracy of this method is assessed in section II.2 and it is shown to have certain advantages over the finite element method in this type of analysis. In Appendix E, solutions are obtained for a specific boundary-value problem using both the Integral Equation Method and the Finite Element Method and the results are compared.

The development of the Integral Equation Method follows.

The region of interest is "embedded" in a region for which the Green's function $G_{ij;q}$ is known. $G_{ij;q}$ represents the ij th stress component at field point P due to a unit line force in the q direction at boundary point P_1 in a region, the surface of which contains and is tangent to the real surface at P_1, see figure 5. The importance of this tangency requirement will be evident later when it will lead to Fredholm integral equations of the second kind. Without the tangency requirement, Fredholm equations of the first kind would be generated and the subsequent solution would be considerably more difficult. At this tangent point, an unknown fictitious line load is applied creating a stress field in the entire fictitious region. The fictitious region is then translated and rotated so that it is tangent to the real body at some other boundary point P'' and another fictitious line load is applied. This process is repeated for all boundary points of the real body and the resultant stress field in this body is simply the sum of these contributions. It is noted, however, that the coordinates in the function $G_{ij;q}$ are translated and rotated with respect to a fixed coordinate system in the body, this translated form being referred to as $\phi G_{ij;q}$. Thus the stress components in the body can be expressed as:

$$\bar{\sigma}_{ij}(P) = \int_{\bar{B}} \phi G_{ij;q}(P, P_1)\, t_q^*(P_1)\, ds \qquad (1.1)$$

$$i,j = x,y$$

where P, P_1 are field and boundary points respectively, $\bar{B}$ is the bounding surface of the real body and s is a measure of length along $\bar{B}$.

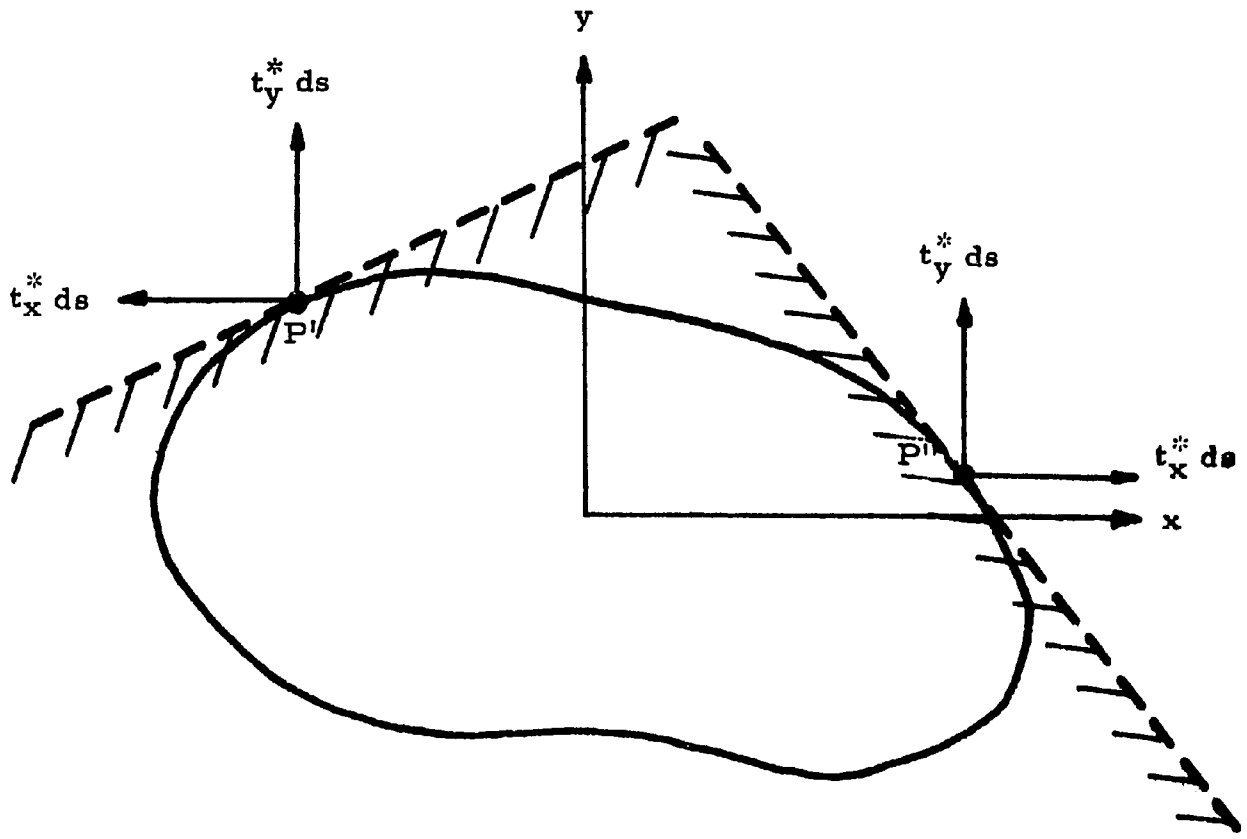


FIGURE 5 REAL BODY "EMBEDDED" IN FICTITIOUS HALF PLANES

This stress field satisfies the equations of elasticity but does not yet satisfy the boundary conditions on $\overline{B}$, namely:

$$\overline{\sigma}_{ij}\, n_j = t_i \qquad \text{on } \overline{B} \tag{1.2}$$

where n_j, t_i are the components of the unit normal and traction vector respectively. Substituting (1.1) into (1.2) and extracting the singularity that occurs when P and P_1 coincide:

$$t_i^*(P) + \int_{\overline{B}} \Phi_{ij;q}(P, P_1)\, t_q^*(P_1)\, n_j(P)\, ds = t_i(P) \tag{1.3}$$

$$i = x, y \qquad P \text{ on } \overline{B}$$

where t_x^*, t_y^* represent "fictitious" x,y traction components along $\overline{B}$. To complete the solution, equation (1.3) is solved for the "fictitious" tractions. These tractions are then substituted into equation (1.1) and the stresses are computed.

A convenient choice for the fictitious region is the half-plane. Consider a line load $d\underset{\sim}{P}^*$ acting on the boundary of a half-plane as in figure 6. The stress components at a point a distance $\underset{\sim}{\overline{r}}$ from the point of application of this load are given by the Flamant-Boussinesq solution [28]:

$$d\overline{\sigma}_{rr} = -\frac{2}{\pi}\,\frac{d\underset{\sim}{P}^* \cdot \underset{\sim}{\overline{r}}}{\overline{r}^2} \qquad d\overline{\sigma}_{r\phi} = d\overline{\sigma}_{\phi\phi} = 0 \tag{1.4}$$

The stress components at this point with respect to a cartesian system can be expressed as

$$\begin{aligned} d\overline{\sigma}_{xx} &= d\overline{\sigma}_{rr}\,(\underset{\sim}{e}_r \cdot \underset{\sim}{e}_x)^2 \\ d\overline{\sigma}_{yy} &= d\overline{\sigma}_{rr}\,(\underset{\sim}{e}_r \cdot \underset{\sim}{e}_y)^2 \\ d\overline{\sigma}_{xy} &= d\overline{\sigma}_{rr}\,(\underset{\sim}{e}_r \cdot \underset{\sim}{e}_x)\,(\underset{\sim}{e}_r \cdot \underset{\sim}{e}_y) \end{aligned} \tag{1.5}$$

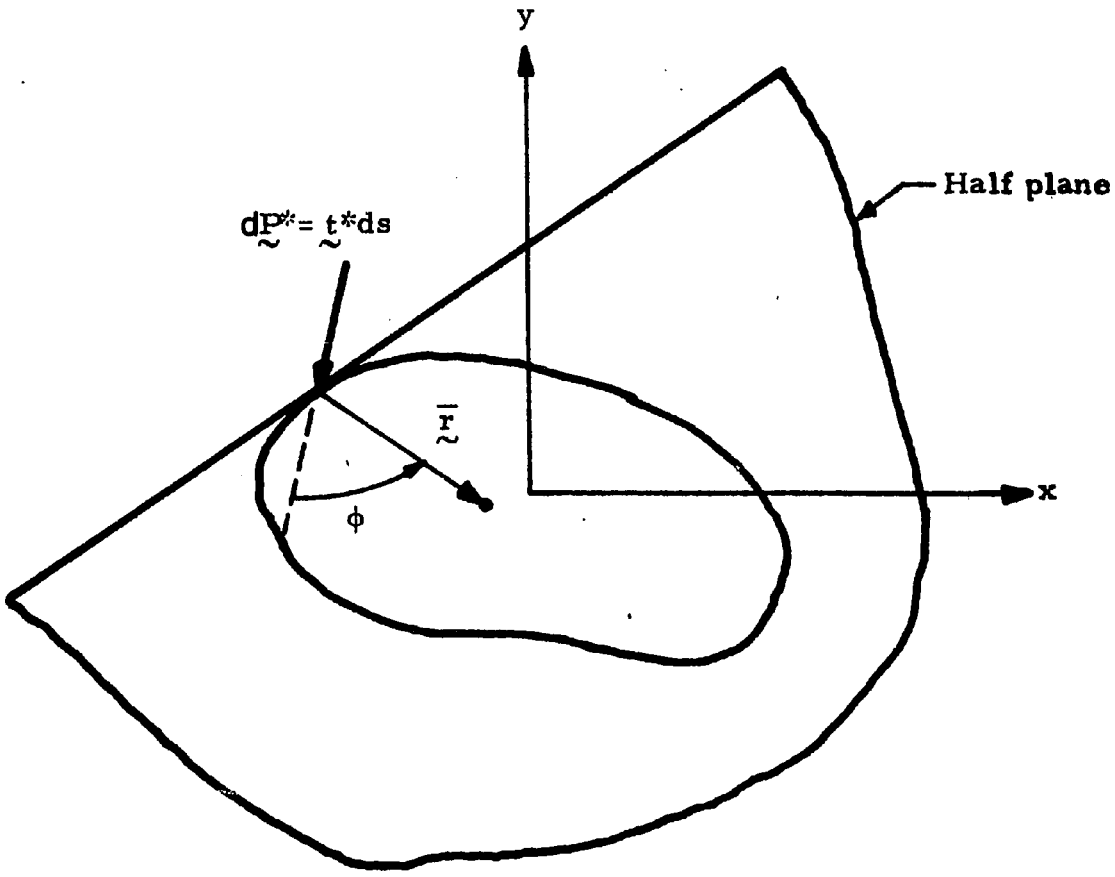


FIGURE 6 LINE LOAD ACTING ON THE BOUNDARY OF A HALF PLANE AT THE POINT OF TANGENCY TO THE REAL BODY

where $\underset{\sim}{e}_i$ is a unit vector in the i-direction. Thus

$$\underset{\sim}{e}_r \cdot \underset{\sim}{e}_x = \frac{\bar{r}_x}{\bar{r}} \qquad \underset{\sim}{e}_r \cdot \underset{\sim}{e}_y = \frac{\bar{r}_y}{\bar{r}} \tag{1.6}$$

where $\bar{r}_x$ and $\bar{r}_y$ are the x and y components of the vector $\underset{\sim}{\bar{r}}$.

Let $d\underset{\sim}{P}^* = \underset{\sim}{t}^* ds$. Then

$$d\underset{\sim}{P}^* \cdot \underset{\sim}{\bar{r}} = (t_x^* \bar{r}_x + t_y^* \bar{r}_y)\, ds \tag{1.7}$$

Combining (1.4), (1.5), (1.6) and (1.7):

$$\begin{aligned} d\bar{\sigma}_{xx} &= -\frac{2}{\pi} \frac{t_x^* \bar{r}_x + t_y^* \bar{r}_y}{\bar{r}^4} \bar{r}_x^2 ds \\ d\bar{\sigma}_{yy} &= -\frac{2}{\pi} \frac{t_x^* \bar{r}_x + t_y^* \bar{r}_y}{\bar{r}^4} \bar{r}_y^2 ds \\ d\bar{\sigma}_{xy} &= -\frac{2}{\pi} \frac{t_x^* \bar{r}_x + t_y^* \bar{r}_y}{\bar{r}^4} \bar{r}_x \bar{r}_y ds \end{aligned} \tag{1.8}$$

where $\bar{r}^2 = \bar{r}_x^2 + \bar{r}_y^2$. From the definition of the Green's function:

$$\begin{aligned} d\bar{\sigma}_{xx} &= \oint G_{xx;q}\, t_q^* ds \\ d\bar{\sigma}_{yy} &= \oint G_{yy;q}\, t_q^* ds \\ d\bar{\sigma}_{xy} &= \oint G_{xy;q}\, t_q^* ds \end{aligned} \tag{1.9}$$

Comparing (1.8) and (1.9):

$$\begin{aligned} \oint G_{xx;q}\, t_q^* &= -\frac{2}{\pi} \frac{t_x^* \bar{r}_x + t_y^* \bar{r}_y}{\bar{r}^4} \bar{r}_x^2 \\ \oint G_{yy;q}\, t_q^* &= -\frac{2}{\pi} \frac{t_x^* \bar{r}_x + t_y^* \bar{r}_y}{\bar{r}^4} \bar{r}_y^2 \\ \oint G_{xy;q}\, t_q^* &= -\frac{2}{\pi} \frac{t_x^* \bar{r}_x + t_y^* \bar{r}_y}{\bar{r}^4} \bar{r}_x \bar{r}_y \end{aligned} \tag{1.10}$$

Note that $\bar{r}_x = x - x'$ and $\bar{r}_y = y - y'$ where x,y refer to the field point P

and x', y' refer to the boundary point P_1 on $\overline{B}$.

Introducing the following dimensionless variables:

$$r_x = \frac{\overline{r}_x}{L} \qquad p_q = \frac{t_q}{P/L} \qquad S = s/L$$
$$r_y = \frac{\overline{r}_y}{L} \qquad p_q^* = \frac{t_q^*}{P/L} \tag{1.11}$$

where P is a characteristic load and L a characteristic length, and substituting equation (1.10) into equation (1.3), the integral equations become:

$$p_x^* - \frac{2}{\pi} \int_{\overline{B}} \left(\frac{p_x^* r_x + p_y^* r_y}{(r_x^2 + r_y^2)^2} \right) (r_x^2 n_x + r_x r_y n_y)\, dS = p_x$$
$$p_y^* - \frac{2}{\pi} \int_{\overline{B}} \left(\frac{p_x^* r_x + p_y^* r_y}{(r_x^2 + r_y^2)^2} \right) (r_x r_y n_x + r_y^2 n_y)\, dS = p_y \tag{1.12}$$

To evaluate equations (1.12) numerically, the boundary is divided into intervals of arbitrary length ΔS_i. The tractions on each interval are replaced by concentrated line loads at the center of each interval defined by:

$$P_{xi}^* = \int_{\Delta S_i} p_x^*\, dS \qquad P_{xi} = \int_{\Delta S_i} p_x\, dS$$
$$P_{yi}^* = \int_{\Delta S_i} p_y^*\, dS \qquad P_{yi} = \int_{\Delta S_i} p_y\, dS \tag{1.13}$$

Using the trapezoidal rule [29], a set of algebraic equations is obtained which can be solved for the concentrated fictitious loads P_{xi}^*, P_{yi}^* in the i^{th} interval:

$$P^*_{xi} - \frac{2}{\pi} \sum_{\substack{j=1 \\ j \neq i}}^{N} \left[\frac{(P^*_{xj}\, r_{xij} + P^*_{yj}\, r_{xij}\, r_{yij})}{(r^2_{xij} + r^2_{yij})^2} (n_{xi}\, r_{xij} + n_{yi}\, r_{yij}) \right] \Delta S_i = P_{xi}$$

$$P^*_{yi} - \frac{2}{\pi} \sum_{\substack{j=1 \\ j \neq i}}^{N} \left[\frac{(P^*_{xj}\, r_{xij}\, r_{yij} + P^*_{yj}\, r^2_{yij})}{(r^2_{xij} + r^2_{yij})^2} (n_{xi}\, r_{xij} + n_{yi}\, r_{yij}) \right] \Delta S_i = P_{yi} \qquad (1.14)$$

$$i = 1, 2, \cdots, N$$

where r_{xij}, r_{yij} are the x,y distances between centers of the subdivisions, and N is the number of subdivisions.

Equations (1.14) can be solved by either matrix inversion or iteration. Iteration has been chosen since machine time is generally less. These equations can be written as:

$$P^*_{xi} = P_{xi} - \sum_{j=1}^{N} (A_{ij}\, P^*_{xj} + B_{ij}\, P^*_{yj})$$

$$P^*_{yi} = P_{yi} - \sum_{j=1}^{N} (B_{ij}\, P^*_{xj} + C_{ij}\, P^*_{yj}) \qquad (1.15)$$

where A_{ij}, B_{ij} and C_{ij} are found by comparing with equations (1.14). Following Massonnet [25], a convergence parameter, $0 < \alpha < 1$, is introduced to facilitate convergence. The equations are then iterated in the following form:

$$P^{*(n+1)}_{xi} = \alpha\, P_{xi} + (1 - \alpha)\, P^{*(n)}_{xi} - \sum_{j=1}^{N} \alpha\, (A_{ij}\, P^{*(n)}_{xj} + B_{ij}\, P^{*(n)}_{yj})$$

$$P^{*(n+1)}_{yi} = \alpha\, P_{yi} + (1 - \alpha)\, P^{*(n)}_{yi} - \sum_{j=1}^{N} \alpha\, (B_{ij}\, P^{*(n)}_{xj} + C_{ij}\, P^{*(n)}_{yj}) \qquad (1.16)$$

where the superscripts in parentheses represents the number of the iteration. In all computations, the value $\alpha = 0.8$ has been used and convergence in general has been fairly rapid except in situations where there are large gradients in the boundary tractions. The initial values of P^*_{xi}, P^*_{yi} were always set equal to the actual tractions on the boundary.

Once the fictitious loads have been computed, the stresses are obtained from the numerical approximation of equations (1.1):

$$\sigma_{xxi} = \frac{\bar{\sigma}_{xxi}}{P/L} = -\frac{2}{\pi} \sum_{j=1}^{N} \frac{P^*_{xj} r_{xij} + P^*_{yj} r_{yij}}{(r^2_{xij} + r^2_{yij})^2} r^2_{xij}$$

$$\sigma_{yyi} = \frac{\bar{\sigma}_{yyi}}{P/L} = -\frac{2}{\pi} \sum_{j=1}^{N} \frac{P^*_{xj} r_{xij} + P^*_{yj} r_{yij}}{(r^2_{xij} + r^2_{yij})^2} r^2_{yij} \qquad (1.17)$$

$$\sigma_{xyi} = \frac{\bar{\sigma}_{xyi}}{P/L} = -\frac{2}{\pi} \sum_{j=1}^{N} \frac{P^*_{xj} r_{xij} + P^*_{yj} r_{yij}}{(r^2_{xij} + r^2_{yij})^2} r_{xij} r_{yij}$$

where the stresses are in dimensionless form.

The equations derived in this section are included in the "fracture" programs of Appendices B and D.

CHAPTER II

FRACTURE ANALYSIS

1. Introductory Remarks

In this chapter, the theory is developed and applied to a boundary-value problem of practical interest (see figure 7). The solution to this problem will be useful in the development of a "penetration" theory in rock mechanics [27] since it will provide a means of analyzing the chip formation process during penetration by a wedge-shaped indentor.

The problem of figure 7 is the following. A truncated quarter plane DBAC is loaded along the truncation boundary BA by a given traction distribution. The material is isotropic, homogeneous and elastic-brittle. Also, the truncated quarter plane is in a state of plane strain. In this problem, the plane strain condition insures that for most practical values of Poisson's ratio ($\nu > .2$), the principal stress component normal to the x-y plane is intermediate between the principal stresses, $\overline{\sigma}_1$ and $\overline{\sigma}_2$, in the x-y plane. Thus the stress $\overline{\sigma}_z$ can be neglected in the fracture analysis following the assumption of both the Mohr criterion and the Griffith theory. It should be noted that the plane strain condition does not always insure the intermediacy of the normal stress. A criterion is derived in Appendix A which is used to determine whether or not the normal stress is in fact intermediate. This criterion should be applied at each point in a plane strain problem

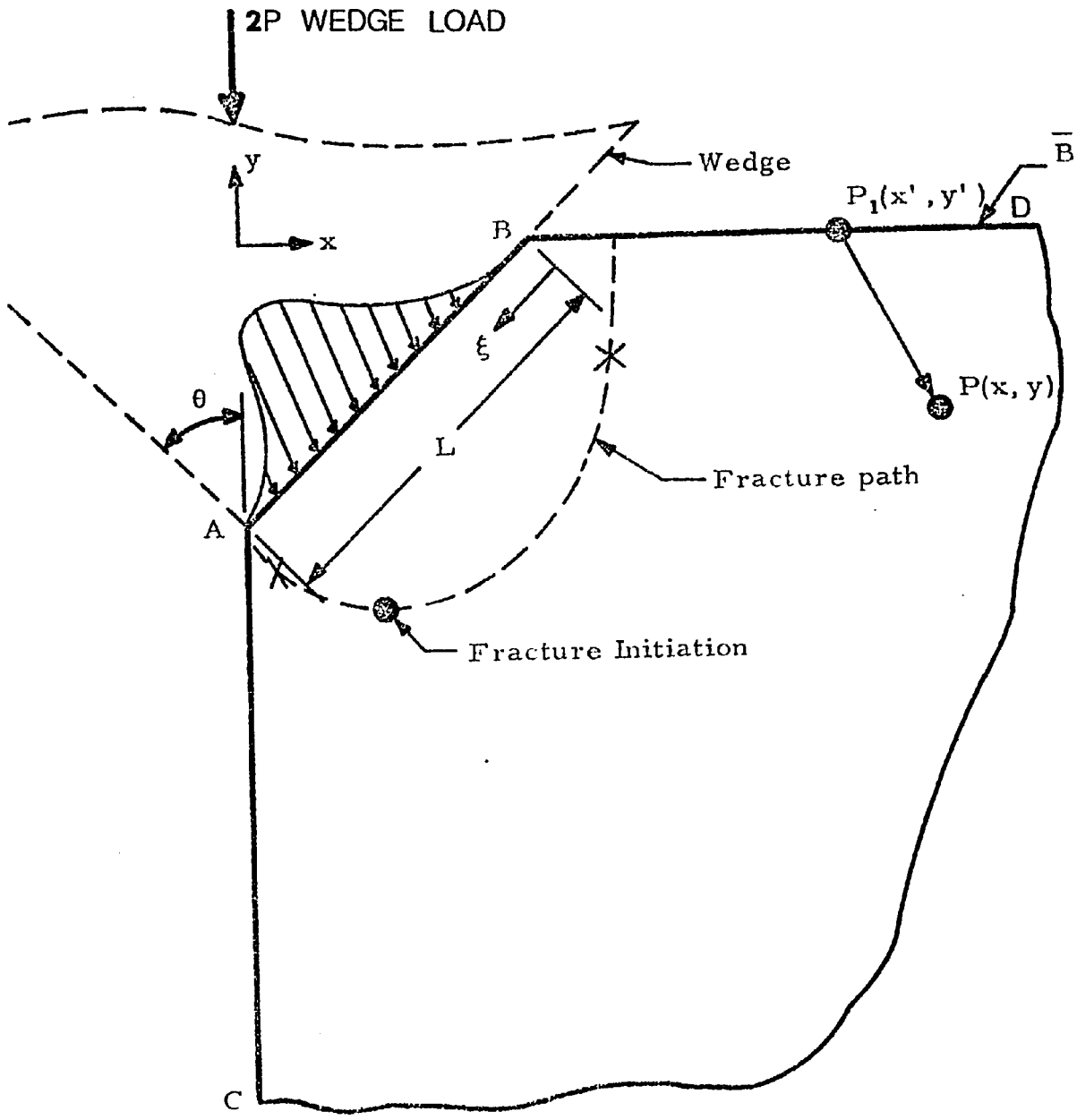


FIGURE 7 BOUNDARY-VALUE PROBLEM GEOMETRY

before application of the fracture criterion. If the normal stress is not intermediate but rather is the largest principal stress algebraically, fracture would occur in a plane oblique to the plane of the problem at that point rather than being a plane surface perpendicular to the problem plane.

The formation of the chip can be described in terms of the stages of fracture growth outlined earlier. (These can be followed on figure 7.) As the traction on edge BA is proportionately increased, the stresses at some point in the region eventually satisfy the fracture criterion and fracture is initiated. As the traction is increased further, the fracture grows in a stable manner. At some point, this growth becomes unstable and the fracture surface protracts rapidly to the free boundaries. It is of interest to determine the fracture initiation load P_i (the total vertical load on the truncation edge BA necessary to initiate fracture), the location of this initiation, the geometry of the completed chip, and the chip formation load P_f (the vertical load on the trunction edge BA at the transition between stable and unstable fracture growth).

In section II.2, the application of the Integral Equation Method to the determination of the stress field in the truncated quarter plane is treated. In this analysis, a traction distribution of the following form will be assumed:

$$t_n = \begin{cases} 0 & \text{on DB} \\ p\,(\xi/L)^m\,(1 - \cos 2\pi\xi/L) & \text{on BA} \\ 0 & \text{on AC} \end{cases}$$

$$t_s = \begin{cases} 0 & \text{on DB} \\ \mu_f\, t_n & \text{on BA} \\ 0 & \text{on AC} \end{cases} \qquad (2.1)$$

where t_n, t_s are the normal and tangential traction components, ξ is a coordinate along BA (defined in figure 7) and μ_f is the coefficient of friction between the material and the wedge. m is a form parameter which, for increasing values, gives a more asymmetric and concentrated traction distribution. p is a scalar pressure defined by:

$$p = \frac{P \cos \phi_f}{L \sin (\theta + \phi_f) \int_0^1 \eta^m\,(1 - \cos 2\pi\eta)\, d\eta} \qquad (2.2)$$

where θ is the half-wedge angle (truncation angle) and ϕ_f is the friction angle ($\mu_f = \tan \phi_f$). With p defined as in equation (2.2), μ_f and m can be varied without affecting the value of the vertical force component, P/L. Before solving for the stress field, the accuracy of the Integral Equation Method is assessed by comparison to a known analytical solution for a similar boundary-value problem.

In section II. 3, a fracture analysis is done for the case of the linear Coulomb-Mohr criterion. In the linear case, a dimensionless parametric study can be performed and this is done. Fracture initiation load and location are studied as functions of the geometric, loading and material parameters. Five parameters, in fact, define this problem.

The geometry is defined by the truncation angle, θ; the form parameter, m, and the coefficient of friction, μ_f, define the traction distribution; and the constants μ and C define the material fracture properties.

This parametric study as well as an analysis of subsequent fracture growth and instability are included in section II. 4.

There are, however, many materials for which a linear fracture envelope is not a good representation. This nonlinearity, as in other non-linear problems, precludes a single dimensionless solution. Here it is necessary that the specific fracture envelope be known.

In section II. 5, a general analysis is developed for fracture initiation and early fracture growth in non-linear brittle materials and is applied to two such materials, Blair dolomite and quartzite. Again, the problem of figure 7 is considered. Of further interest, and included in the analysis, is the effect of hydrostatic pressure on the fracture initiation.

An iterative technique is developed for handling these nonlinear fracture envelopes based on a series of linear envelopes. This technique is then applied to the two materials mentioned above and results are obtained for varying hydrostatic pressure and truncation angle. These are presented and discussed in section II. 6.

2. Stress Analysis

The Integral Equation Method of section I. 3 will now be applied to the geometry of figure 7.

There are two very important questions which arise concerning the numerical solution of this problem. These are: (1) at which points on the boundaries DB and AC should the boundary subdivisions begin and end; and (2) what should be the sizes of the subdivisions on these boundaries and on the boundary BA? These questions are answered by a comparison with a known exact solution.

The stresses in a quarter plane due to a line load applied at the apex are [28], see figure 8a :

$$\bar{\sigma}_{\rho\rho} = -\frac{Q\cos\delta}{\rho\left(\frac{\pi}{4}+\frac{1}{2}\right)} \qquad \bar{\sigma}_{\rho\delta} = \bar{\sigma}_{\delta\delta} = 0 \tag{2.3}$$

Now considering the region in figure 8b and determining the traction on BA necessary to equilibrate the line force Q:

$$\begin{aligned} t_\eta &= -\bar{\sigma}_{\rho\rho}\cos^2\delta \\ t_\xi &= -\bar{\sigma}_{\rho\rho}\sin\delta\cos\delta \end{aligned} \tag{2.4}$$

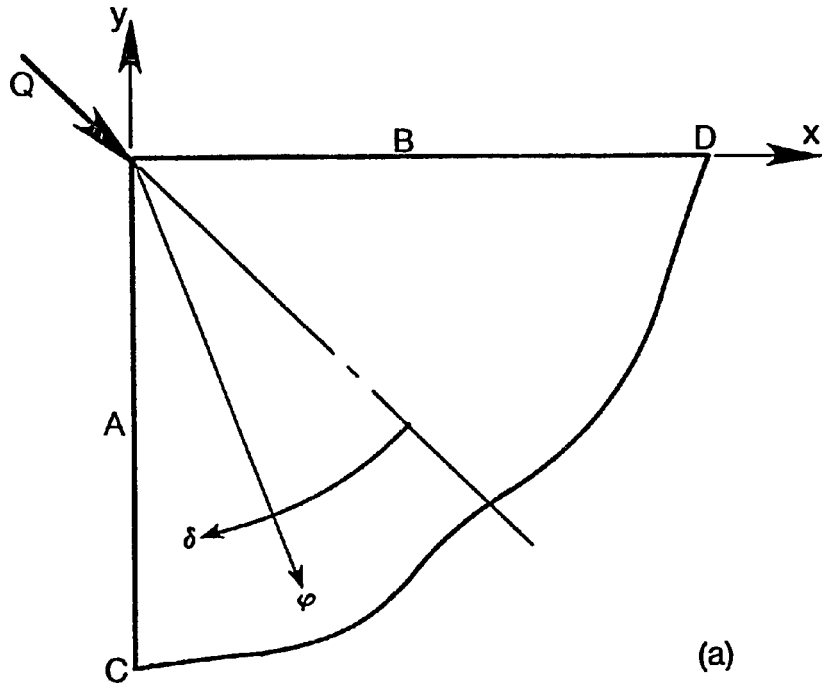
From geometry:

$$\begin{aligned} \rho^2 &= \xi^2 + (L/2)^2 \\ \cos\delta &= L/2\rho \\ \sin\delta &= \xi/\rho \end{aligned} \tag{2.5}$$

Combining (2.3), (2.4), and (2.5):

$$\begin{aligned} t_\eta &= \frac{Q}{L}\left(\frac{1}{2\pi+4}\right)\left[\frac{1}{\left(\frac{\xi}{L}\right)^4+\frac{1}{2}\left(\frac{\xi}{L}\right)^2+\frac{1}{16}}\right] \\ t_\xi &= \frac{Q}{L}\left(\frac{\xi/L}{\pi+2}\right)\left[\frac{1}{\left(\frac{\xi}{L}\right)^4+\frac{1}{2}\left(\frac{\xi}{L}\right)^2+\frac{1}{16}}\right] \end{aligned} \tag{2.6}$$

$$-1/2 \le \xi/L \le 1/2$$



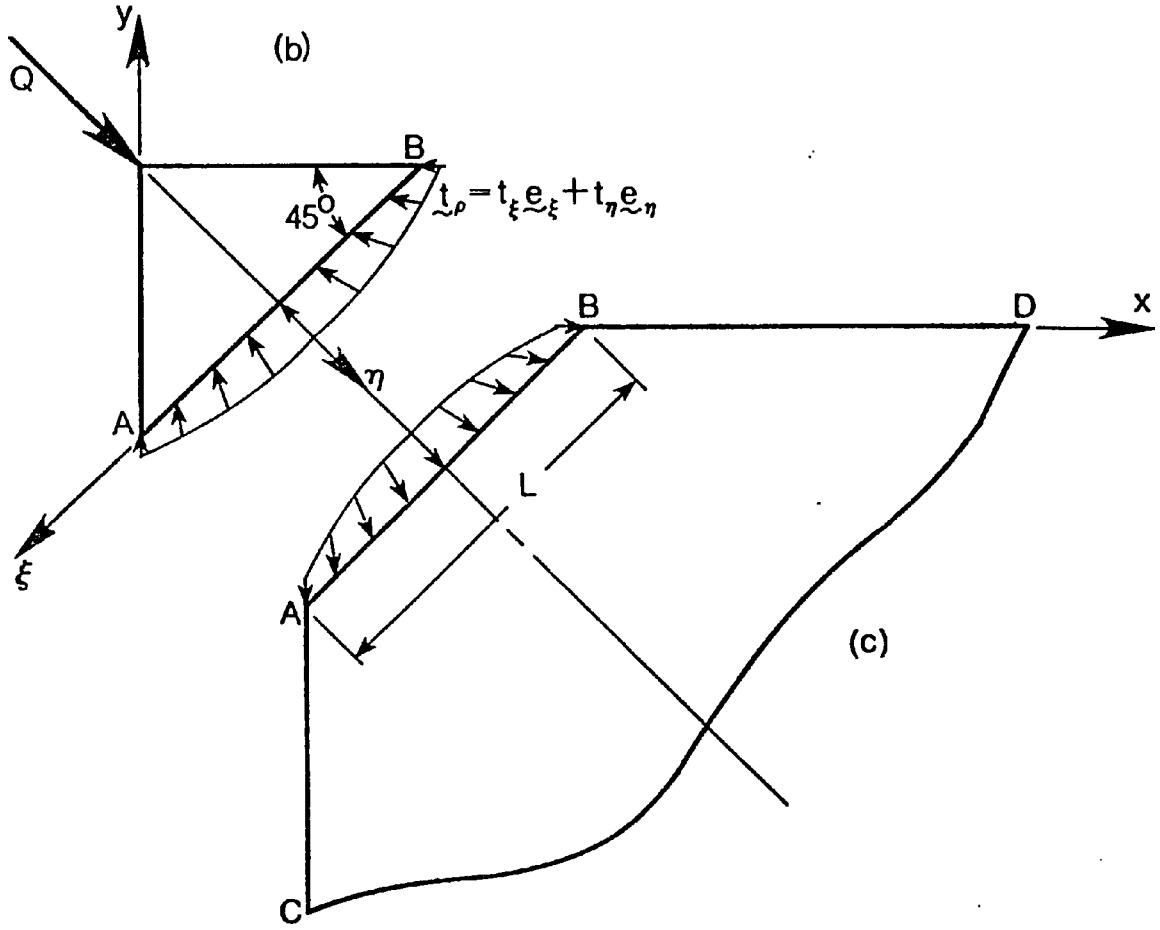


FIGURE 8 STRESSES IN A QUARTER PLANE DUE TO A LINE LOAD APPLIED AT THE APEX

and converting to x-y coordinate system:

$$t_x = \frac{Q}{L}\frac{\sqrt{2}\left(\frac{1}{2} - \frac{\xi}{L}\right)}{2(\pi + 2)}\left[\frac{1}{\left(\frac{\xi}{L}\right)^4 + \frac{1}{2}\left(\frac{\xi}{L}\right)^2 + \frac{1}{16}}\right]$$

$$t_y = -\frac{Q}{L}\frac{\sqrt{2}\left(\frac{1}{2} + \frac{\xi}{L}\right)}{2(\pi + 2)}\left[\frac{1}{\left(\frac{\xi}{L}\right)^4 + \frac{1}{2}\left(\frac{\xi}{L}\right)^2 + \frac{1}{16}}\right] \qquad (2.7)$$

Then, the stress field in the region of figure 8c is equivalent to the stress field in the region of figure 8a provided the tractions given by equations (2.7) are applied to the boundary BA.

Equations (2.7) in non-dimensional form are:

$$p_x = \frac{t_x L}{Q} = .1375\left[\frac{\frac{1}{2} - \frac{\xi}{L}}{\left(\frac{\xi}{L}\right)^4 + \frac{1}{2}\left(\frac{\xi}{L}\right)^2 + \frac{1}{16}}\right]$$

$$p_y = \frac{t_y L}{Q} = -.1375\left[\frac{\frac{1}{2} + \frac{\xi}{L}}{\left(\frac{\xi}{L}\right)^4 + \frac{1}{2}\left(\frac{\xi}{L}\right)^2 + \frac{1}{16}}\right] \qquad (2.8)$$

Based on this traction distribution, the exact values of the principal stresses at any point in the region of figure 8c are

$$\sigma_1 = 0 \qquad \sigma_2 = \frac{\bar{\sigma}_{\rho\rho} L}{Q} \qquad (2.9)$$

where σ_1 is the maximum principal stress algebraically. The numerical values for selected field points are given in Table 2.1. Of these field points, 1 - 12 are located at a distance of L/8 from the boundary, 13 - 20 are L/16 from the boundary and 21 - 29 are L/32 from the boundary (see figure 9).

TABLE 2.1

The Exact Solution for the Problem of Figure 8

Field Point	Coordinates (figure 8c) x_i/L	y_i/L	$(\sigma_2)_{exact}$
1	.4419	- .4419	-1.2448
2	.3536	- .5303	-1.1969
3	.2652	- .6187	-1.0731
4	.1768	- .7071	- .9153
5	.1250	- .7589	- .8220
6	.1250	- .8321	- .7436
7	.1250	- .9571	- .6389
8	.1250	-1.0821	- .5596
9	.1250	-1.2071	- .4976
10	.1250	-1.3321	- .4478
11	.1250	-1.4571	- .4069
12	.1250	-1.5821	- .3728
13	.3977	- .3977	-1.3831
14	.2210	- .5745	-1.1549
15	.0625	- .7330	- .8086
16	.0625	- .8214	- .7165
17	.0625	- .8321	- .7068
18	.0625	-1.0821	- .5359
19	.0625	-1.3321	- .4314
20	.0625	-1.5821	- .3609
21	.3757	- .3757	-1.4644
22	.1989	- .5524	-1.1989
23	.0625	- .6977	- .8417
24	.0313	- .7201	- .7956
25	.0313	- .7642	- .7480
26	.0313	- .8321	- .6850
27	.0313	-1.0821	- .5226
28	.0313	-1.3321	- .4224
29	.0313	-1.5821	- .3544

Now that the exact solution for the problem of figure 8c is known, the approximate method, developed in section I.3 can be applied to the same problem and its accuracy can be evaluated. To answer the question of boundary cut-offs (i.e., what portions of boundaries DB and AC should be included), the problem was solved for DB and AC equal to 2L, 3L, 4L and 5L. All sub-divisions (mesh spacings) were of length L/8. The results for several field points are given in Table 2.2. This sampling gives a clear indication of the small sensitivity of the results on the boundary cut-offs. Therefore, boundary cut-offs of 2L on DB and AC are used in all subsequent calculations.

Several combinations of mesh spacing were considered; that shown in figure 9 was the best compromise between accuracy and computer cost. The accuracy of the method for such a mesh spacing is given in Table 2.3. The field points considered are shown in figure 9.

From figure 9 and Table 2.3, the boundary cut-offs and mesh spacing which have been chosen can be evaluated. Of those points located at a distance L/8 from the boundary (points 1-12), the accuracy was within 2.6%. Of those located L/16 from the boundary (points 13-20), the accuracy was within 3.6%. At L/32 from the boundary, the accuracy was no worse than 5.3%. At points farther into the field than L/8 but within a distance L from the truncated face, the solution is virtually exact. As will be seen in the fracture analysis to follow, fracture initiation generally is located within this region. Thus it can

TABLE 2.2

Dependence of Integral Method Solution on Boundary Cut-off

Field Point	$(\sigma_z)_{approx}$ 2L	3L	4L	5L
1	-1.1843	-1.1843	-1.1843	-1.1843
2	-1.1563	-1.1563	-1.1563	-1.1563
3	-1.0649	-1.0647	-1.0647	-1.0647
4	- .9265	- .9262	- .9262	- .9262
5	- .8427	- .8425	- .8424	- .8424
6	- .7471	- .7467	- .7466	- .7466
7	- .6277	- .6271	- .6269	- .6269
8	- .5503	- .5495	- .5492	- .5492
9	- .4911	- .4901	- .4898	- .4897
10	- .4436	- .4423	- .4419	- .4419
11	- .4046	- .4029	- .4025	- .4024
12	- .3720	- .3700	- .3695	- .3694

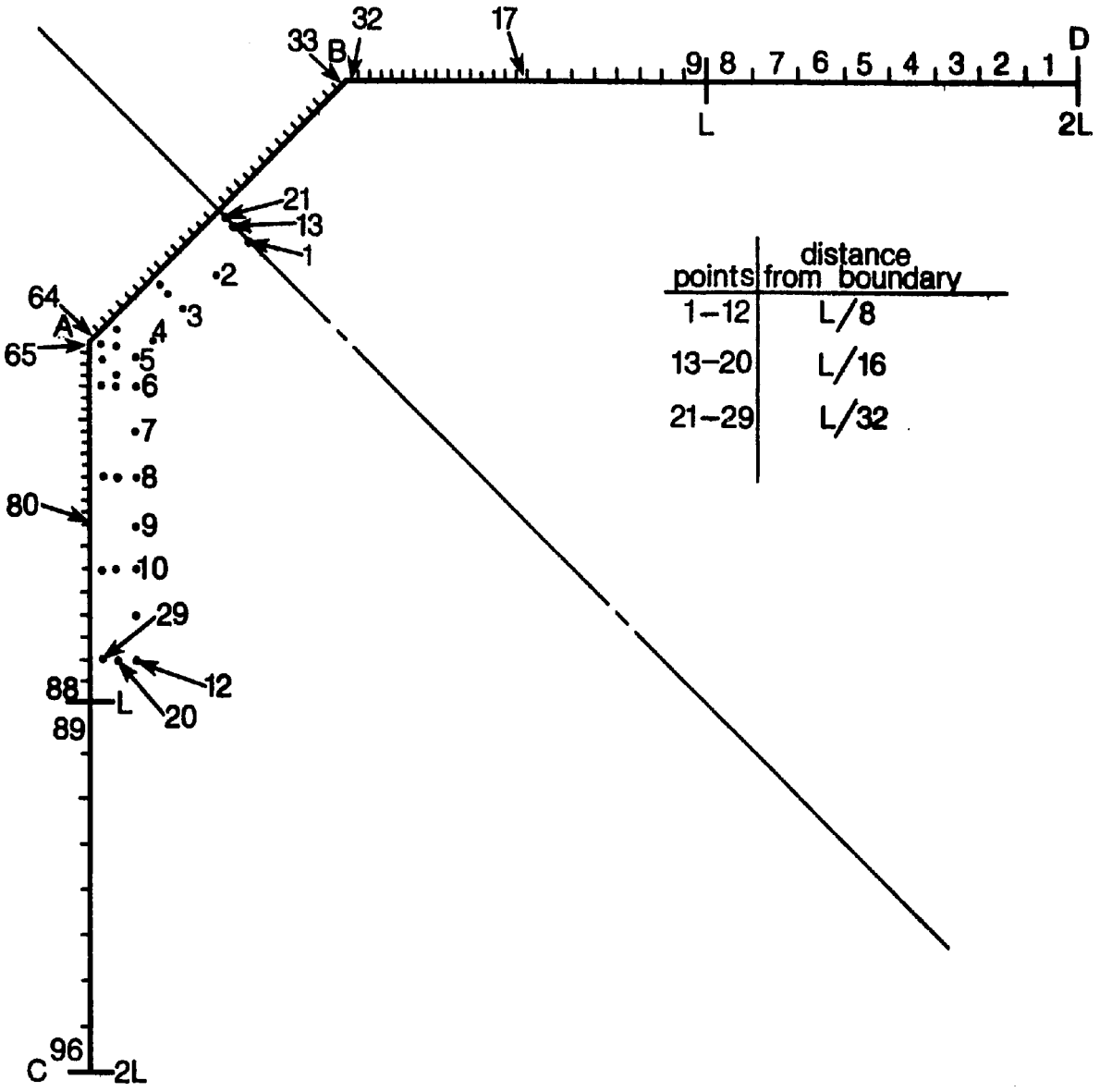


FIGURE 9 BOUNDARY MESH SPACING

TABLE 2.3

Integral Method Solution Using Mesh Spacing of Figure 9

Field Point	$(\sigma_2)_{approx}$	Error (%)
1	-1.2449	- .01
2	-1.1973	- .04
3	-1.0737	- .06
4	- .9165	- .13
5	- .8237	- .21
6	- .7396	- .54
7	- .6317	1.12
8	- .5567	.52
9	- .4994	- .37
10	- .4571	-2.09
11	- .4175	-2.60
12	- .3816	-2.33
13	-1.3824	.05
14	-1.1552	- .03
15	- .8137	- .63
16	- .7020	2.03
17	- .6919	2.11
18	- .5227	2.47
19	- .4469	-3.59
20	- .3748	-3.84
21	-1.4189	3.11
22	-1.1909	.67
23	- .8455	- .45
24	- .8216	-3.27
25	- .7166	4.19
26	- .6611	3.48
27	- .4996	4.40
28	- .4412	-4.45
29	- .3732	-5.28

be concluded that further refinement of the boundary sub-divisions is not warranted.

The integral method proves to be particularly useful in this analysis. Once the fictitious traction distribution is determined, the stresses anywhere in the field are found by an integration, equation (1.17). This is an important feature, since it will be necessary to search the field for the point of fracture initiation. Also, since the boundary, rather than the field, is sub-divided, the resulting matrix is of lower order than that generated by finite elements or finite differences. With the integral method, the stresses can be found anywhere in the field without interpolation and are essentially exact.

3. Fracture Analysis - Linear Criterion

Fracture initiation in the material is assumed to be governed by the Coulomb-Mohr fracture criterion:

$$|\bar{\tau}| + \mu \bar{\sigma} = C \qquad (2.10)$$

where $\bar{\tau}, \bar{\sigma}$ are the shear and normal stress components on the plane* which maximizes $\{|\bar{\tau}| + \mu \bar{\sigma}\}$; μ is the slope of the envelope; and C is the $\bar{\tau}$-intercept. Only two material constants, μ and C, characterize incipient fracture in the isotropic case.

*When the stress component normal to the plane of the problem is the intermediate principal stress, the plane which maximizes equation (2.10) is normal to the plane of the problem.

Equation (2.10) is an empirical criterion. The physical significance of this criterion and its applicability to fracture initiation in boundary value problems of this type is discussed in the Introduction and in section I.2.

By determining the angle which maximizes $|\bar{\tau}| + \mu \bar{\sigma}$, substituting it back into equation (2.10) and expressing the results in principal stresses, eq. (2.10) becomes

$$\frac{\mu}{2} (\bar{\sigma}_1 + \bar{\sigma}_2) + \frac{\sqrt{1 + \mu^2}}{2} (\bar{\sigma}_1 - \bar{\sigma}_2) = C \qquad (2.11)$$

where $\bar{\sigma}_1 > \bar{\sigma}_2$ algebraically. There are two angles for which equation (2.11) is valid, representing equally probably critical directions (normals to critical planes)

$$\psi_{1,2} = \gamma_1 \pm \left(\frac{\pi}{4} - \frac{\phi}{2}\right) \qquad (2.12)$$

where γ_1 represents the angle between the normal to the first principal plane and the x-axis defined in figure 7. The fracture criterion and fracture angles are represented geometrically in figure 10.

Non-dimensionalizing equation (2.11) with respect to P/L:

$$F(\sigma_1, \sigma_2; \mu) = \frac{\mu}{2} (\sigma_1 + \sigma_2) + \frac{\sqrt{1 + \mu^2}}{2} (\sigma_1 - \sigma_2) = \beta \qquad (2.13)$$

where β is the dimensionless "cohesion," $\beta = CL/P$. For a given value of μ, fracture initiation will occur at that point in the field at which $F(\sigma_1, \sigma_2; \mu)$ is maximum.

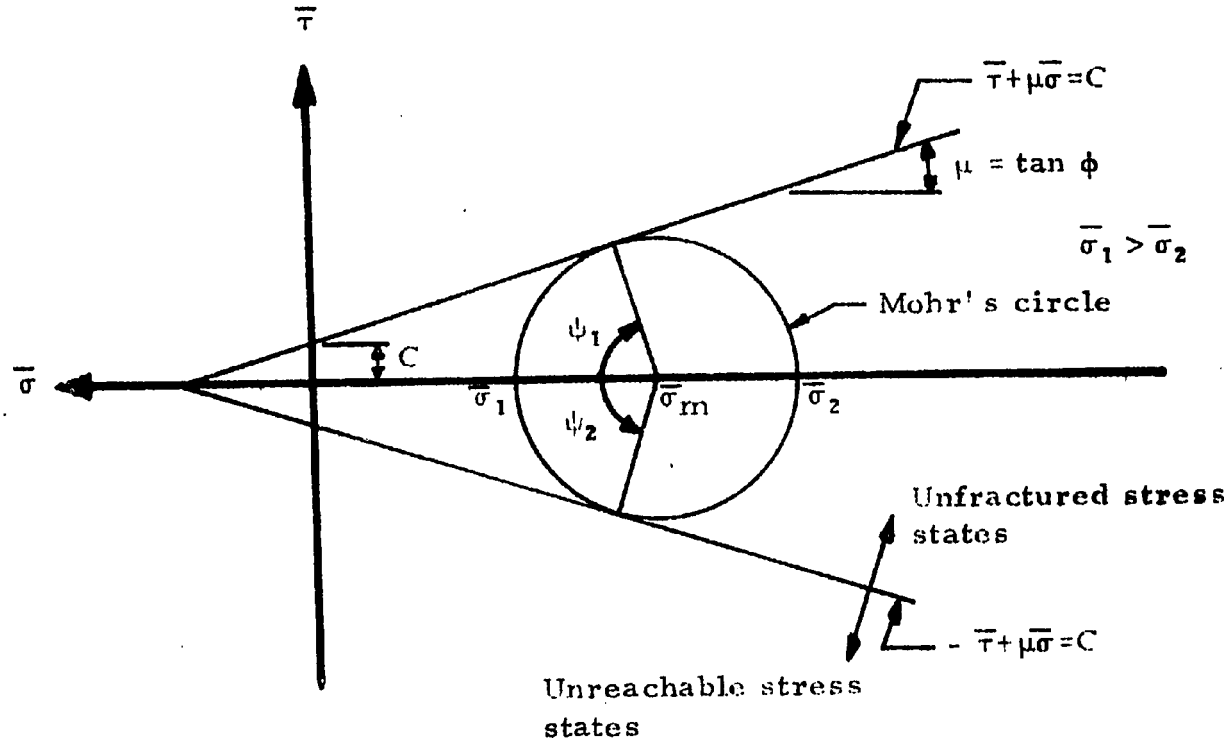


FIGURE 10 COULOMB-MOHR FRACTURE ENVELOPE

4. Numerical Results and Discussion

It is of interest to determine the effects on fracture initiation of the traction distribution (m, μ_f), geometry (θ) and material properties (μ, C). Given the first three parameters, the stresses (σ_1, σ_2) can be determined at prescribed points in the field by the integral equation method of section I.3. Then $F(\sigma_1, \sigma_2; \mu)$ can be determined at these same points. A typical set of initial points are shown as dots in figure 11. Once these initial points have been examined and a point of maximum F has been located, the region surrounding this point is subdivided and a more precise location is found. The computer program which implements this "searching" procedure is listed in Appendix B. The largest value of F found in this subdivided region is considered to be F_{max}. Equating F_{max} to β, the incipient fracture force P can be found for a given "cohesion" C and length L. A parametric study follows.

The traction distribution is altered by varying the form parameter m. Setting $\mu_f = 0.0$ and $\theta = 45^\circ$, the location and magnitude of fracture initiation as a function of m (and μ) are depicted in figures 11 and 13. Although the location of fracture initiation is strongly dependent on traction for small values of m, the dependence of the magnitude F_{max} is weak. Furthermore, for larger values of m, the dependence of fracture initiation location on traction distribution is also rather weak. This insensitivity of fracture initiation to traction distribution is most striking at the more physically realistic values of

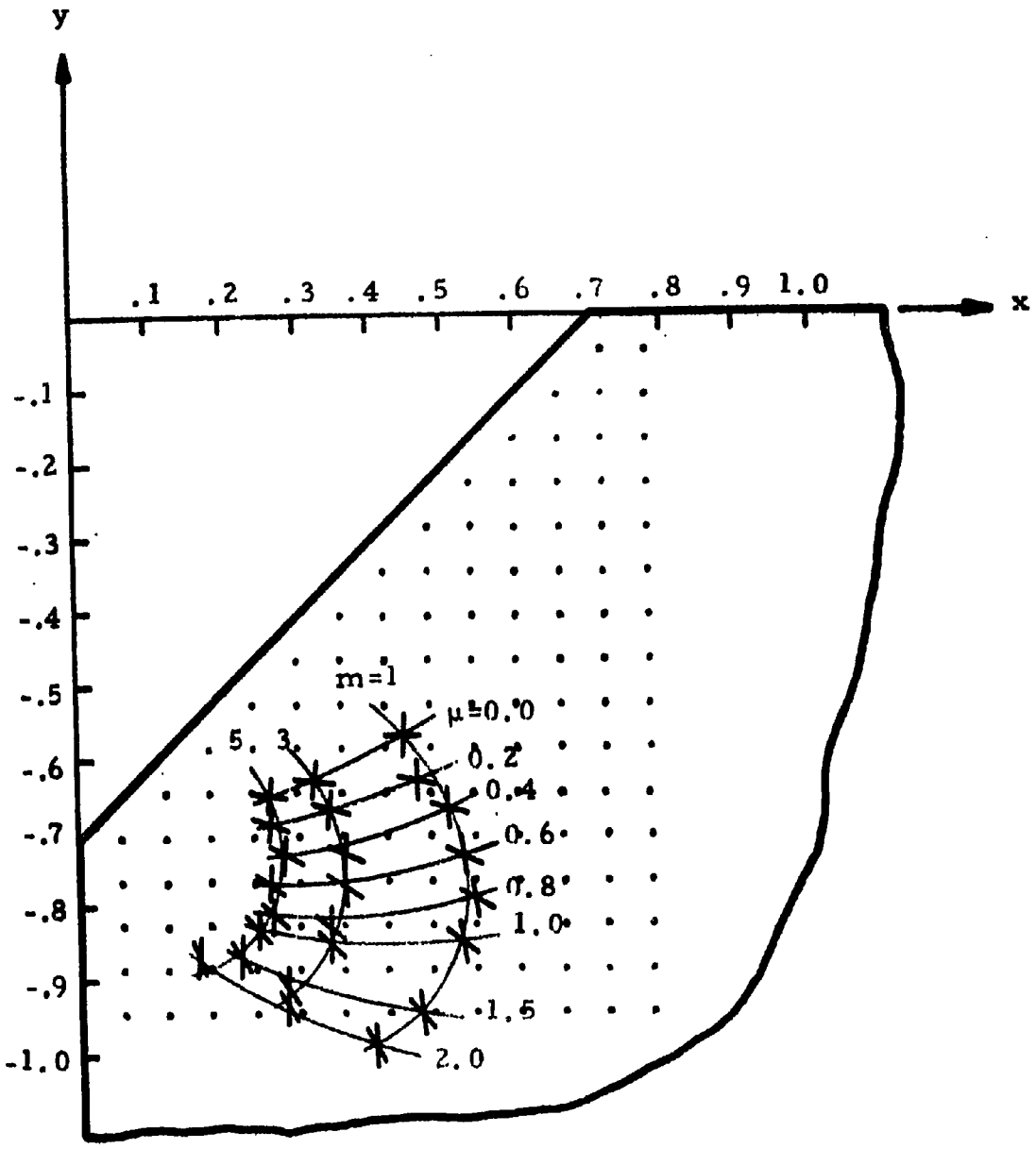


FIGURE 11 LOCATION AND DIRECTION OF CRITICAL CRACKS: $\theta=45^{o}$, $\mu_f=0.0$

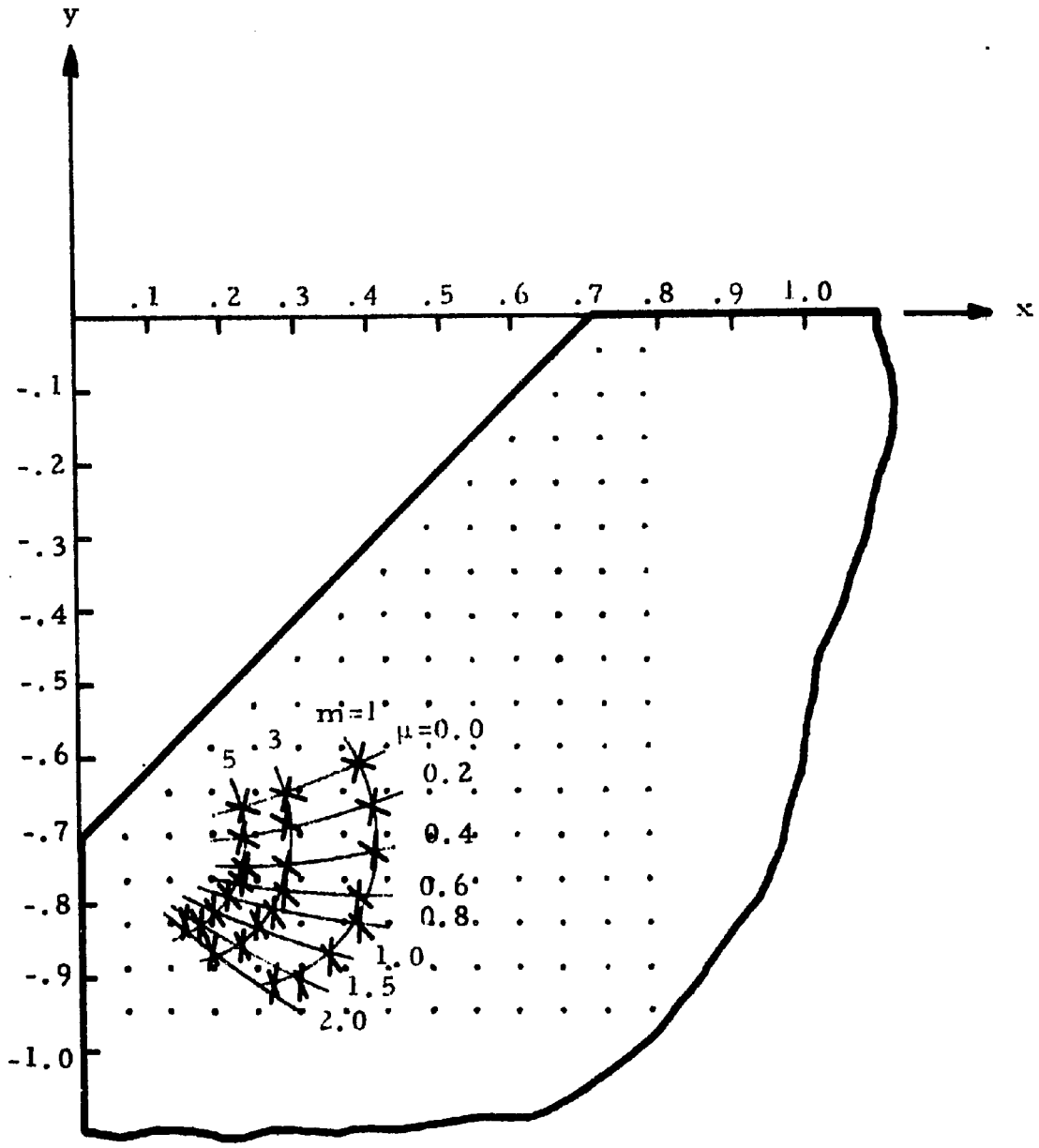


FIGURE 12 LOCATION AND DIRECTION OF CRITICAL CRACKS; $\theta=45^{o}$, $\mu_f=0.1$

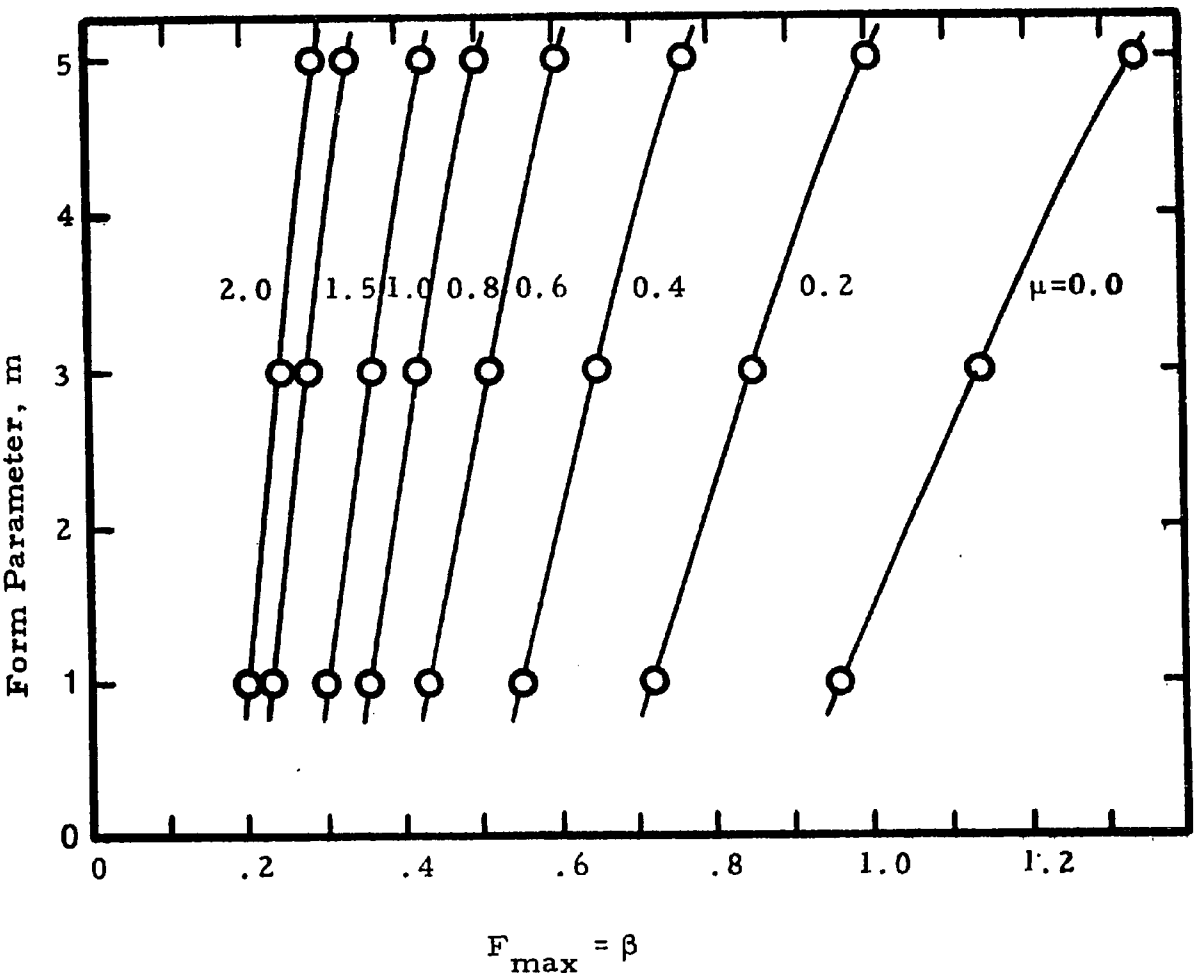


FIGURE 13 DEPENDENCE OF FRACTURE INITIATION ON TRACTION DISTRIBUTION; $\theta=45^{o}$, $\mu_f=0.0$

m ($m \cong 5$) and μ ($\mu \cong 1$), cf. [12]. Figures 12 and 14 depict the same curves for $\mu_f = 0.1$, a typical value of the coefficient of friction [30]. The effect of friction, again for large m and $\mu \cong 1$, is clearly small. Thus it can be concluded that for this particular problem the effect of traction distribution on fracture initiation, within physically realizable ranges of the parameters, is minor.

The dependence of fracture initiation on wedge geometry (truncation angle) is shown in figure 15 for $m = 5$ and $\mu_f = 0.0$. For sharp wedges ($\theta < 45^\circ$), this dependence is more noticeable than for blunt wedges ($\theta > 45^\circ$). However, again for values of μ near unity, the effect is small.

The effect of the material properties can be seen in figures 11-15. As the slope of the fracture envelope μ is increased, the fracture initiation point moves deeper into the material, see figures 11, 12. Also for increasing μ, F_{max} decreases, denoting increasing forces necessary to cause fracture initiation. The two possible critical planes are shown at each point in figures 11 and 12. These planes play important roles in the fracture propagation process.

Thus far, fracture initiation in the truncated quarter-plane has been defined in terms of the load, geometry and material properties. Now the path of the fracture propagation from the onset of incipient fracture to the formation of a complete chip will be examined. The results suggest that the fracture follows the minimum gradient of a contour map of the fracture function $F(\sigma_1, \sigma_2; \mu)$, see equation (2.13).

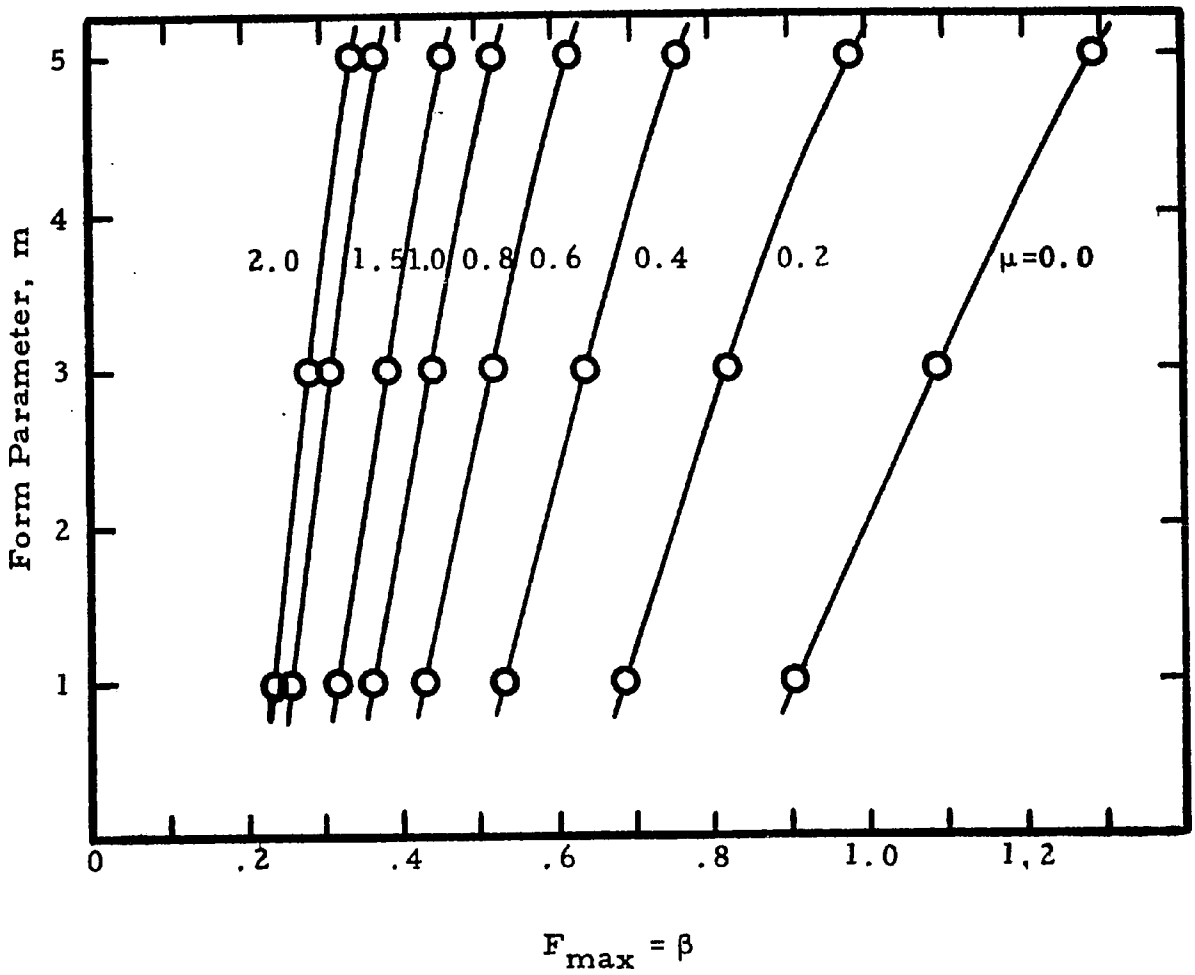


FIGURE 14 DEPENDENCE OF FRACTURE INITIATION ON TRACTION DISTRIBUTION; $\theta = 45^{o}$, $\mu_f = 0.1$

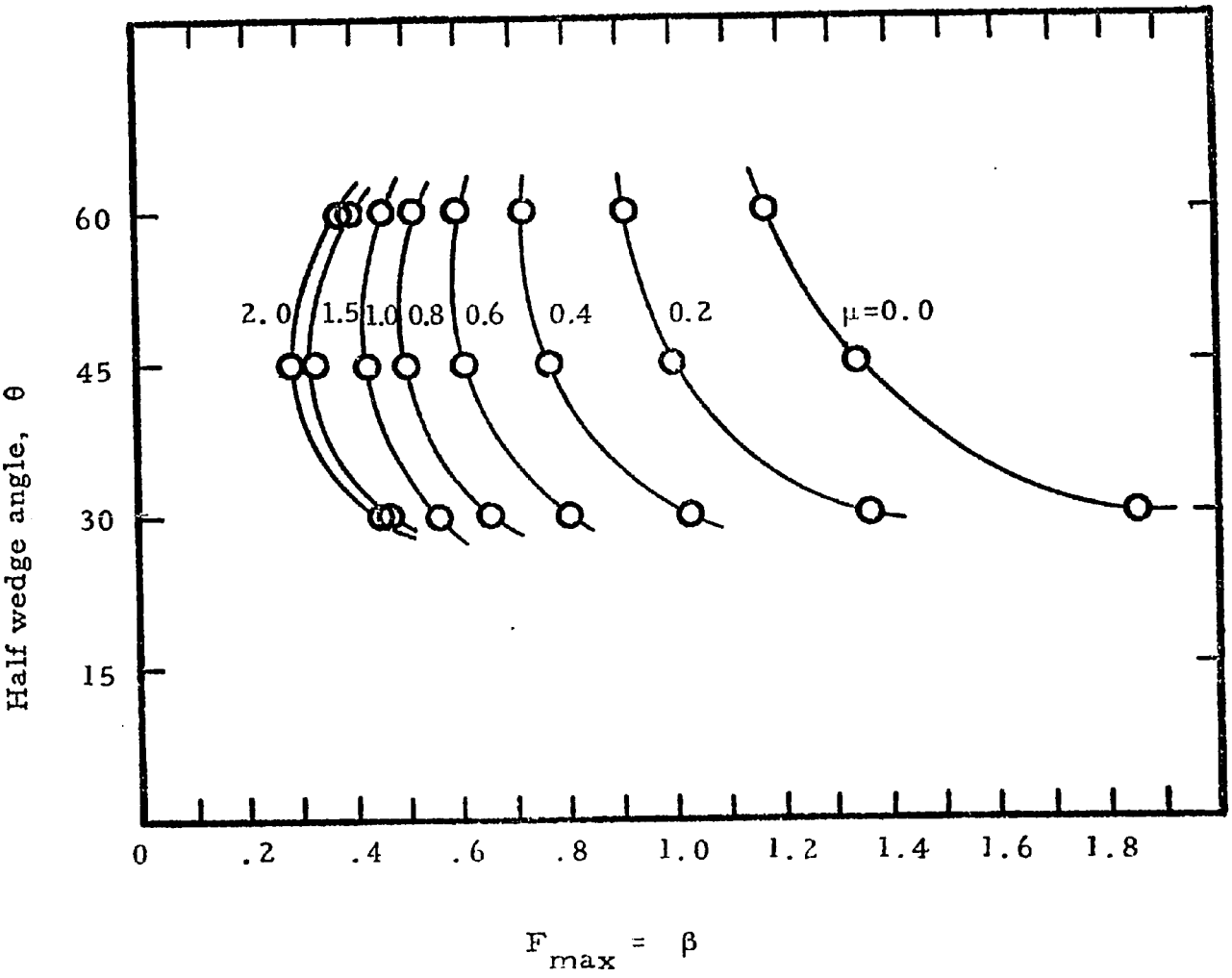


FIGURE 15 EFFECT OF WEDGE ANGLE ON FRACTURE INITIATION; $m=5, \mu_f=0.0$

The wedge force necessary to propagate the fracture to some point along this path is found using $F(\sigma_1, \sigma_2; \mu)$ in the same way as for fracture initiation. It is further suggested that the transition from stable to unstable fracture growth occurs at the inflection point of a plot of $F(\sigma_1, \sigma_2; \mu)$ versus $\hat{s}$ where $\hat{s}$ is the distance measured along the fracture path having its origin at the point of fracture initiation. The wedge force calculated at this inflection point represents the chip formation force.

In figure 16, a typical contour map of $F(\sigma_1, \sigma_2; \mu)$ is shown. Figure 17 depicts a closer view of the fracture initiation region. It can be seen in these figures that the function $F(\sigma_1, \sigma_2; \mu)$ forms a narrow "ridge" in the fracture initiation region with values quite close to F_{max}. The critical planes predicted by the Coulomb-Mohr theory, equation (2.12) and shown by the solid lines at each point in figure 17 represent the orientation of critical cracks in the modified Griffith theory (this interpretation is discussed in section II.5). It is well known that crack propagation from such a critical Griffith crack in a compressive stress state begins normal to the crack surface near the tips and bends so as to be parallel to the largest compressive stress (see Introduction). This is shown in figure 17b at the point of fracture initiation. However, it has been shown [18] that such a crack does not have the potential of forming the complete chip. It is suggested that fracture instead proceeds as follows. Crack growth is initiated almost simultaneously at several points in the vicinity of F_{max}, i.e., where $F(\sigma_1, \sigma_2; \mu) \approx F_{max}$.

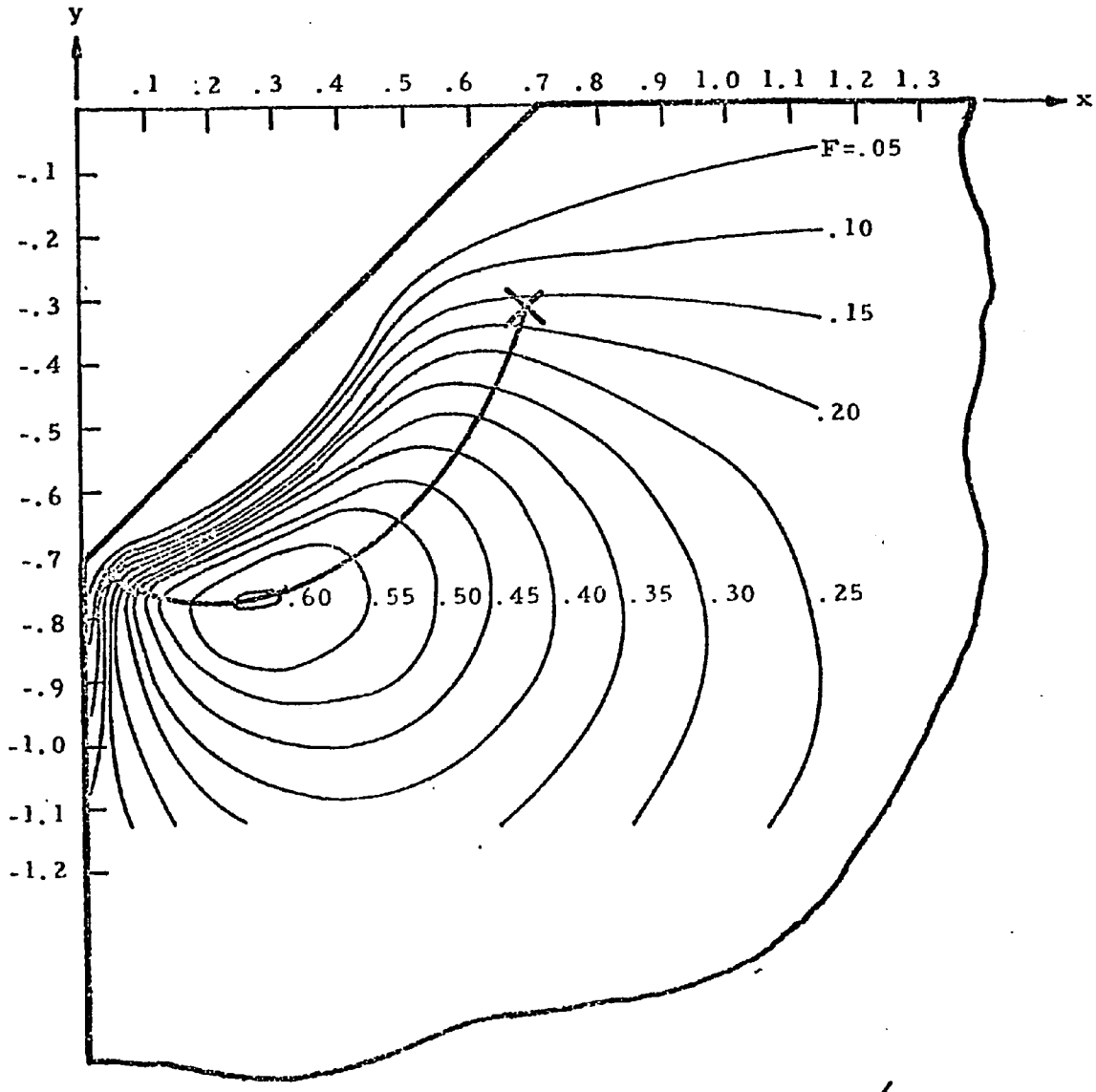
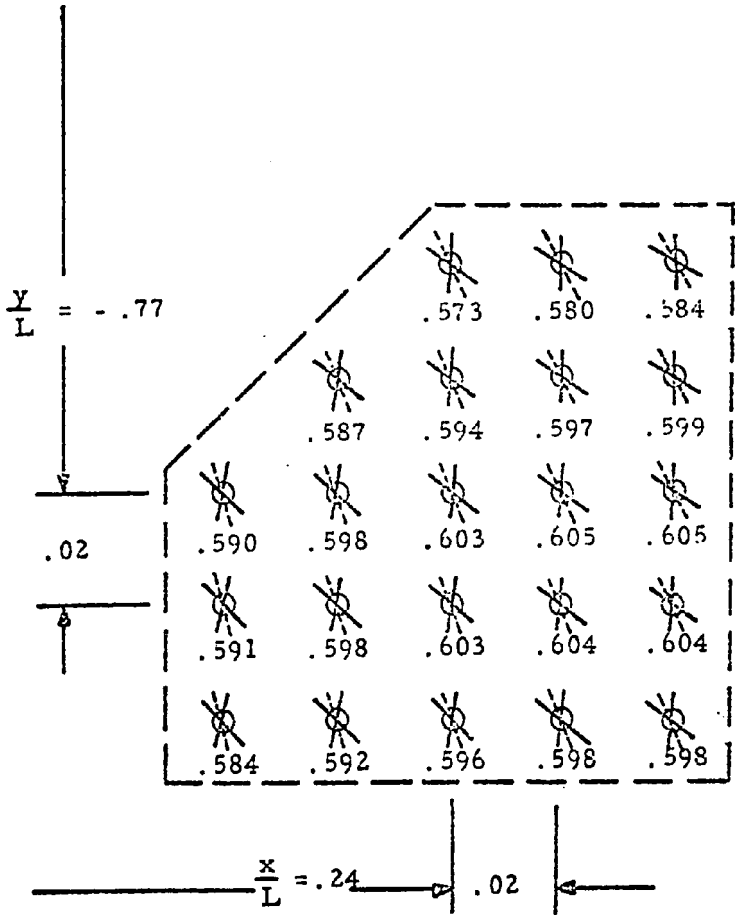
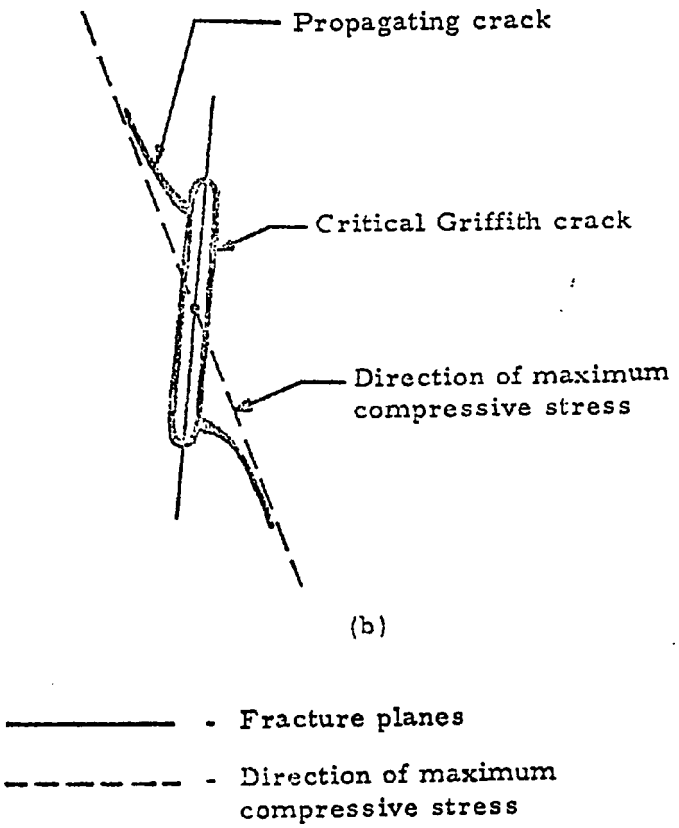


FIGURE 16 CONTOUR MAP OF FRACTURE FUNCTION $F(\sigma_1,\sigma_2;\mu)$; $m=5, \mu_1=0.0, \mu=0.6, \theta=45^{o}$



(a)



(b)

——— - Fracture planes

– – – – – - Direction of maximum compressive stress

FIGURE 17 ENLARGED VIEW OF FRACTURE INITIATION REGION; $m=5, \mu_f=0.0, \mu=0.6, \theta=45^{o}$

Initiation occurs wherever there is a critical Griffith crack such as a grain boundary in the rock [22], oriented at an angle predicted by equation (2.12). Cracks propagate from each of these flaws as shown in figure 17b. It is the coalescence of these cracks in the region near F_{max} that forms the actual fracture path. The extreme narrowness of the fracture function contours in the vicinity of the fracture initiation point suggests that the initial propagation direction coincides with the minimum gradient of F rather than in the direction predicted by equation (2.12).

A first approximation of the fracture propagation away from the fracture initiation region can also be established on the basis of this contour map. As the force P on the wedge increases, the region in which the fracture criterion, equation (2.13), is satisfied grows. If the prefracture stress field is assumed for the moment to be valid, then the growth of this "damaged" region is described by the contours in figure 16. Extensions of certain critical Griffith cracks within this damaged region coalesce in the manner described above to form the actual fracture path. This proceeds until the fracture either becomes unstable or reaches a boundary.

Note that the contours widen away from the fracture initiation point and the probable fracture path becomes more ambiguous. The prefracture stress field would obviously be altered by the presence of the fracture and damaged region. Thus a more accurate description of the fracture propagation would require determination of the stress

distribution in the fractured medium. It is felt that a better description of this stress distribution will result in fracture contours which are narrower and hence in a less ambiguous fracture path. However, some of this ambiguity may be inherent in the chip formation process as evidenced by the natural scatter in chip geometry in wedge penetration tests [31].

A probable fracture path is shown in figure 16. It is interesting to note that a sizeable shift in the proposed fracture path (away from the fracture initiation region) has little effect on the force versus path length plot, figure 18. Again this is borne out in actual wedge penetration tests, in that there appears to be considerably less scatter in chip formation forces than in chip geometry.

Bieniawski [19] has shown that the transition from stable to unstable fracture growth occurs at the inflection point of the fracture velocity versus fracture length plot. This can be used to establish, at least approximately, this transition point for the present problem. It can be argued that, under constant load rate, the fracture velocity is proportional to $F(\sigma_1, \sigma_2; \mu)$ along the proposed fracture path except for points in the vicinity of incipient fracture and in the region of unstable fracture growth, see figure 18. Thus the inflection point of the $F(\sigma_1, \sigma_2; \mu)$ versus $\hat{s}$ curve is used to establish the transition from stable to unstable growth. Both the positions $\hat{s}$ and value of F, i.e., $\hat{s} = -0.22, 0.61$, and $F = 0.175$ are taken from figure 18. The positions of these inflection points are shown as x's on figure 16. It has already

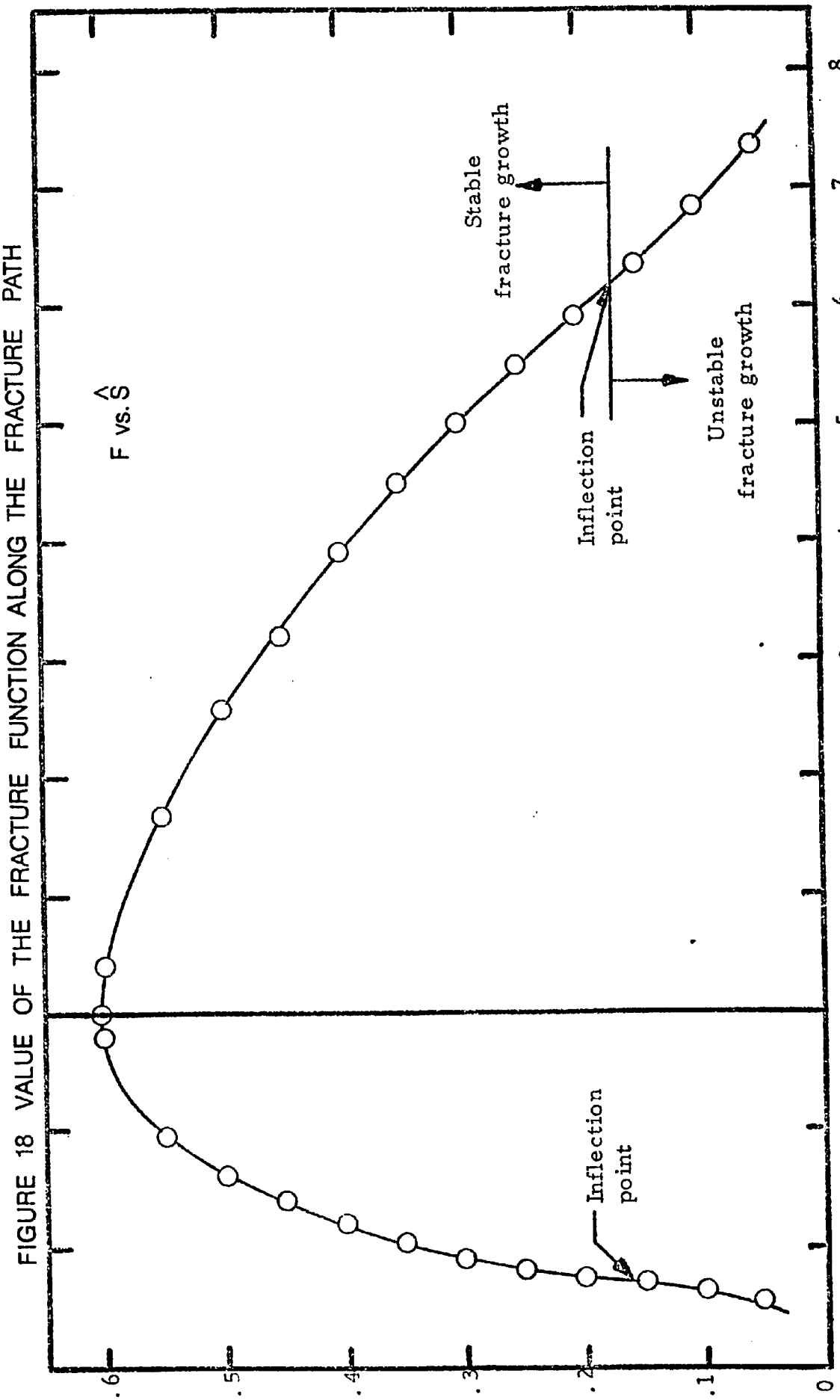


FIGURE 18 VALUE OF THE FRACTURE FUNCTION ALONG THE FRACTURE PATH

been pointed out that the predictions for the latter stages of stable fracture growth are approximate. It is felt, however, that the transition values of $\hat{s}$ and F are reasonable estimates since a fairly large shift in fracture path, figure 16, has little effect on figure 18.

5. Fracture Analysis - Nonlinear Criterion

A Mohr envelope can be represented in the following form:

$$|\bar{\tau}| + \mu(\bar{\sigma}_m)\,\bar{\sigma} = C(\bar{\sigma}_m) \tag{2.14}$$

where $\bar{\tau}, \bar{\sigma}$ are the dimensional shear and normal stresses on some plane and $\mu(\bar{\sigma}_m)$, $C(\bar{\sigma}_m)$ are the slope and $\bar{\tau}$ - intercept of a linear envelope tangent to the Mohr envelope at the point where the mean stress is $\bar{\sigma}_m$, see figure 19. From figure 19, the "material constants" $\mu(\bar{\sigma}_m)$, $C(\bar{\sigma}_m)$ are given by:

$$\mu(\bar{\sigma}_m) = \frac{\bar{\sigma}(\bar{\sigma}_m) - \bar{\sigma}_m}{\bar{\tau}(\bar{\sigma}_m)}$$

$$C(\bar{\sigma}_m) = \bar{\tau}(\bar{\sigma}_m) + \mu(\bar{\sigma}_m)\,\bar{\sigma}(\bar{\sigma}_m) \tag{2.15}$$

The Mohr envelope represents given input data and is further expressible parametrically in terms of the following polynomials:

$$\bar{\tau} = \bar{\tau}(\bar{\sigma}_m) = \sum_{i=0}^{r} \alpha_i \bar{\sigma}_m^i$$

$$\bar{\sigma} = \bar{\sigma}(\bar{\sigma}_m) = \sum_{i=0}^{r} \beta_i \bar{\sigma}_m^i \tag{2.16}$$

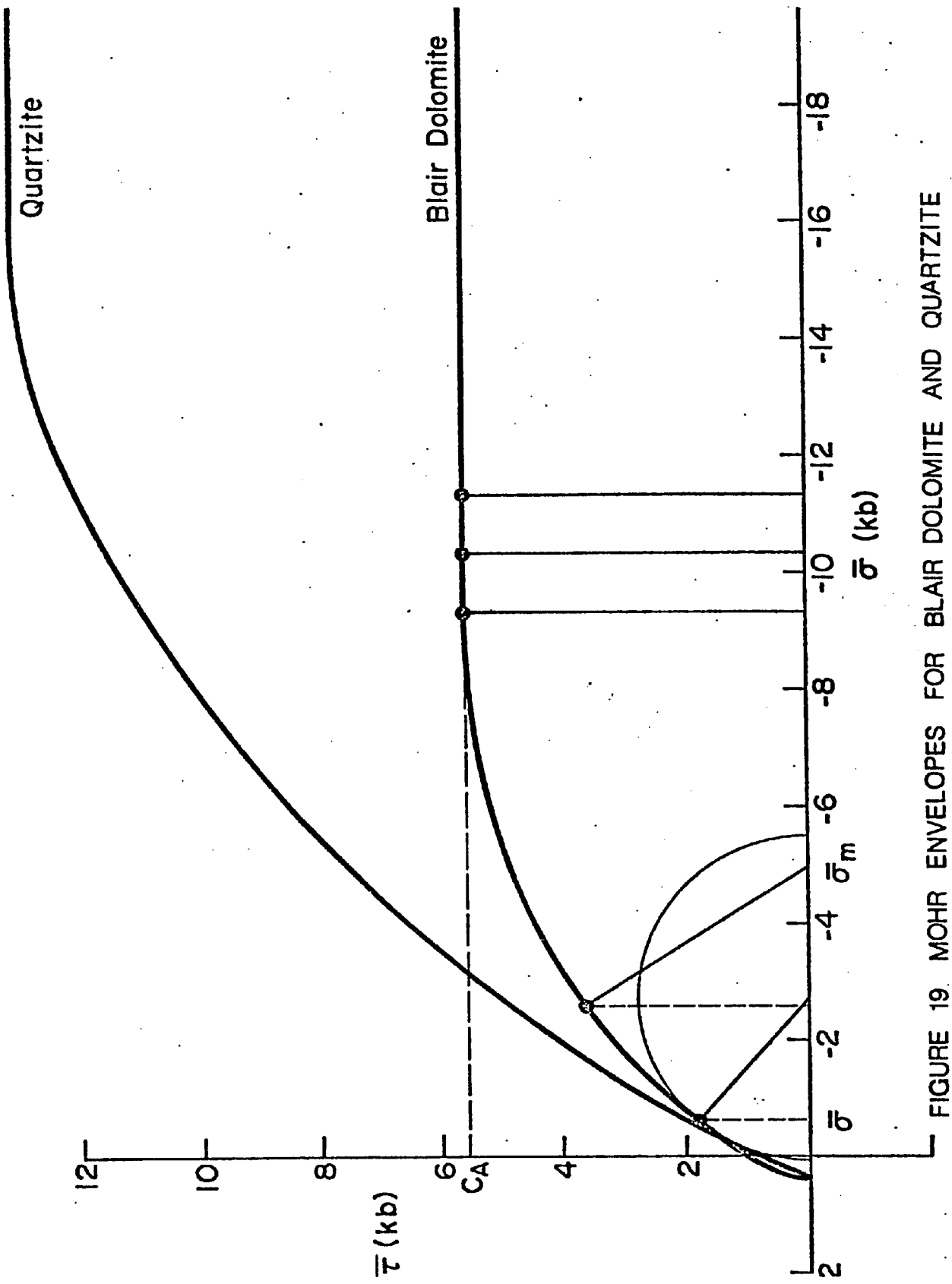


FIGURE 19. MOHR ENVELOPES FOR BLAIR DOLOMITE AND QUARTZITE

The two materials considered are Blair dolomite and quartzite. The Mohr envelope data for these two rocks were obtained by Brace [16] using the special compression specimens mentioned previously which insure a fairly uniform axial stress distribution. With the envelopes given, the constants in equations (2.16) can be found using a least squares fit. Details of this fitting are presented in Appendix C.

The problem of figure 7 will now be reconsidered using the non-linear Mohr criterion instead of the linear Coulomb-Mohr criterion.

If the planes which maximize the left-hand side of equation (2.14) are found and the resulting stresses on these planes expressed in terms of principal stresses, equation (2.14) takes the form:

$$\frac{\mu(\bar{\sigma}_m)}{2}(\bar{\sigma}_1^T + \bar{\sigma}_2^T) + \frac{\sqrt{1+\mu^2(\bar{\sigma}_m)}}{2}(\bar{\sigma}_1^T - \bar{\sigma}_2^T) = C(\bar{\sigma}_m) \qquad (2.17)$$

where $\bar{\sigma}_1^T$, $\bar{\sigma}_2^T$ are the principal stresses with $\bar{\sigma}_1^T > \bar{\sigma}_2^T$ algebraically. The superscript T indicates total stress due to both loading on the truncated face, see figure 7, and hydrostatic pressure. There are two angles for which equation (2.17) is valid,

$$\psi_{1,2} = \gamma_1 \pm \left(\frac{\pi}{4} - \frac{\phi(\bar{\sigma}_m)}{2}\right); \quad \tan\phi(\bar{\sigma}_m) = \mu(\bar{\sigma}_m) \qquad (2.18)$$

where γ_1 is the angle between the x axis and the normal to the first principal plane. The interpretation of the angles $\psi_{1,2}$, with regard to fracture direction, is unclear at present. As was shown in section II.4, these angles do not define the direction of fracture propagation as is commonly believed. These directions are shown in figure 20 and,

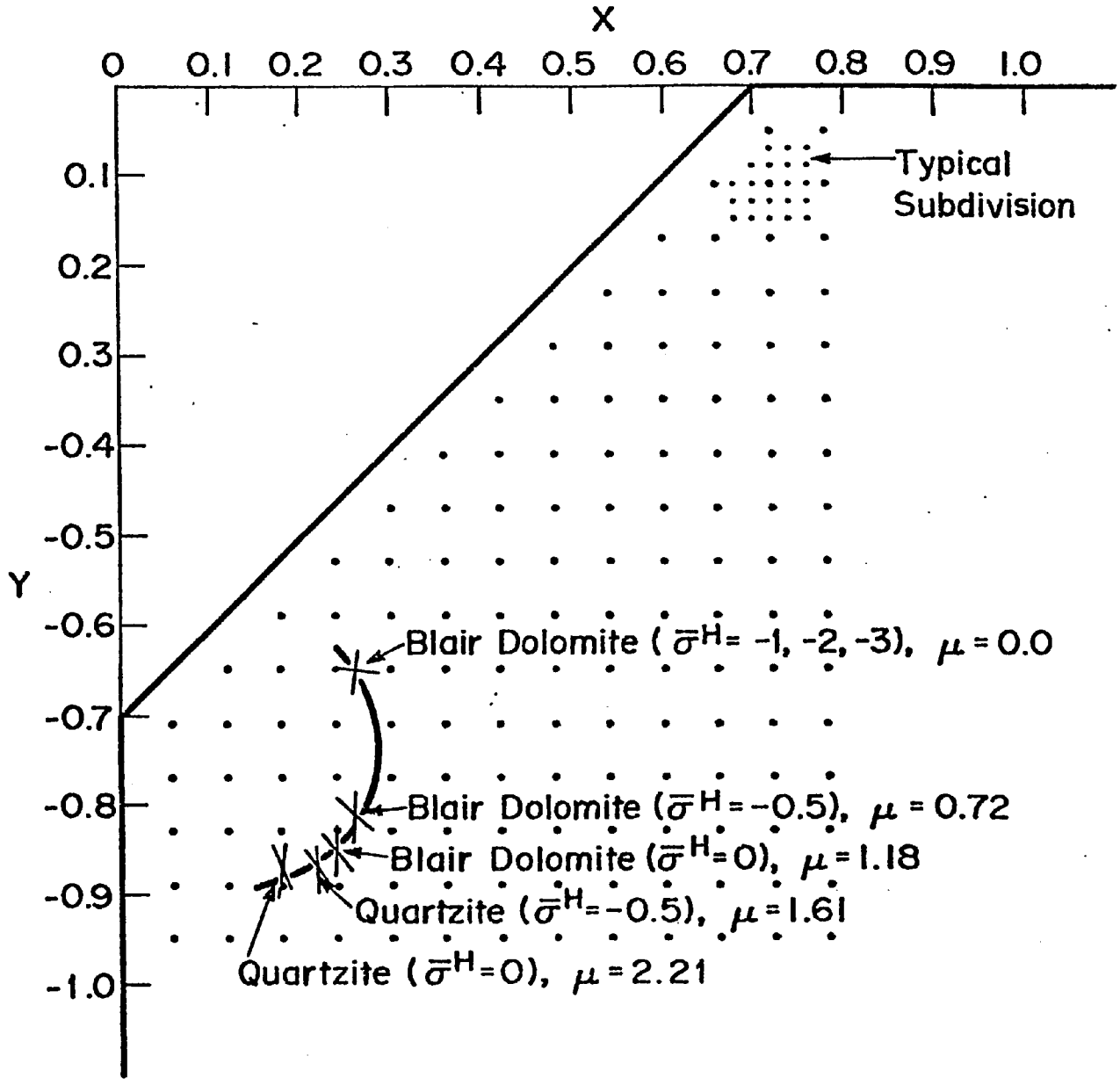


FIGURE 20 FRACTURE INITIATION POINTS FOR BLAIR DOLOMITE AND QUARTZITE, m=5, μ_f=0.0, θ=45°

clearly, are not consistent with known chip formation behavior. The interpretation proposed in section II.4 that these angles represent directions of critically oriented Griffith cracks is not strictly correct either since the Mohr criterion assumes that cracks have already coalesced. These directions are, however, close to those predicted by the Griffith theory.

If the total stress is divided into its component parts:

$$\begin{aligned} \bar{\sigma}_1^T &= \bar{\sigma}_1 + \bar{\sigma}^H \\ \bar{\sigma}_2^T &= \bar{\sigma}_2 + \bar{\sigma}^H \end{aligned} \tag{2.19}$$

and substituted into equation (2.17), the following is obtained:

$$\frac{\mu(\bar{\sigma}_m)}{2}(\bar{\sigma}_1 + \bar{\sigma}_2) + \frac{\sqrt{1+\mu^2(\bar{\sigma}_m)}}{2}(\bar{\sigma}_1 - \bar{\sigma}_2) = C(\bar{\sigma}_m) - \mu(\bar{\sigma}_m)\bar{\sigma}^H \tag{2.20}$$

Nondimensionalizing $\bar{\sigma}_1$, $\bar{\sigma}_2$ with respect to P/L (see figure 7), i.e., $\sigma_1 = \bar{\sigma}_1 L/P$, $\sigma_2 = \bar{\sigma}_2 L/P$, equation (2.20) becomes:

$$\frac{P}{L}\left[\frac{\mu(\bar{\sigma}_m)}{2}(\sigma_1 + \sigma_2) + \frac{\sqrt{1+\mu^2(\bar{\sigma}_m)}}{2}(\sigma_1 - \sigma_2)\right] = C(\bar{\sigma}_m) - \mu(\bar{\sigma}_m)\bar{\sigma}^H \tag{2.21}$$

A "fracture function" can be defined as:

$$\begin{aligned} K(\bar{\sigma}_1^T, \bar{\sigma}_2^T; \mu(\bar{\sigma}_m), C(\bar{\sigma}_m)) &= \frac{P}{L} \\ &= \frac{2[C(\bar{\sigma}_m) - \mu(\bar{\sigma}_m)\bar{\sigma}^H]}{\mu(\bar{\sigma}_m)(\sigma_1 + \sigma_2) + \sqrt{1+\mu^2(\bar{\sigma}_m)}(\sigma_1 - \sigma_2)} \end{aligned} \tag{2.22}$$

This fracture function represents the value of P/L necessary to initiate fracture at a given point in the field. The minimum value of K (K_{min})

occurs at that point in the field at which actual fracture begins. Note that K is defined differently than the fracture function, F, of the linear case.

To find K, the stress field σ_1 , σ_2 must first be determined. The traction distribution is again represented by equation (2.1) and the integral equation procedure outlined in Chapter I is again used. m = 5 and $\mu_f = 0$ are used throughout this analysis.

With σ_1 , σ_2 known throughout the field for P/L = 1, K_{min} can be found using the following iteration equations:

$$K^{(n)} = \left(\frac{P}{L}\right)^{(n)} = \frac{2\left[C^{(n-1)}(\bar{\sigma}_m^{(n-1)}) - \mu^{(n-1)}(\bar{\sigma}_m^{(n-1)})\,\bar{\sigma}^H\right]}{\mu^{(n-1)}(\bar{\sigma}_m^{(n-1)})(\sigma_1+\sigma_2)+\sqrt{1+(\mu^{(n-1)}(\bar{\sigma}_m^{(n-1)}))^2}\,(\sigma_1-\sigma_2)} \qquad \text{(a)}$$

$$\bar{\sigma}_m^{(n)} = (\sigma_1+\sigma_2)\left(\frac{P}{L}\right)^{(n)} + \bar{\sigma}^H \qquad \text{(b)}$$

$$\bar{\tau}^{(n)} = \sum_{i=0}^{r} \alpha_i (\bar{\sigma}_m^{(n)})^i \qquad \text{(c)}$$

$$\bar{\sigma}^{(n)} = \sum_{i=0}^{r} \beta_i (\bar{\sigma}_m^{(n)})^i \qquad \text{(d)}$$

$$\mu^{(n)} = \frac{\bar{\sigma}^{(n)} - \bar{\sigma}_m^{(n)}}{\bar{\tau}^{(n)}} \qquad \text{(e)}$$

$$C^{(n)} = \bar{\tau}^{(n)} + \mu^{(n)}\,\bar{\sigma}^{(n)} \qquad \text{(f)}$$

(2.23)

where the superscripts in parentheses represent the iteration cycle number. Note that σ_1 , σ_2 , $\bar{\sigma}^H$, α_i, β_i are constants throughout the iteration. Assuming initially (n =1) that $\mu^{(0)} = 0$ and $C^{(0)} = C_A$ (the

appropriate asymptotic value of the Mohr envelope, see figure 19), $K^{(1)}$ can be found directly from equation (2.23a). Beginning the iteration from the asymptotic value of the Mohr envelope avoids certain numerical difficulties, i.e., too large an initial value of μ may result in an unbounded first iterant. The value of $K^{(1)}$ determines a new mean stress $\bar{\sigma}_m^{(1)}$ from equation (2.23b), which in turn determines $\bar{\tau}^{(1)}$ and $\bar{\sigma}^{(1)}$ from equations (2.23c) and (2.23d). The new constants $\mu^{(1)}$, $C^{(1)}$ are then determined from equations (2.23e), (2.23f). This iteration procedure continues until the convergence criterion is satisfied:

$$\frac{|K^{(n)} - K^{(n-1)}|}{|K^{(n-1)}|} < \epsilon \qquad (2.24)$$

where ϵ is usually chosen to be 0.01.

This iteration procedure should take place at every point in the field with that point at which K is minimum being the fracture initiation point. To implement this numerically, those points shown as dots in figure 20 were the initially selected field points. (It is necessary to determine K throughout the field as in section II.4 so that contour maps can be drawn.) The iteration procedure was applied at all of these points and the location and value of K_{min} found. The field was then subdivided as before and the iteration process repeated for this smaller field. The new value and location of K_{min} was the one finally selected. The computer program for this nonlinear case is presented in Appendix D.

6. Numerical Results and Discussion

Numerical results for the two materials considered, Blair dolomite and quartzite, are summarized in Table 2.4 and figures 20-22. The confining pressures considered in these results, zero to three kilobars, represent moderate pressures and the materials are still in their brittle state [13].

Fracture initiation locations for the various cases are shown in figure 20. As the confining pressure increases, the fracture initiation point approaches a limiting point nearer the surface. This indicates a decreasing "chip" size with increasing confining pressure. Similar results have been found experimentally by Gnirk and Cheatham [32]. The force necessary to initiate fracture also approaches a limiting value as confining pressure increases as is seen in Table 2.4. An important result is that fracture initiation location for a given traction distribution is solely dependent on μ ($\bar{\sigma}_m$) (location on the Mohr envelope). This conclusion is consistent with the results of section II.4. The small differences in fracture initiation point for Blair dolomite and quartzite at low confining pressure is due to differences in the slopes of their respective Mohr envelopes at low mean stress. Differences in the two materials are illustrated by the relative magnitude of the forces required to initiate fracture (K_{min}), see Table 2.4. Mohr envelope intercepts of the various fracture initiation points of figure 20 are shown on figure 19, for Blair dolomite.

TABLE 2.4

Fracture Initiation Results for Blair Dolomite and Quartzite; $m = 5$, $\mu_f = 0.0$

Material	θ	$\bar{\sigma}^H$ (kb)	K_{min}	$\bar{\sigma}_m$ (kb)
Blair dolomite	45°	-3.0	4.185	-11.3
		-2.0	4.185	-10.3
		-1.0	4.185	- 9.3
		-0.5	3.946	- 4.9
		0.0	2.708	- 2.65
	30°	-2.0	3.035	-10.4
	60°	-2.0	4.774	- 9.5
Quartzite	45°	-0.5	5.278	- 5.25
		0.0	2.953	- 2.48

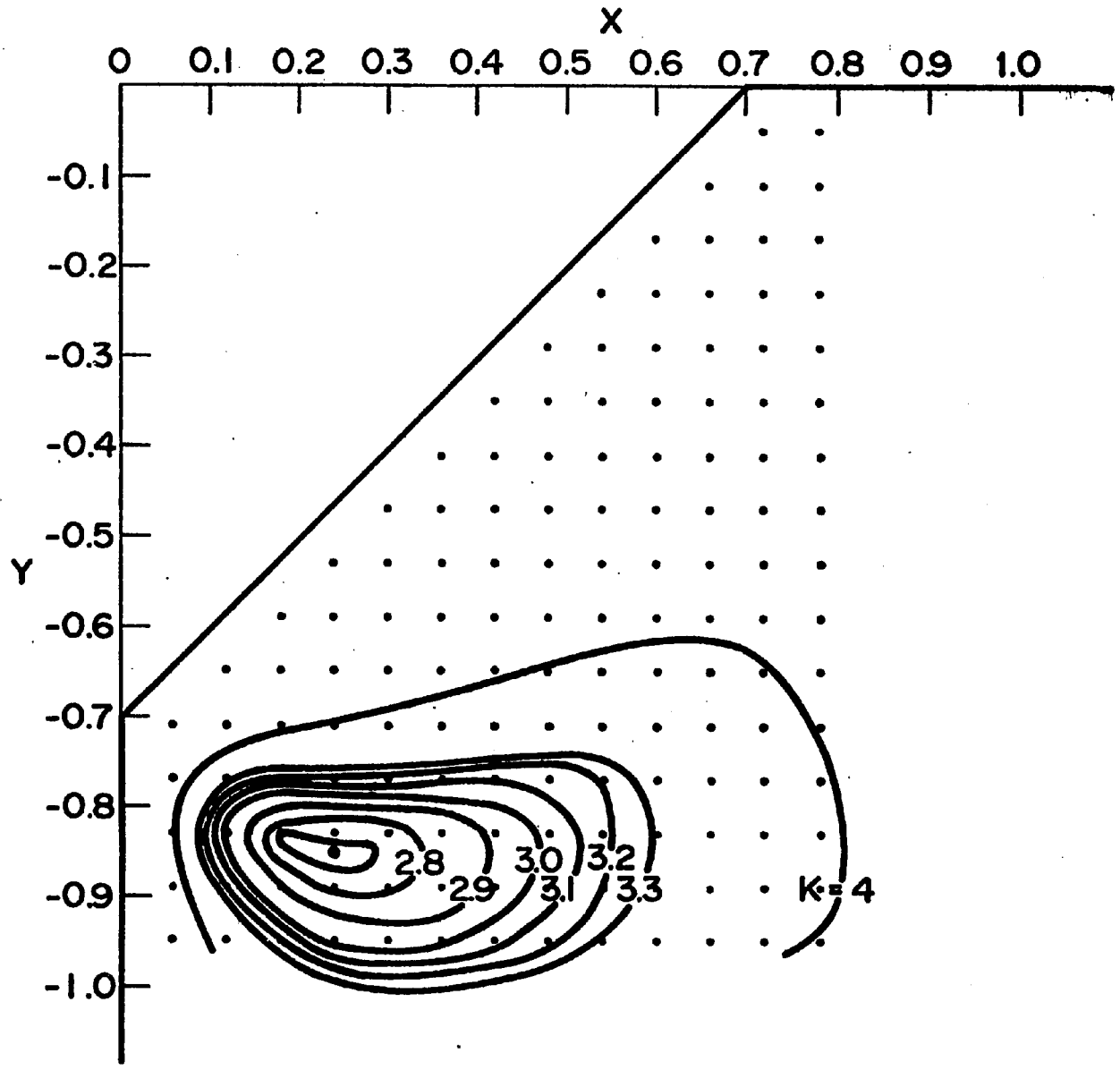


FIGURE 21 CONTOUR MAP FOR BLAIR DOLOMITE AT ZERO CONFINING PRESSURE; $m=5, \mu_f=0.0, \Theta=45^{o}$

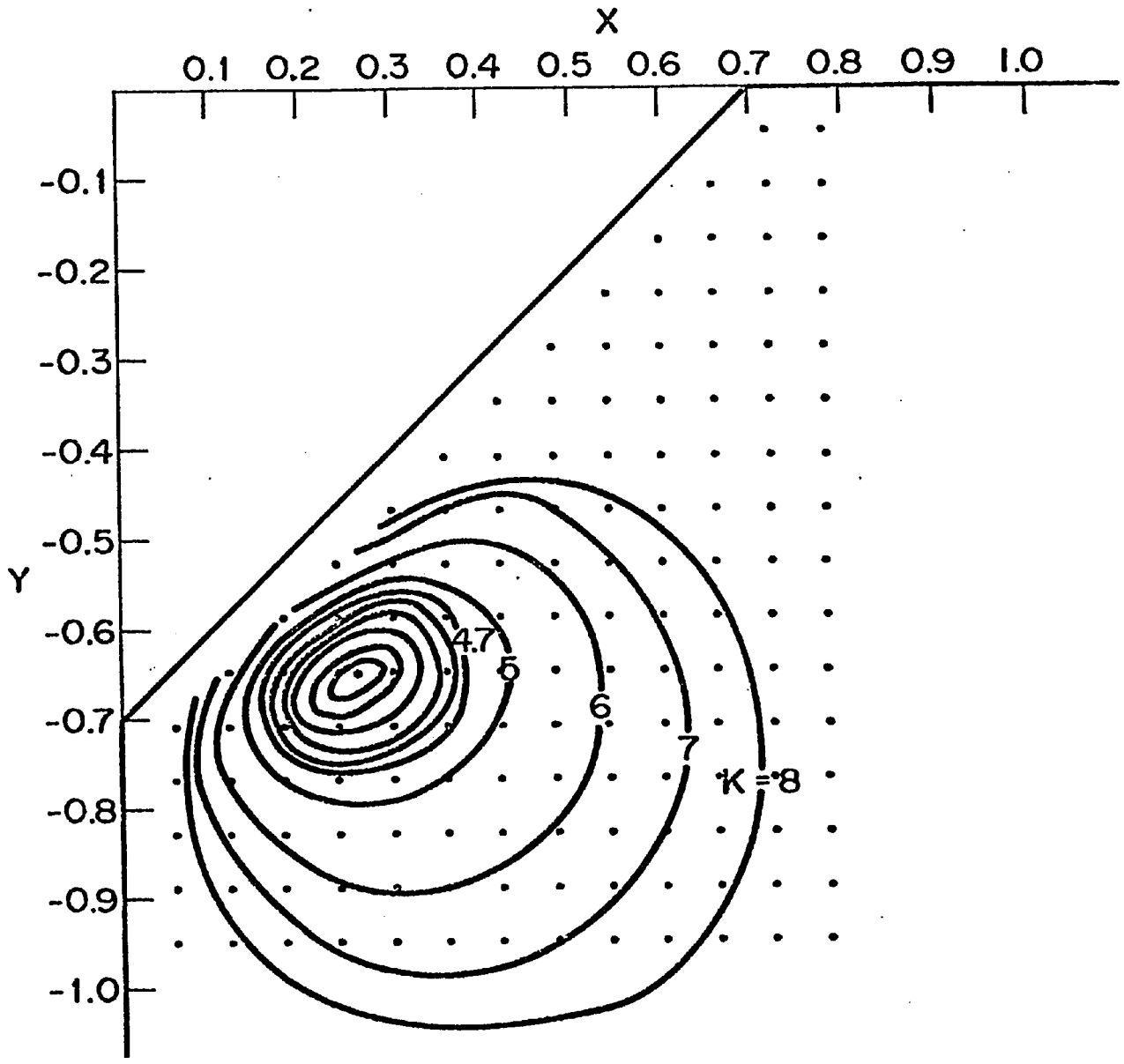


FIGURE 22 CONTOUR MAP FOR BLAIR DOLOMITE AT MODERATE CONFINING PRESSURE (3 kb); $m=5, \mu_f = 0.0, \Theta = 45^{o}$

Effects of wedge angle (truncation angle) on the magnitude of the fracture initiation force for Blair dolomite can also be seen in Table 2.4. As expected, fracture initiation forces increase with increasing wedge angle. For all three wedge angles (and $\bar{\sigma}^H = -2$ kb), the location of the fracture initiation point was identical (within the range of accuracy of the subdivision) relative to the truncated face. This is expected since the fracture initiation point is somewhat removed from the boundaries DB and AC of figure 7.

The analysis (determination of K throughout the field) can also be used to predict initial propagation of the fracture. In figures 21, 22, contour maps of K for Blair dolomite at zero and three kilobars confining pressure are shown. Following the reasoning of section II.4, it is proposed that the initial propagation of fracture follows the minimum gradient of the contour plot. An interesting result is that this proposed path is well-defined at zero confining pressure, figure 21, and less so at higher confining pressure, figure 22. This would indicate more ambiguity in chipping behavior at higher confining pressures. This has also been seen experimentally by Gnirk and Cheatham[32].

CHAPTER III

EXPERIMENT

1. Introductory Remarks

The theoretical analysis presented in Chapter II provides a description of the fracture process from the onset of macrofracture to the formation of a complete fracture surface. This description includes (1) the magnitude of the applied force necessary to initiate macrofracture, (2) the location of this fracture initiation, (3) the initial direction of fracture propagation, (4) an estimate of the ultimate fracture configuration, and (5) an estimate of the applied load necessary to form the complete fracture surface.

An experimental study is now presented, the purpose of which is to evaluate this theory. Briefly, the experiment is as follows. Plaster models, trapezoidal in shape, are loaded in compression (see figure 26). These models are confined between steel plates to eliminate deformation normal to the plane and thus simulate a state of plane strain. As the load is increased, a uniform displacement of surface BA results. The relationship between the total applied load and the displacement of surface BA is recorded on an X-Y plotter and it is shown that the fracture initiation load and the chip formation load can be determined directly from these force-displacement plots. Individual tests are interrupted at load levels between fracture initiation and chip formation and the models are removed from the test fixture

allowing inspection of the fracture development. Thus all five of the descriptive features determined in the theoretical analysis can be measured experimentally and compared to the theoretical expectations.

The presentation of this experimental study will be done in three sections. In section III.2, the experiment will be discussed in greater detail. First, the preparation of the plaster models will be discussed and the relevant material properties will be determined through a series of standard tests. Then the experimental apparatus and the test conditions will be described.

In section III.3, a theoretical analysis similar to those done in Chapter II will be applied to the boundary value problem defined by this experiment. In this analysis, certain quantitative expectations are computed. Then in section III.4, the experimental results are presented and compared to the theoretical predictions found in section III.3. It is found that the theory does predict the location and initial direction of fracture propagation and predicts a fracture initiation load which is within 7% of the average result measured in the series of tests. Furthermore, the theory predicts the general shape of the ultimate fracture surface. It is also shown that, for this problem, an upper bound for the chip formation load can be determined. A very important result found in these experiments is that the fracture growth is definitely stable during at least part of its development, there being a sizeable difference between the initiation and ultimate formation load levels.

2. The Experiment

Plaster models have been used in a number of investigations dealing with fracture of elastic-brittle materials, usually as a model of macroscopic rock behavior [33]. Under triaxial stress conditions, plaster exhibits the same macroscopic fracture characteristics as rock [33] and the Coulomb-Mohr criterion has been used to describe this fracture quantitatively [33, 34]. Plaster has definite advantages over rock as a test material. These include low cost, ready availability, moderate strength, homogeneity and controllable material properties. The fracture characteristics of plaster were first studied by Roark and Hartenburg [35]. Since then, there have been several studies on the effects of various mixture ratios and preparation techniques on the elastic and strength properties of plaster models [33, 36].

The type of plaster used for this study was a medium-set modelling plaster. To insure brittle behavior, the plaster-water ratio chosen was low (70 parts by weight of plaster to 100 parts by weight of water). Tap water at a temperature of 60° F was used. The plaster-water mixture was stirred until all bubbles were removed and the mixture had begun to thicken (10 minutes). The models were cast in aluminum molds which had been greased to facilitate removal. The mixture hardened in 15-20 minutes and was then removed from the mold. The models were cured at room temperature (70° F) for six months. They were stored in an upright position during this time. Prior to testing, the models were carefully machined to insure flat,

smooth faces and a uniform thickness (.450").

The elastic and strength properties of plaster depend on a large number of factors including: type of plaster, storage conditions, plaster-water ratio, preparation techniques, curing conditions and the age of the models at the time of testing. Thus, although these properties have been measured by other investigators, it is necessary to re-measure these parameters using test specimens made from the same plaster as the models, at the same time as the models and cured under the same conditions. Three types of tests were conducted here to determine Young's modulus (E), the compressive strength (S_c) and the tensile strength (S_t). Test specimens were cut from several of the prepared models. The shapes and dimensions of these test specimens are shown in figure 23.

The rectangular-shaped specimen of figure 23a was used to determine the Young's modulus of this plaster mixture. The specimen was loaded uniformly in the axial direction. Two thin Teflon sheets (.005" thick) were placed between the specimen ends and the loading surfaces of the test machine to minimize shear tractions due to friction. Three such tests were run and the results are shown on figure 24. From these results, Young's modulus was computed as:

$$E = \frac{PL}{A\delta} = 4.2 \times 10^5 \text{ psi}$$

The compressive strength was determined using "dogbone" specimens as in figure 23b. Two tests were run. The specimens

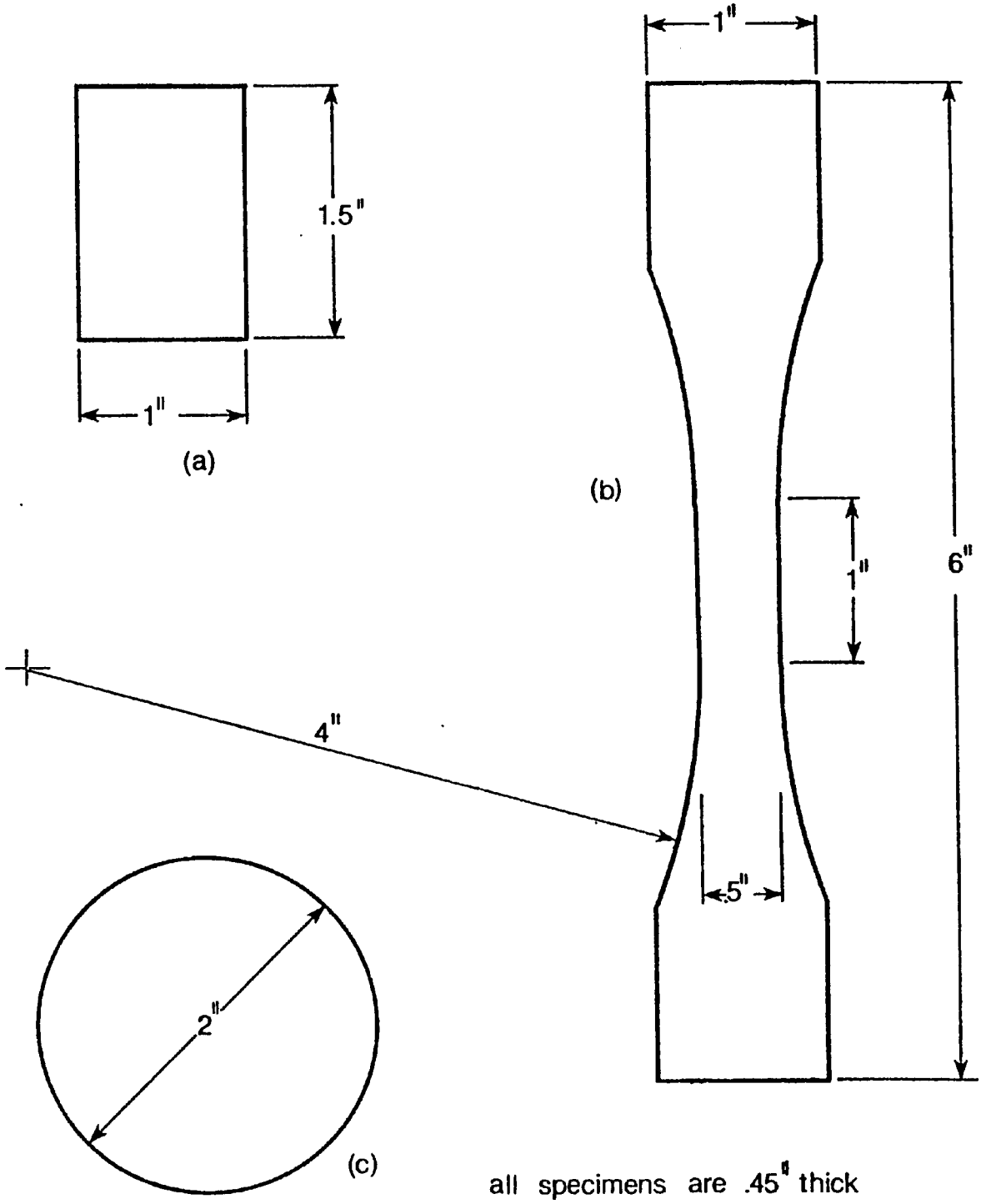


FIGURE 23 TEST SPECIMENS FOR DETERMINATION OF MATERIAL PROPERTIES OF PLASTER

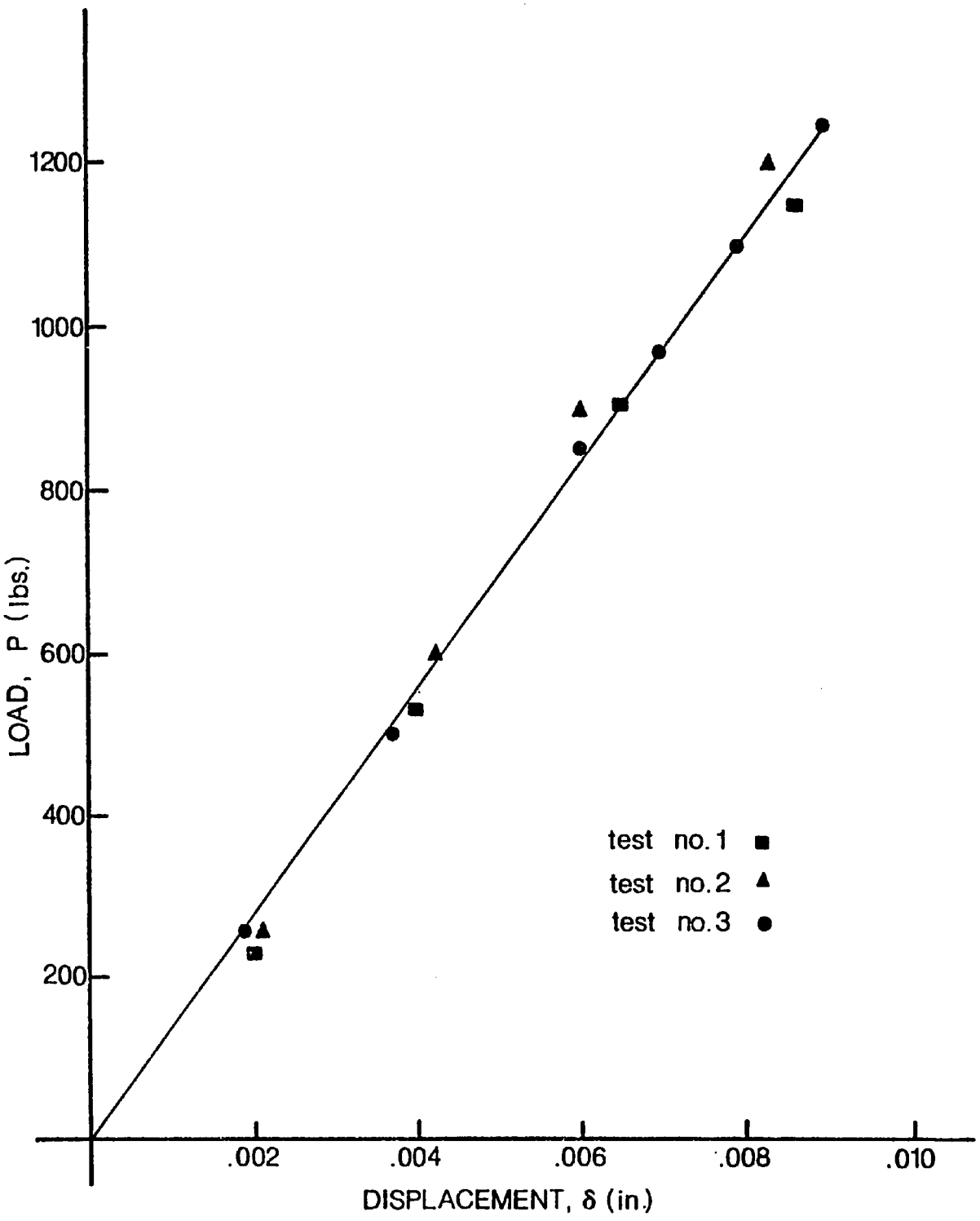


FIGURE 24 "STRESS-STRAIN" CURVE FOR PLASTER

failed at 650# and 625# respectively. Thus, the compressive strength was determined to be

$$S_c = \frac{635\#}{A_t} = 2800\#/in^2$$

where A_t is the area of the "throat" of the test specimen. The Mohr's circle defined by the compressive strength is drawn in figure 25.

The tensile strength was determined from the well-known "Brazilian" test. Disc-shaped specimens, shown in figure 23c were loaded diametrically in compression until they failed by splitting at a load P_B. The tensile strength was then determined from

$$.7\ S_t = \frac{2\ P_B}{\pi\ Dt}$$

where D is the diameter and t is the thickness of the disc. The coefficient, .7, is a correction factor suggested by Fairhurst [37]. Two such tests were run, both giving a result of $P_B = 500\#$. From the above equation:

$$S_t = P_B = 500\#/in^2$$

is the tensile strength. The Mohr's circle described by this test is also drawn in figure 25.

The only relevant material property not measured here is ν, Poisson's ratio. Barron and Larocque [36] found that Poisson's ratio is insensitive to mixture ratios and is always .24 for plaster. Thus in the analysis which follows, $\nu = .24$ will be used.

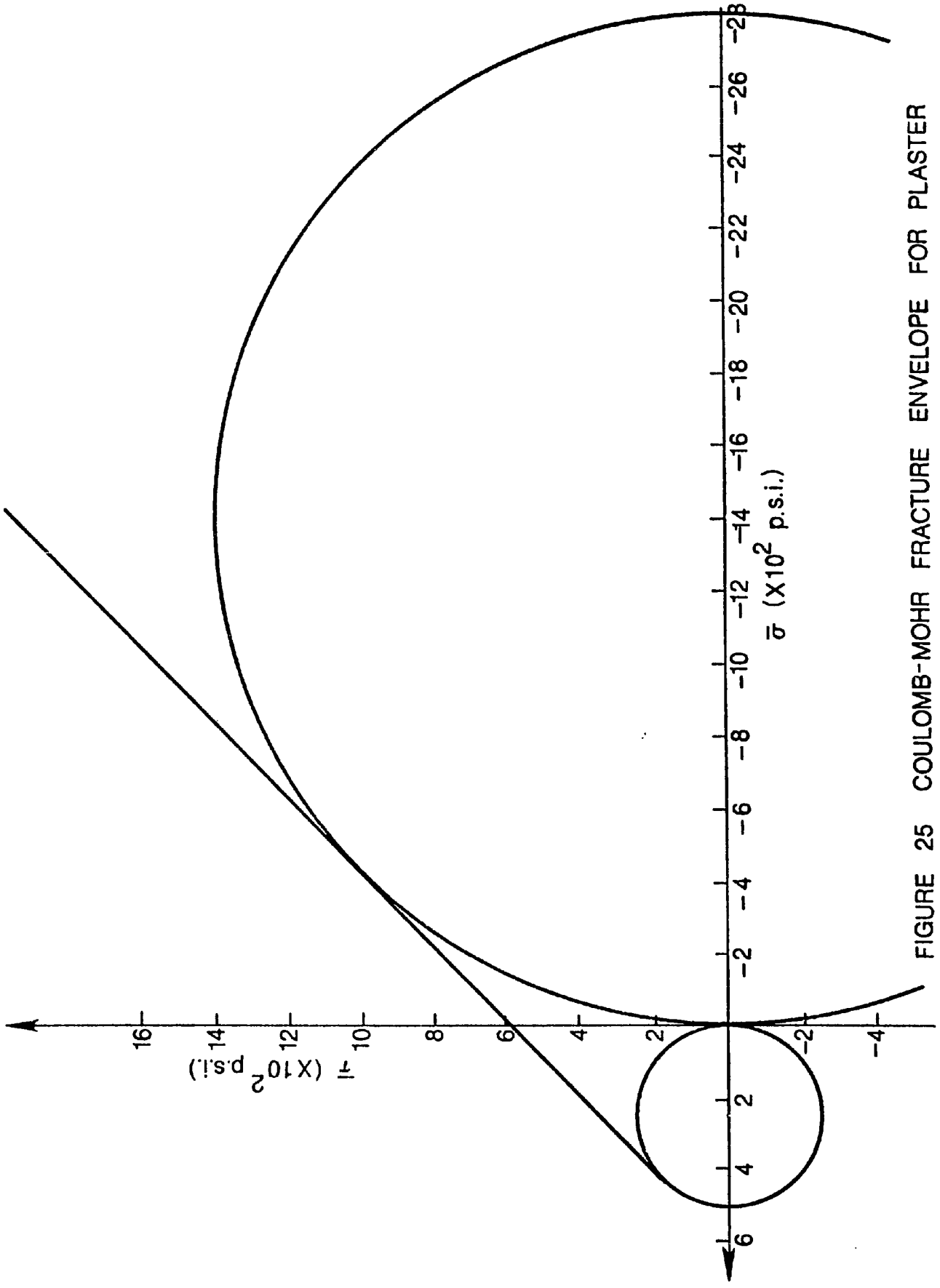


FIGURE 25 COULOMB-MOHR FRACTURE ENVELOPE FOR PLASTER

It will be assumed that the fracture criterion for plaster is linear (Coulomb-Mohr) and thus can be approximated by a line tangent to the Mohr's circles describing the compressive and tensile strengths (see figure 25). The fracture properties are then:

$$\mu = .93$$

$$C = 590 \text{ psi}$$

The loading system is shown in figure 26. The models were confined between two steel plates to insure plane strain conditions. Double layers of .005" thick Teflon sheets were placed between the steel plates and the model faces to eliminate shear forces due to friction. A steel loading platen (.450" wide) was used (as shown in figure 26) to insure uniform contact along the loaded face BA. Double layers of Teflon were also placed between the platen and the face BA. The boundary conditions on face BA therefore consisted of a uniform vertical displacement and zero shear traction. The load was applied quasi-statically (50 pounds per second).

In figure 27, a schematic diagram of the data recording system is shown. The force-displacement plots obtained from this system provide a description of the fracture process. (This will be discussed in greater detail in section III.4.) The LVDT was calibrated using a Starrett dial gage, the difference being no greater than 2%. The load cell was calibrated using dead weight loading to within 5% error.

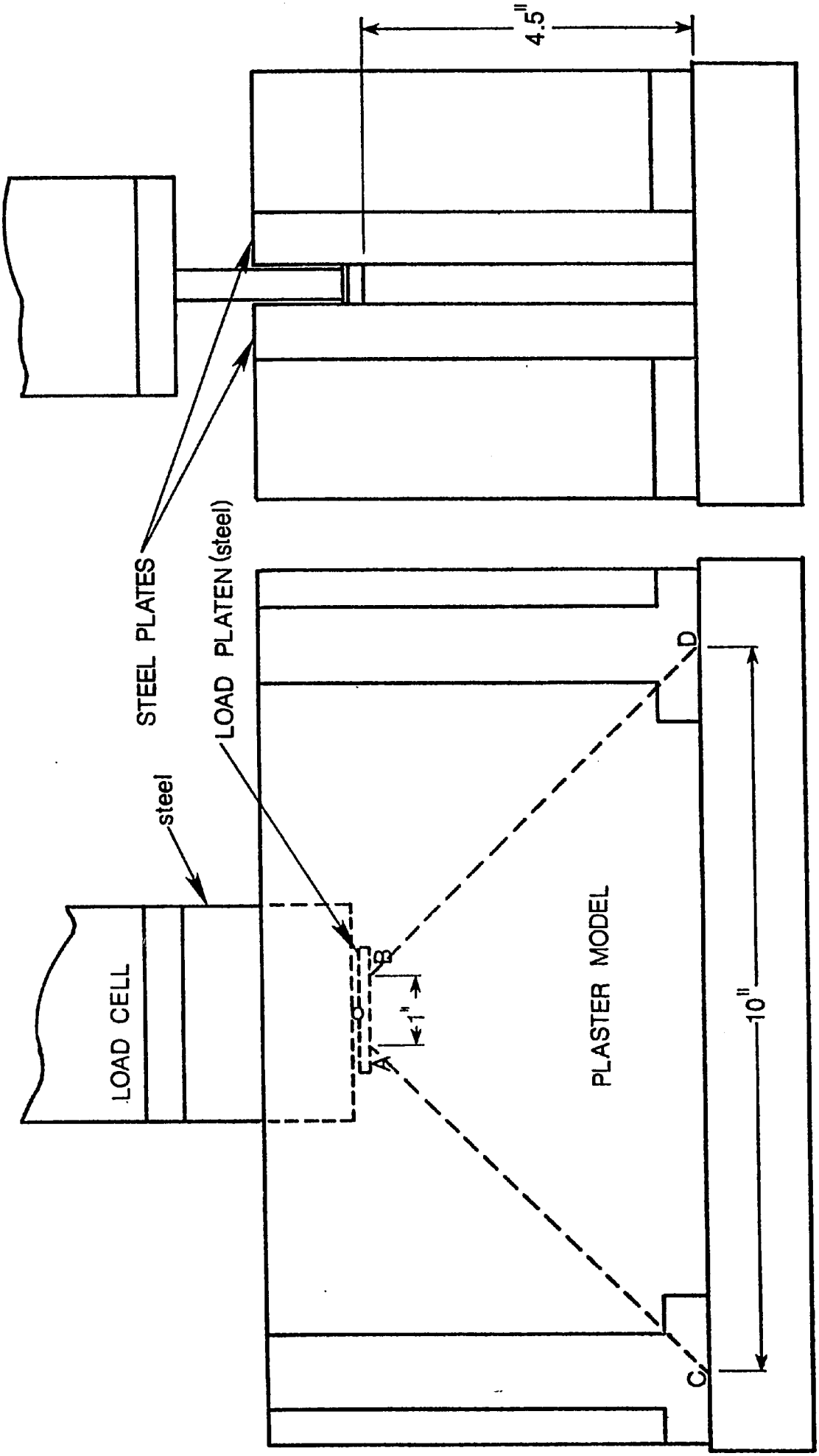


FIGURE 26 PLASTER MODEL IN LOADING FIXTURE

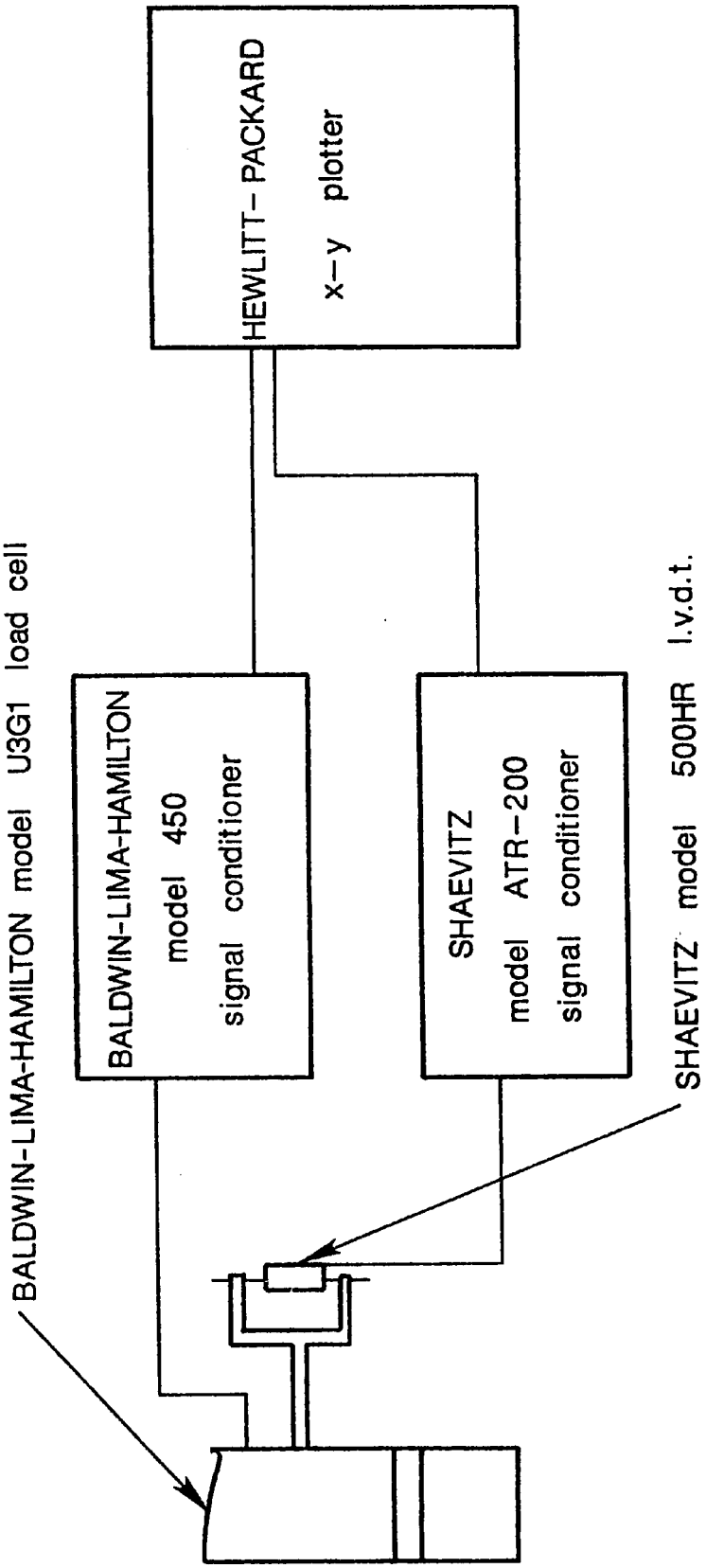


FIGURE 27 SCHEMATIC DIAGRAM OF RECORDING SYSTEM

3. Theoretical Results

A. Uniform Displacement Problem

The problem of interest is the following. A plaster model, the geometry of which is shown in figure 26 and the material properties of which are shown in figures 24 and 25, is subjected to a vertical displacement of the upper surface BA as shown in figure 26. The base of the model CD is constrained in the vertical direction and all other boundary conditions are zero traction conditions. The model is in a state of plane strain.

The integral equation method, as it is formulated in section I.3, is applicable to traction boundary-value problems only. It is therefore necessary to convert this mixed boundary-value problem into a traction boundary-value problem before employing the "fracture" program. This conversion is accomplished through the use of a finite element program developed by Weaver [39] and the results are presented in Appendix E. There, a uniform displacement of the boundary BA is specified and the corresponding traction distribution is determined (a plot of which is drawn in figure E-3). This traction distribution is then used as input into the "fracture" program. The use of the integral method in the "fracture" program greatly facilitates the search procedure for locating the fracture initiation location.

When the traction distribution of figure E-3 and the slope of the fracture envelope $\mu = .93$ are inputed into the "fracture" program,

the fracture function contour map of figure 28 is obtained. Clearly, fracture initiates in the corners, the initial propagation being quite rapid (as evidenced by the proximity of the contours). The propagation commences at $F_{max} = .25$. Thus the fracture initiation load is

$$P_i = \left[\frac{CL}{F_{max}}\right] t = 1060\#$$

where $t = .45"$ is the model thickness, $L = 1"$ is the length of edge BA and $C = 590$ psi.

Once this propagation has begun, the original stress distribution is altered and thus the contour map should be modified. This particular problem is further complicated by the fact that the condition applied to the truncation surface is a displacement rather than a traction condition. Thus as the load on the truncation surface is increased beyond the fracture initiation load, the surface traction distribution itself will be altered. Since the initial damage is confined to the vicinity of the corners, this alteration will probably be a leveling of the non-dimensional traction peaks near the corners (since the stiffness in these regions will be decreased). Thus the first effect on the traction distribution of the propagating fracture would probably be to make this distribution more uniform (see figure E-3). As the fracture continues to propagate, the non-dimensional applied tractions near the corners will continue to decrease and the non-dimensional applied tractions near the center of the surface BA will increase since the undamaged region will be providing more support than the damaged. Clearly the net result of

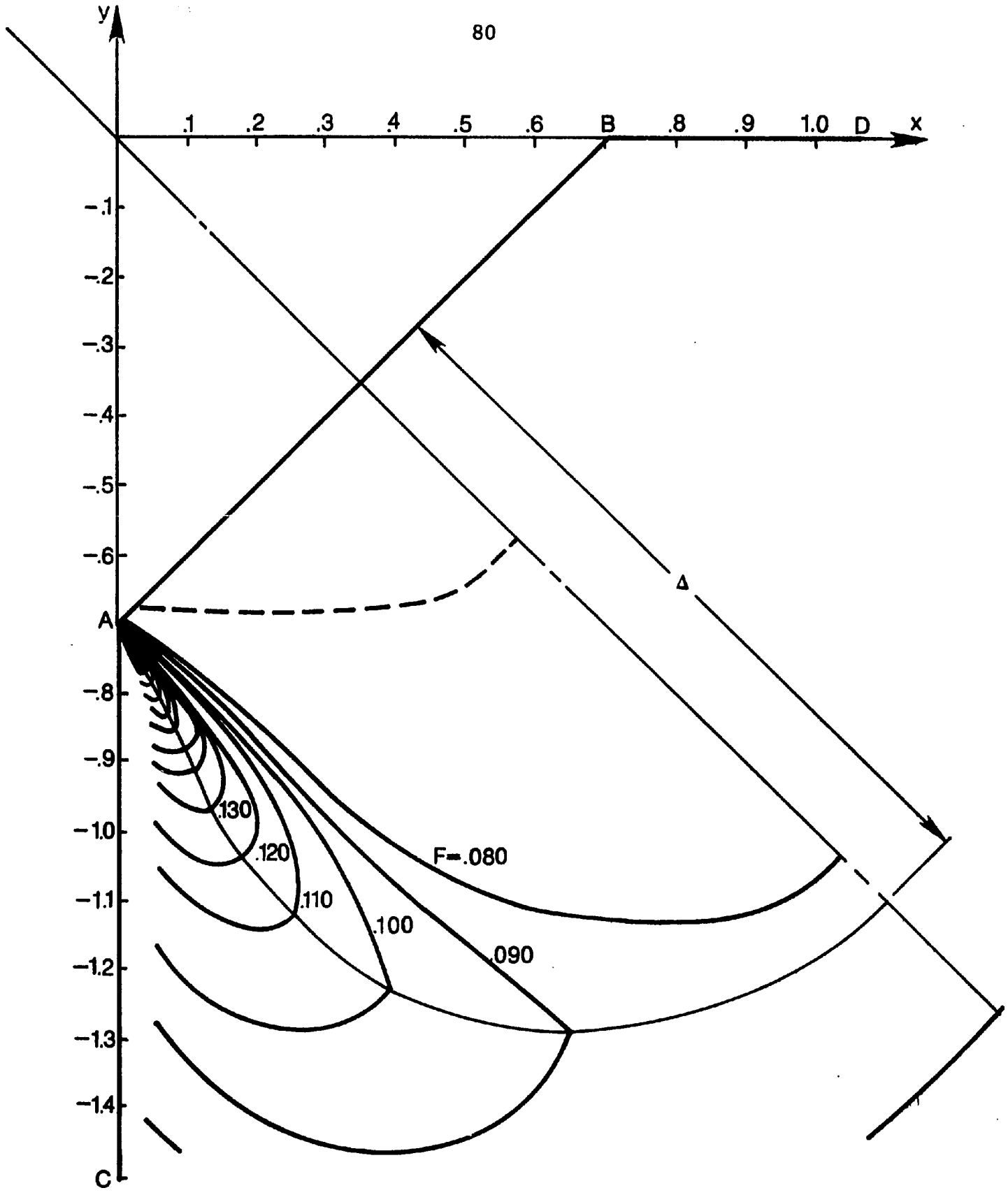


FIGURE 28 CONTOUR MAP FOR PLASTER; UNIFORM DISPLACEMENT OF BA

this shift will be to decrease the predicted chip formation load and the expected chip depth, Δ. Thus results for P_f and Δ obtained from figure 28 should be upper bounds on the actual results. From figure 28:

$$P_f = 3200\#$$

$$\Delta = 1.05''$$

It should be noted that in the region between edge BA and the dotted line in figure 28, the criterion (A. 3) was not satisfied, i.e., at points in this region, the principal stress normal to the plane is not the intermediate stress but is rather the maximum stress algebraically. As a result, some surface damage, oblique to the plane of the problem, may occur in this region, an effect which will be observed in some of the tests run in section III. 4.

B. Uniform Traction Problem

Based on the reasoning of section A, a better upper bound on the chip formation load and the chip geometry can be obtained if the problem is reconsidered for the case of a uniform traction distribution. This has been done and the resulting fracture function contour map is shown in figure 29.

Based on figure 29:

$$P_f = 2400\#$$

$$\Delta = .85''$$

An important feature of figures 28 and 29 is the distinct and unambiguous character of the fracture path in the vicinity of initiation

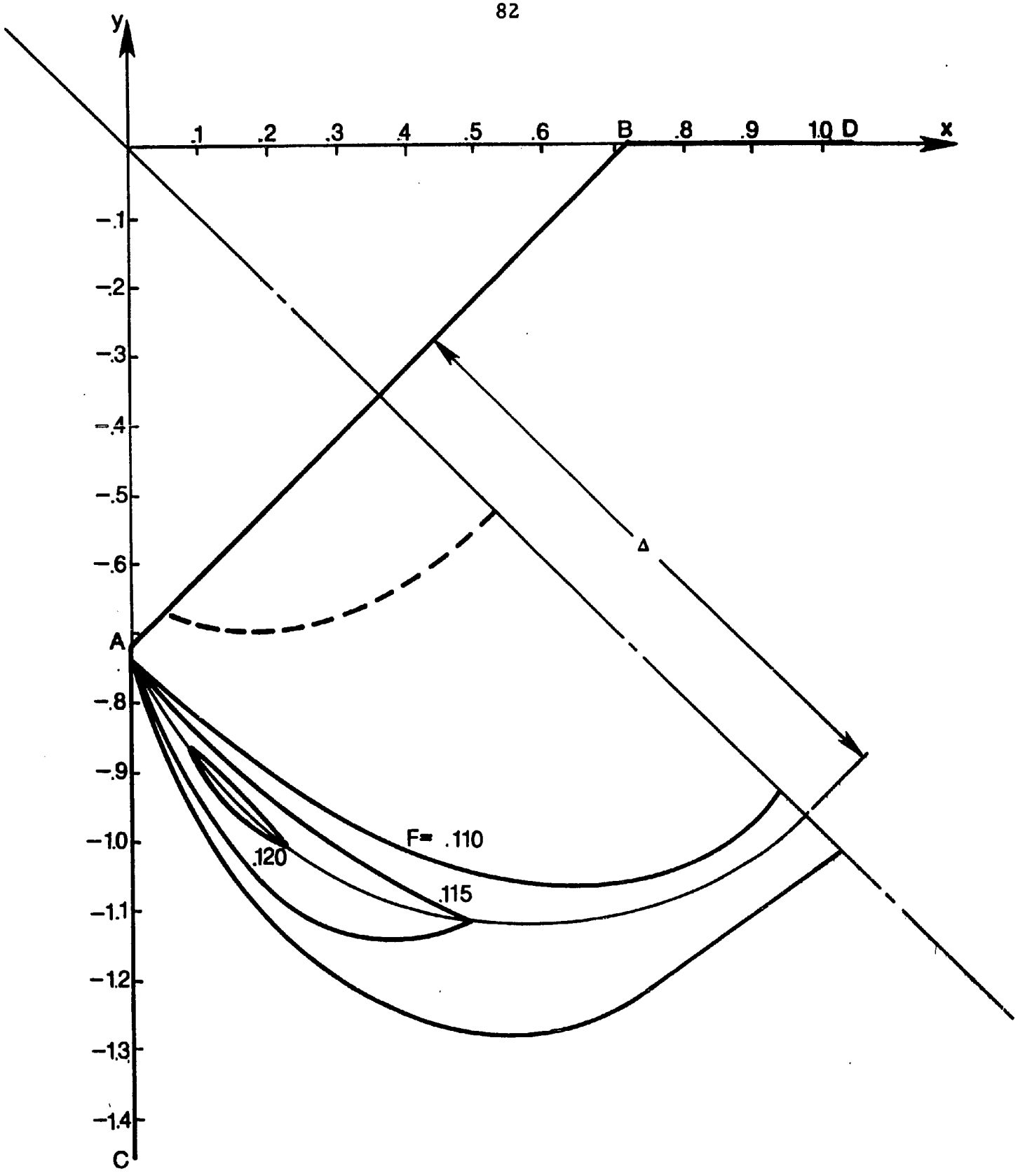


FIGURE 29 CONTOUR MAP FOR PLASTER; UNIFORM TRACTION ALONG BA

as defined by the contours. This is contrasted by the wide contours which represent lower values of the fracture function. As stated earlier, the changing stress field may alter these contours in such a way that the ambiguity would be reduced. It will be seen in the experiment results, however, that the latter stages of the fracture growth is characterized by damage on either side of the macrofracture. Such damage will not be found near the initiation points.

4. Experimental Results

Eight tests were conducted as described in section III.2, the results of which are presented in Table 3.1. As can be seen in the table, the fracture initiation loads range from 1030 pounds (2.8% below the predicted value) to 1250 pounds (18.0% above the predicted value), the average being 1130 pounds (6.6% above the predicted value). A typical force displacement plot is shown in figure 30. The curve is linear up to point A which is to be expected of an undamaged elastic material. At point A, this linear behavior is suddenly disrupted. Test number 7 was stopped at this point and removed from the fixture. The damage was found to be restricted to the corners of the model propagating vertically as predicted. As the load is increased beyond point A, the stiffness of the model continuously decreases as evidenced by the decrease in slope of the force-displacement plot. This decrease in stiffness is due to an increase in damage (propagation of fracture). At point B, there is another sudden disruption of the plot due to the

TABLE 3.1

Experimental Results
(Uniform Displacement Problem)

Test No.	Fracture Initiation Load P_i (pounds)	Chip Formation Load P_f (pounds)	Depth Δ (inches)
1	1030	1400	.65
2	1125	1500	.65
3	1250	1525	.65
4	1050	1400	.60
5	1160	1575	.60
6	1050	1600	.60
7	1200	--	--
8	1180	1500	.55
Average	1130	1500	.61

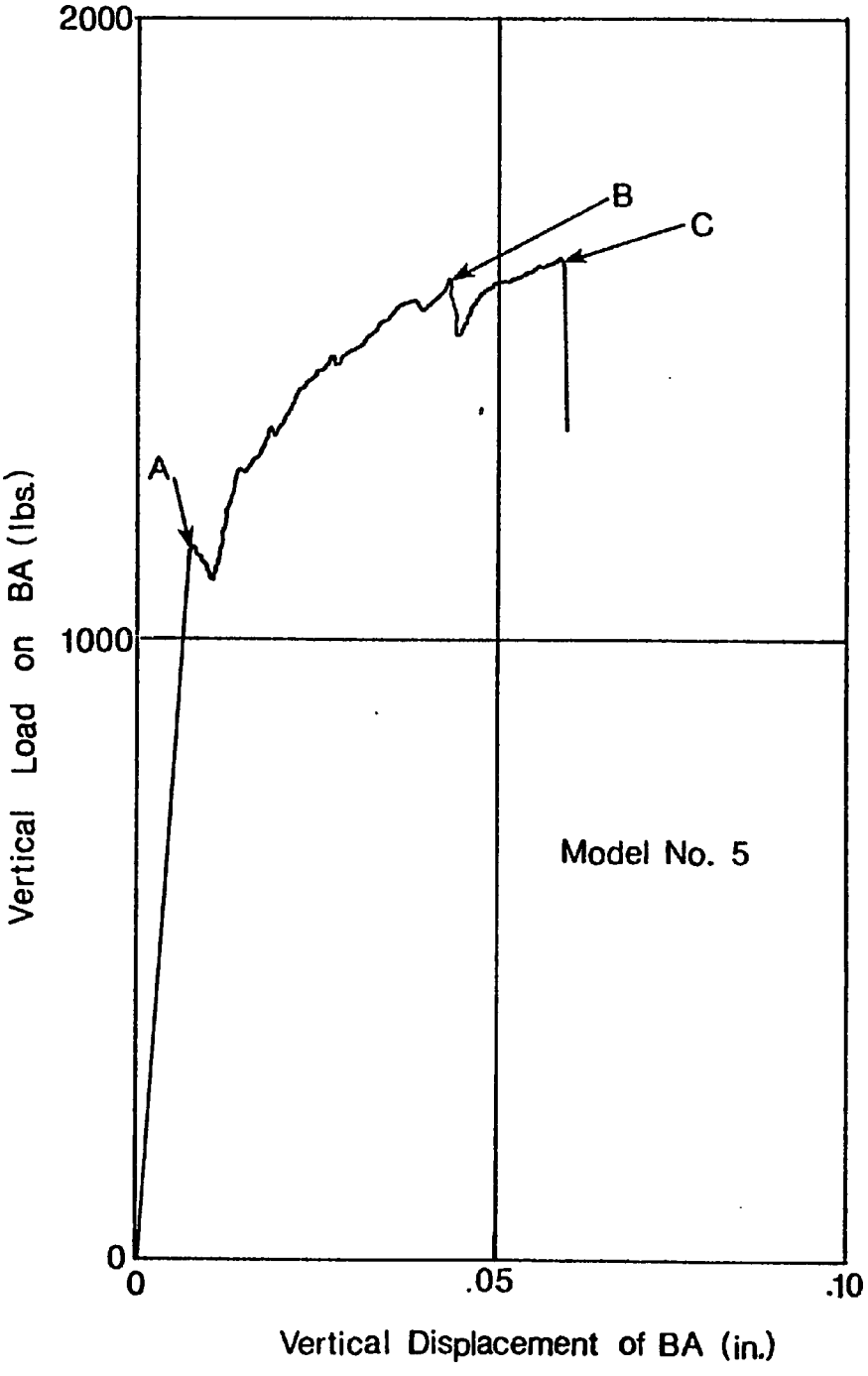


FIGURE 30 TYPICAL FORCE-DISPLACEMENT PLOT OF UNIFORM DISPLACEMENT TEST ON PLASTER MODEL

formation of the chip. Several of the tests were in fact stopped just after point B and removed from the fixture. In each of these models, a completed chip was observed. Upon further increase of the load beyond point B, the completed chip is forced into the model. This chip acts like a wedge which then splits the model in a tensile fracture mode (mode I fracture). This causes structural failure of the model at point C.

In figure 31, the result of a test which was stopped between points B and C is shown. The chip has been removed for clarity. Note the distinct, unambiguous nature of the fracture surface near the corners where it initiated. Subsequent growth is apparently less well defined as evidenced by the extensive damage at the base of the chip and the somewhat ragged surface of the macrofracture itself.

In Table 3.1, two other results are given: the chip formation load, P_f, and the chip depth, Δ. The averages of the seven completed tests are:

$$P_f = 1500\# \qquad \Delta = .61"$$

As expected, these results are less than the uniform traction solution:

$$P_f = 2400\# \qquad \Delta = .85"$$

and the uniform displacement solution:

$$P_f = 3200\# \qquad \Delta = 1.05"$$

It is felt that this result provides a motivation for further development of the theory for later stages of fracture growth. This will be discussed further in the Closure.

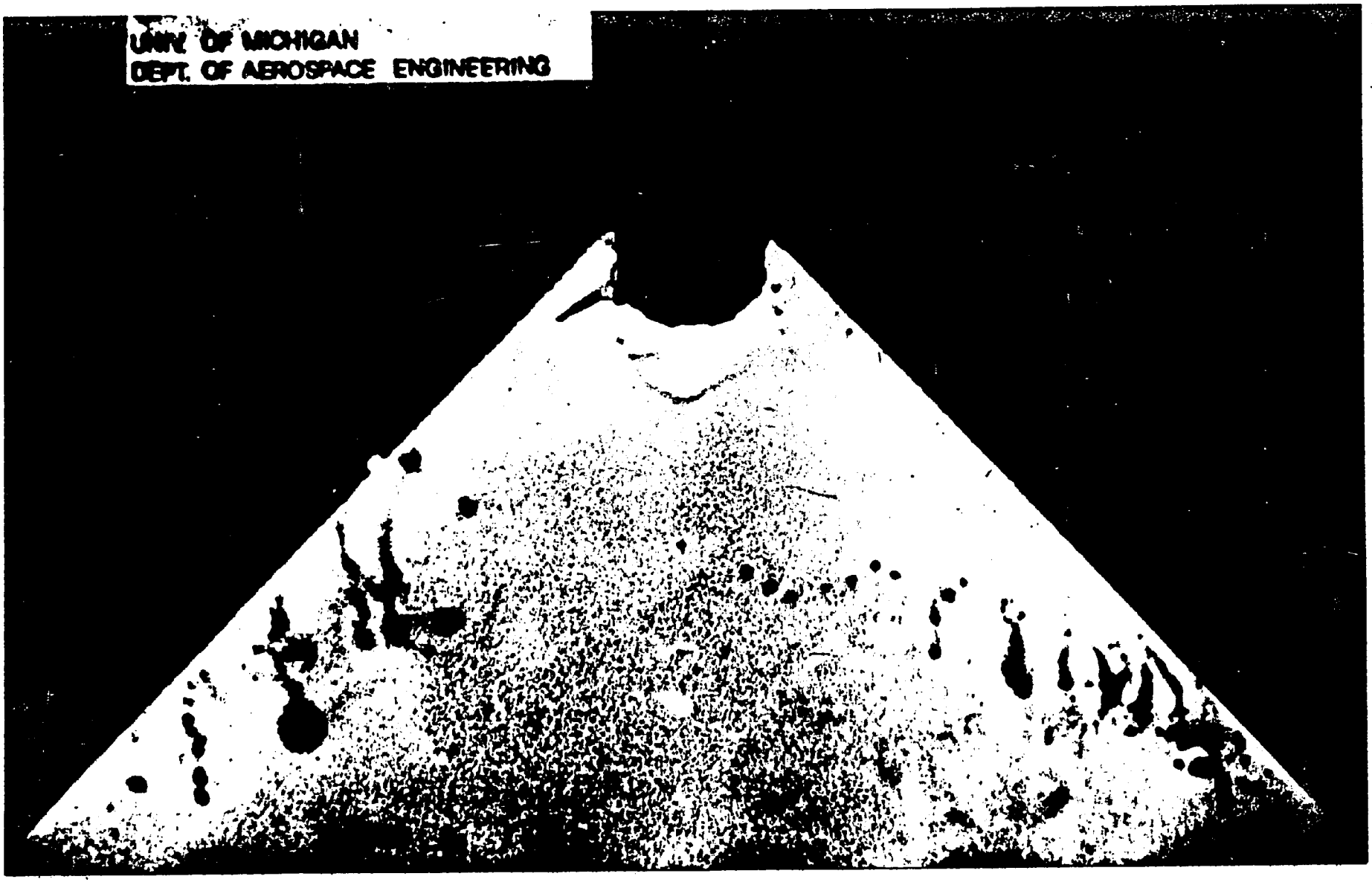


FIGURE 31 PHOTOGRAPH OF COMPLETE CHIP

In all tests, minor surface damage, oblique to the plane, was observed along the edge BA. This damage was confined within the areas defined by the dotted lines in figures 28 and 29, areas in which criterion (A. 3) was not satisfied.

CLOSURE

A theory has been presented for fracture initiation and propagation in isotropic elastic-brittle materials subjected to non-uniform compressive stress fields. It has been shown that macroscopic fracture is formed by the coalescence of cracks which have propagated from critical Griffith flaws in the material. This coalescence, it has been proposed, can best be described quantitatively by the empirical Mohr criterion. Based on this criterion, a "fracture function" has been defined, the contour map of which can be used to analyze the fracture process. Fracture is initiated at the extremum of such a contour map and propagates in the direction of the minimum gradient.

Such an analysis was done for a specific set of boundary-value problems in Chapter II. The problems considered are of practical interest in that they simulate the chipping phase of the penetration of a wedge into an elastic-brittle material. A dimensionless, parametric study was done applicable to materials possessing linear Mohr envelopes (Coulomb-Mohr); the effects of load, geometric and material parameters were considered. The analysis was then extended to the more general nonlinear Mohr envelopes. Results were obtained for two rock materials, quartzite and Blair dolomite at zero to moderate confining pressure.

In Chapter III, an experimental verification of the theory was presented. For the problem considered, the theory accurately predicted the fracture initiation location and load and the initial direction of fracture propagation. It also provided an approximation of the final fracture path. The chip formation load found experimentally was 33% higher than the fracture initiation load, which appears to indicate the presence of stable growth.

It is felt that the experimental results obtained in Chapter III substantiate the theoretical predictions regarding fracture initiation and initial fracture propagation. Furthermore, it is felt that these results provide a strong motivation for future research directed toward modifying the theory to account for the changing stress field due to the presence of the propagating macrofracture and material dilatancy.

APPENDIX A

A NECESSARY AND SUFFICIENT CONDITION FOR THE STRESS NORMAL TO A PLANE IN A STATE OF PLANE STRAIN TO BE THE INTERMEDIATE PRINCIPAL STRESS

The boundary-value problems solved in Chapters II and III were considered to be in the state of plane strain. In such a state, for the problems considered, the stress $\bar{\sigma}_z$ normal to the plane is the intermediate principal stress at each point and therefore does not enter either the Mohr fracture criterion or the modified Griffith theory.

Plane strain does not insure that $\bar{\sigma}_z$ is always intermediate. Thus, in solving plane strain problems of this type, it is important to check each point considered before applying the fracture criterion. In this appendix, a condition is derived with which this check can be made.

Let $\bar{\sigma}_1$ and $\bar{\sigma}_2$ be the principal stresses in the plane at a given point where $\bar{\sigma}_1 > \bar{\sigma}_2$ algebraically. For plane strain

$$\bar{\sigma}_z = \nu (\bar{\sigma}_1 + \bar{\sigma}_2) \tag{A.1}$$

where ν is Poisson's ratio. It will be assumed here that $0 \leq \nu \leq \frac{1}{2}$.* It is desirable to determine the conditions under which $\bar{\sigma}_1 > \bar{\sigma}_z > \bar{\sigma}_2$.

Let $\bar{\sigma}_z = \bar{\sigma}_2 + \sum$; then:

$$\sum = \nu \bar{\sigma}_1 + (\nu - 1) \bar{\sigma}_2 \tag{A.2}$$

---

*To establish uniqueness for linear elasticity, it is necessary that the strain energy density be positive definite. This is satisfied for $-1 \leq \nu \leq 1/2$. Although some crystals exhibit ν values between $-1 \leq \nu \leq 0$, to the author's knowledge, no isotropic materials have this range.

and

$$\bar{\sigma}_1 > \bar{\sigma}_z > \bar{\sigma}_2 \iff \bar{\sigma}_1 - \bar{\sigma}_2 > \sum > 0$$

Consider two cases:

Case I Both stresses compressive, i.e., $0 > \bar{\sigma}_1 > \bar{\sigma}_2$

Then $|\bar{\sigma}_2| > |\bar{\sigma}_1|$.

Let $\bar{\sigma}_1 = - |\bar{\sigma}_1|$ and $\bar{\sigma}_2 = - |\bar{\sigma}_2|$.

Equation (A.2) becomes:

$$\sum = - \nu |\bar{\sigma}_1| + (1 - \nu) |\bar{\sigma}_2|$$

Now $1 - \nu \geq \nu$

$$\therefore \quad (1 - \nu) |\bar{\sigma}_2| > \nu |\bar{\sigma}_1|$$

$$\therefore \quad \sum > 0$$

Equation (A.2) can be rewritten as:

$$\sum = \bar{\sigma}_1 - \bar{\sigma}_2 + (\nu - 1) \bar{\sigma}_1 + \nu \bar{\sigma}_2 = \bar{\sigma}_1 - \bar{\sigma}_2 + (1 - \nu) |\bar{\sigma}_1| - \nu |\bar{\sigma}_2|$$

Therefore

$$\sum < \bar{\sigma}_1 - \bar{\sigma}_2 \iff (1 - \nu) |\bar{\sigma}_1| - \nu |\bar{\sigma}_2| < 0 \iff (1 - \nu) |\bar{\sigma}_1| < \nu |\bar{\sigma}_2|$$

or

$$|\bar{\sigma}_2| > \frac{1 - \nu}{\nu} |\bar{\sigma}_1| \qquad \text{(A.3)}$$

Thus, when both principal stresses at a point in the plane are compressive, condition (A.3) must be satisfied for the normal stress to be intermediate.

Case II One stress compressive and one tensile, i.e., $\bar{\sigma}_1 > 0 > \bar{\sigma}_2$

Let $\bar{\sigma}_1 = |\bar{\sigma}_1|$ and $\bar{\sigma}_2 = - |\bar{\sigma}_2|$

Equation (A.2) becomes:

$$\sum = \nu\,|\bar{\sigma}_1| + (1 - \nu)|\bar{\sigma}_2|$$

Now $1 - \nu > 0$

$\nu > 0$

$\therefore \quad \sum > 0$

Equation (A.2) can be rewritten as:

$$\sum = \bar{\sigma}_1 - \bar{\sigma}_2 + (\nu - 1)\,\bar{\sigma}_1 + \nu\,\bar{\sigma}_2 = \bar{\sigma}_1 - \bar{\sigma}_2 + (\nu - 1)\,|\bar{\sigma}_1| - \nu\,|\bar{\sigma}_2|$$

Now $\nu - 1 < 0$

$\nu > 0$

$\therefore \quad \sum < \bar{\sigma}_1 - \bar{\sigma}_2$

Thus, when one in-plane principal stress is tensile and the other in-plane principal stress is compressive, the principal stress normal to the plane at that point is always intermediate under plane strain conditions.

APPENDIX B

"FRACTURE" COMPUTER PROGRAM-
LINEAR FRACTURE ENVELOPE

A computer program was employed for the numerical computation of the stress field and "fracture function." A listing of that program for the linear (Coulomb-Mohr) case is presented in this appendix.

A. Input Data

The following information must be provided as input (all values are dimensionless unless otherwise designated):

NML	- total number of subdivisions on the boundary
NDB, NBA	- the number of these subdivisions allotted to boundary segments DB and BA, respectively (see figure 9)
(S (I), I = 1, NML)	- the lengths of the boundary subdivisions beginning with the right-most on boundary DB and listing counter-clockwise
PC	- degree of accuracy desired in the iteration of equations (1.15)
AL	- value of the convergence parameter, α, in equation (1.16)
NFPI	- the number of field points at which the stress tensor components and "fracture function" are to be computed

(XF (I), YF (I), I = 1, NFPI) - coordinates of these field points with respect to the coordinate system designated in figure 7

DIV - Once the "fracture function," $F(\sigma_1, \sigma_2; \mu)$, has been evaluated at each of the specified field points, the computer determines at which of these points F is a maximum. A grid is then set up about this point as in figure B-1, the computations are repeated and a new location of maximum F is determined. A minor adjustment to the program would allow for further subdivisions and subsequently better accuracy.

THETA - the half wedge angle, θ

MUF - coefficient of friction on loaded surface, μ_f

M - form parameter, m, (see equation (2.1))

MU - slope of the Coulomb-Mohr envelope, μ

B. Output Data

The following information is obtained as output (again, all values are dimensionless unless otherwise designated):

(LOCT (I), XB (I), YB (I) I = 1, NML) - Given the number and lengths of the boundary subdivisions, the computer determines the coordinates of the center point of each and assigns to each a location number. This

numbering begins at the right-most subdivision on the boundary segment DB and proceeds consecutively in the counter-clockwise direction (see figure 9).

(PX (I), PY (I) I = 1, NML) - Components of the real traction on the boundary, represented by the concentrated real load at the center of each one of the subdivisions. The real traction distribution is of the form indicated in equation (2.1) and is non-dimensionalized as in equation (1.11). The components for a given subdivision, P_{xi}, P_{yi}, are then found by integration of the traction over that subdivision as in equation (1.13).

(PXS (I), PYS (I), I = 1, NML) - Components of the fictitious traction on the boundary, represented by the concentrated load, P^*_{xi}, P^*_{yi}, at the center of each one of the subdivisions. These are computed by iteration as indicated in equation (1.16).

(LOCT (I), XF (I), YF (I) I = 1, NFP) - The computer also assigns a location number to each of the field points. The set of specified field points (input) are numbered from 1 to NFPI whereas the points of the grid (figure B-1) are numbered from (NFPI + 1) to NFP = (NFPI + 22).

(SGMAXX (I), SGMAYY (I) SGMAXY (I), I = 1, NFP) - Components of the stress tensor, σ_{xx}, σ_{yy}, σ_{xy}, at each of the field points. These are computed by the use of equation (1.17).

(SGMA1 (I), SGMA2 (I) ALPHA1 (I), ALPHA2 (I) I = 1, NFP) - Principal stresses and their directions at these same field points. SGMA1 (I) is the larger stress in an algebraic sense.

(F (I), PSI1 (I), PSI2 (I) I = 1, NFP) - The "fracture function," F (equation (2.13)) and the angles between the x-axis and the normals to the critical planes, ψ_1 and ψ_2 (equation (2.12)) at each field point.

FMAX - Maximum value of F; value of F at location of incipient fracture.

The computer program follows.

```
C ISOTROPIC CASE - LINEAR CRITERION
      REAL MU
      REAL MUF
      DIMENSION S(96),XB(96),YB(96),ANX(96),ANY(96),
     1 PX(96),PY(96),B1(96,96),B2(96,96),B3(96,96),
     2 PXS(96),PYS(96),PXSN(96),PYSN(96),SUMX(96),
     3 SUMY(96),XF(267),YF(267),SGMAXX(267),SGMAYY(267),
     4 SGMAXY(267),SGMAA(267),SGMAB(267),SGMA1(267),
     5 SGMA2(267),ALPHAA(267),ALPHAB(267),ALPHA1(267),
     6 ALPHA2(267),F(267),PSI1(267),PSI2(267),LOCT(267)
 100  FORMAT ('1')
 201  FORMAT ('0LOCT',19X,'XB',35X,'YB'/'0'/
     1 (I4,8X,E20.8,16X,E20.8))
 301  FORMAT ('0LOCT',19X,'PX',35X,'PY'/'0'/
     1 (I4,8X,E20.8,16X,E20.8))
 401  FORMAT ('0CICLE =',I4/'0'/'LOCT',18X,'PXS',34X,
     1 'PYS'/'0'/(I4,8X,E20.8,16X,E20.8))
 501  FORMAT ('0LOCT',19X,'XF',35X,'YF'/'0'/
     1 (I4,8X,E20.8,16X,E20.8))
 601  FORMAT ('0LOCT',17X,'SGMAXX',30X,'SGMAYY',30X,
     1 'SGMAXY'/'0'/(I4,8X,E20.8,16X,E20.8,16X,E20.8))
 701  FORMAT ('0LOCT',17X,'SGMA1',21X,'SGMA2',20X,
     1 'ALPHA1',20X,'ALPHA2'/'0'/(I4,8X,E20.8,6X,E20.8,
     2 6X,E20.8,6X,E20.8))
 801  FORMAT ('0LOCT',19X,'F',34X,'PSI1',32X,'PSI2'/'0'/
     1 (I4,8X,E20.8,16X,E20.8,16X,E20.8))
 901  FORMAT ('0FMAX =',E20.8)
      NAMELIST/DATA1/NML,NDB,NBA,S,PC,AL,NFPI,XF,YF,DIV,
     1 THETA,MUF,M
      NAMELIST/DATA2/ MU
      READ (5,DATA1)
      WRITE (6,DATA1)
      DO 2 I=1,267
    2 LOCT(I)=I
C
C DETERMINATION OF XB(I) AND YB(I)
      XD=0.0
      DO 3 I=1,NDB
    3 XD=XD+S(I)
      II=NDB+1
      JJ=NDB+NBA
      DO 4 I=II,JJ
    4 XD=XD+S(I)*SIN(THETA)
      XB(1)=XD-S(1)/2.0
      YB(1)=0.0
      DO 5 I=2,NDB
      XB(I)=XB(I-1)-(S(I)+S(I-1))/2.0
    5 YB(I)=0.0
      XB(NDB+1)=XB(NDB)-S(NDB)/2.0-S(NDB+1)*SIN(THETA)/
     1 2.0
```

```
      YB(NDB+1)=-S(NDB+1)*COS(THETA)/2.0
      II=NDB+2
      JJ=NDB+NBA
      DO 6 I=II,JJ
      XB(I)=XB(I-1)-(S(I)+S(I-1))*SIN(THETA)/2.0
      YB(I)=YB(I-1)-(S(I)+S(I-1))*COS(THETA)/2.0
    6 CONTINUE
      II=NDB+NBA+2
      XB(II-1)=0.0
      YB(II-1)=YB(II-2)-S(II-1)/2.0-S(II-2)*COS(THETA)/2.0
      DO 7 I=II,NML
      XB(I)=0.0
      YB(I)=YB(I-1)-(S(I)+S(I-1))/2.0
    7 CONTINUE
      WRITE (6,100)
      WRITE (6,201) (LOCT(I),XB(I),YB(I), I=1,NML)
C
C DETERMINATION OF ANX(I) AND ANY(I)
      DO 8 I=1,NDB
      ANX(I)=0.0
    8 ANY(I)=1.0
      II=NDB+1
      JJ=NDB+NBA
      DO 9 I=II,JJ
      ANX(I)=-COS(THETA)
    9 ANY(I)=SIN(THETA)
      II=NDB+NBA+1
      DO 10 I=II,NML
      ANX(I)=-1.0
   10 ANY(I)=0.0
      PI=3.1415927
C
C DETERMINATION OF PX(I) AND PY(I)
C     M CANNOT EXCEED 5
      DO 11 I=1,NDB
      PX(I)=0.0
   11 PY(I)=0.0
      II=NDB+NBA+1
      DO 12 I=II,NML
      PX(I)=0.0
   12 PY(I)=0.0
      II=NDB+1
      JJ=NDB+NBA
      ETA=0.0
      PHIF=ATAN(RUF)
      D1N=SIN(THETA+PHIF)
      D1D=COS(THETA+PHIF)
      D1=D1N/D1D
      DO 19 I=II,JJ
      A=ETA
```

```
      ETA=ETA+S(I)
      B=ETA
      SA=SIN(2.0*PI*A)
      SB=SIN(2.0*PI*B)
      CA=COS(2.0*PI*A)
      CB=COS(2.0*PI*B)
      SA1=SA/(2.0*PI)
      SB1=SB/(2.0*PI)
      SA2=SA/(8.0*(PI**3))
      SB2=SB/(8.0*(PI**3))
      SA3=SA/(32.0*(PI**5))
      SB3=SB/(32.0*(PI**5))
      CA1=CA/(4.0*(PI**2))
      CB1=CB/(4.0*(PI**2))
      CA2=CA/(16.0*(PI**4))
      CB2=CB/(16.0*(PI**4))
      CA3=CA/(64.0*(PI**6))
      CB3=CB/(64.0*(PI**6))
      IF (M.GT.0) GO TO 13
      D=D1
      PX(I)=(B-A-SB1+SA1)/D
      GO TO 18
13    IF (M.GT.1) GO TO 14
      D=0.5*D1
      PX(I)=((B**2)/2.0-(A**2)/2.0-B*SB1+A*SA1-CB1+CA1)/D
      GO TO 18
14    IF (M.GT.2) GO TO 15
      D=0.2826727*D1
      PX(I)=((B**3)/3.0-(A**3)/3.0-(B**2)*SB1+(A**2)*SA1
     1  +2.0*SB2-2.0*SA2-2.0*B*CB1+2.0*A*CA1)/D
      GO TO 18
15    IF (M.GT.3) GO TO 16
      D=0.1740091*D1
      PX(I)=((B**4)/4.0-(A**4)/4.0-(B**3)*SB1+(A**3)*SA1
     1  +6.0*B*SB2-6.0*A*SA2-3.0*(B**2)*CB1+3.0*(A**2)*CA1
     2  +6.0*CB2-6.0*CA2)/D
      GO TO 18
16    IF (M.GT.4) GO TO 17
      D=0.1140776*D1
      PX(I)=((B**5)/5.0-(A**5)/5.0-(B**4)*SB1+(A**4)*SA1
     1  +12.0*(B**2)*SB2-12.0*(A**2)*SA2-24.0*SB3+24.0*SA3
     2  -4.0*(B**3)*CB1+4.0*(A**3)*CA1+24.0*B*CB2-24.0*A*
     3  CA2)/D
      GO TO 18
17    D=0.0785125*D1
      PX(I)=((B**6)/6.0-(A**6)/6.0-(B**5)*SB1+(A**5)*SA1
     1  +20.0*(B**3)*SB2-20.0*(A**3)*SA2-120.0*B*SB3+120.0*
     1  A*SA3
     2  -5.0*(B**4)*CB1+5.0*(A**4)*CA1+60.0*(B**2)*CB2
     3  -60.0*(A**2)*CA2-120.0*CB3+120.0*CA3)/D
```

```
   18       PY(I)=-01*PX(I)
   19       CONTINUE
            WRITE (6,301) (LOCT(I),PX(I),PY(I), I=1,NML)
C
C  DETERMINATION OF PXS(I) AND PYS(I)
            DO 23 I=1,NML
            DO 22 J=1,NML
            RXB=XB(I)-XB(J)
            RYB=YB(I)-YB(J)
            IF (I.NE.J) GO TO 21
            B1(I,J)=0.0
            B2(I,J)=0.0
            B3(I,J)=0.0
            GO TO 22
   21       PN=ANX(I)*RXB+ANY(I)*RYB
            PG=(RXB**2+RYB**2)**2
            B1(I,J)=-2.0*S(I)*PN*(RXB**2)/(PI*PG)
            B2(I,J)=-2.0*S(I)*PN*RXB*RYB/(PI*PG)
            B3(I,J)=-2.0*S(I)*PN*(RYB**2)/(PI*PG)
   22       CONTINUE
   23       CONTINUE
            DO 24 I=1,NML
            PXS(I)=PX(I)
            PYS(I)=PY(I)
   24       CONTINUE
            NCICLE=1
            GO TO 27
   25       IF (NCICLE.GT.40) GO TO 33
            NCICLE=NCICLE+1
            DO 26 I=1,NML
            PXS(I)=PXSN(I)
            PYS(I)=PYSN(I)
   26       CONTINUE
   27       DO 28 I=1,NML
            SUMX(I)=0.0
            SUMY(I)=0.0
   28       CONTINUE
            DO 30 I=1,NML
            DO 29 J=1,NML
            SX=PXS(J)*B1(I,J)+PYS(J)*B2(I,J)
            SY=PXS(J)*B2(I,J)+PYS(J)*B3(I,J)
            SUMX(I)=SUMX(I)+SX
            SUMY(I)=SUMY(I)+SY
   29       CONTINUE
   30       CONTINUE
            DO 31 I=1,NML
            PXSN(I)=AL*PX(I)+(1.0-AL)*PXS(I)-AL*SUMX(I)
            PYSN(I)=AL*PY(I)+(1.0-AL)*PYS(I)-AL*SUMY(I)
   31       CONTINUE
            DO 32 I=1,NML
```

```
      EPXS=PC*ABS(PXS(I))
      EPYS=PC*ABS(PYS(I))
      DPXS=ABS(PXSN(I)-PXS(I))
      DPYS=ABS(PYSN(I)-PYS(I))
      IF (DPXS.GT.EPXS) GO TO 25
      IF (DPYS.GT.EPYS) GO TO 25
   32 CONTINUE
   33 WRITE (6,401) NCICLE, (LOCT(I),PXSN(I),PYSN(I),
     1 I=1,NML)
C
C DETERMINATION OF SGMAXX(I),SGMAYY(I),SGMAXY(I)
      N=1
      L=1
      NFP=NFPI
   34 DO 35 I=L,NFP
      SGMAXX(I)=0.0
      SGMAYY(I)=0.0
      SGMAXY(I)=0.0
   35 CONTINUE
      DO 37 I=L,NFP
      DO 36 J=1,NML
      RXF=XF(I)-XB(J)
      RYF=YF(I)-YB(J)
      SN1=-2.0/(PI*((RXF**2+RYF**2)**2))
      SN2=PXSN(J)*RXF+PYSN(J)*RYF
      SNXX=SN1*SN2*(RXF**2)
      SNYY=SN1*SN2*(RYF**2)
      SNXY=SN1*SN2*RXF*RYF
      SGMAXX(I)=SGMAXX(I)+SNXX
      SGMAYY(I)=SGMAYY(I)+SNYY
      SGMAXY(I)=SGMAXY(I)+SNXY
   36 CONTINUE
   37 CONTINUE
      WRITE (6,100)
      WRITE (6,501) (LOCT(I),XF(I),YF(I), I=L,NFP)
      WRITE (6,601) (LOCT(I),SGMAXX(I),SGMAYY(I),
     1 SGMAXY(I), I=L,NFP)
C
C DETERMINATION OF SGMA1(I) AND SGMA2(I)
      DO 41 I=L,NFP
      IF (ABS(SGMAXX(I)-SGMAYY(I)).LT.0.00001) GO TO 38
      ALPHAA(I)=0.5*ATAN(2.0*SGMAXY(I)/
     1 (SGMAXX(I)-SGMAYY(I)))
      GO TO 39
   38 ALPHAA(I)=PI/4.0
   39 SGMAA(I)=SGMAXX(I)*(COS(ALPHAA(I))**2)+SGMAYY(I)*
     1 (SIN(ALPHAA(I))**2)+2.0*SGMAXY(I)*SIN(ALPHAA(I))*
     2 COS(ALPHAA(I))
      ALPHAB(I)=ALPHAA(I)+PI/2.0
      SGMAB(I)=SGMAXX(I)*(COS(ALPHAB(I))**2)+SGMAYY(I)*
```

```
     1    (SIN(ALPHAB(I))**2)+2.0*SGMAXY(I)*SIN(ALPHAB(I))*
     2    COS(ALPHAB(I))
          IF(SGMAA(I).GT.SGMAB(I)) GO TO 40
          SGMA1(I)=SGMAB(I)
          SGMA2(I)=SGMAA(I)
          ALPHA1(I)=ALPHAB(I)*(180.0/PI)
          ALPHA2(I)=ALPHAA(I)*(180.0/PI)
          GO TO 41
  40      SGMA1(I)=SGMAA(I)
          SGMA2(I)=SGMAB(I)
          ALPHA1(I)=ALPHAA(I)*(180.0/PI)
          ALPHA2(I)=ALPHAB(I)*(180.0/PI)
  41      CONTINUE
          WRITE (6,701) (LOCT(I),SGMA1(I),SGMA2(I),ALPHA1(I),
     1    ALPHA2(I), I=L,NFP)
C
C DETERMINATION OF F(I) AND PSI(I)
          IF (N.GT.1) GO TO 47
  46      READ (5,DATA2)
          WRITE (6,DATA2)
  47      DO 42 I=L,NFP
          F(I)=(MU*(SGMA1(I)+SGMA2(I))/2.0)+(SQRT(1.0+MU**2)
     1    /2.0)*(SGMA1(I)-SGMA2(I))
          PSI1(I)=ALPHA1(I)+45.0-((ATAN(MU))/2.0)*(180.0/PI)
          PSI2(I)=ALPHA1(I)-45.0+((ATAN(MU))/2.0)*(180.0/PI)
  42      CONTINUE
          WRITE (6,801) (LOCT(I),F(I),PSI1(I),PSI2(I),
     1    I=L,NFP)
          FMAX=F(L)
          X=XF(L)
          Y=YF(L)
          II=L+1
          DO 43 I=II,NFP
          IF (F(I).LE.FMAX) GO TO 43
          FMAX=F(I)
          X=XF(I)
          Y=YF(I)
  43      CONTINUE
          WRITE (6,901) FMAX
C
C FURTHER SUBDIVISION OF FIELD
          N=N+1
          IF (NFP.EQ.NFPI) GO TO 50
          N=1
          L=1
          NFP=NFPI
          GO TO 48
  50      L=NFP+1
          NFP=NFP+22
          II=L+7
```

```
      JJ=NFP-4
      DO 51 I=II,JJ,5
51    XF(I)=X-2.0*DIV
      II=L+3
      JJ=NFP-3
      DO 52 I=II,JJ,5
52    XF(I)=X-DIV
      XF(L)=X
      II=L+4
      JJ=NFP-2
      DO 53 I=II,JJ,5
53    XF(I)=X
      XF(L+1)=X+DIV
      II=L+5
      JJ=NFP-1
      DO 54 I=II,JJ,5
54    XF(I)=X+DIV
      XF(L+2)=X+2.0*DIV
      II=L+6
      DO 55 I=II,NFP,5
55    XF(I)=X+2.0*DIV
      JJ=L+2
      DO 56 I=L,JJ
56    YF(I)=Y+2.0*DIV
      II=L+3
      JJ=L+6
      DO 57 I=II,JJ
57    YF(I)=Y+DIV
      II=L+7
      JJ=L+11
      DO 58 I=II,JJ
58    YF(I)=Y
      II=L+12
      JJ=L+16
      DO 59 I=II,JJ
59    YF(I)=Y-DIV
      II=L+17
      DO 60 I=II,NFP
60    YF(I)=Y-2.0*DIV
      GO TO 34
      END
```

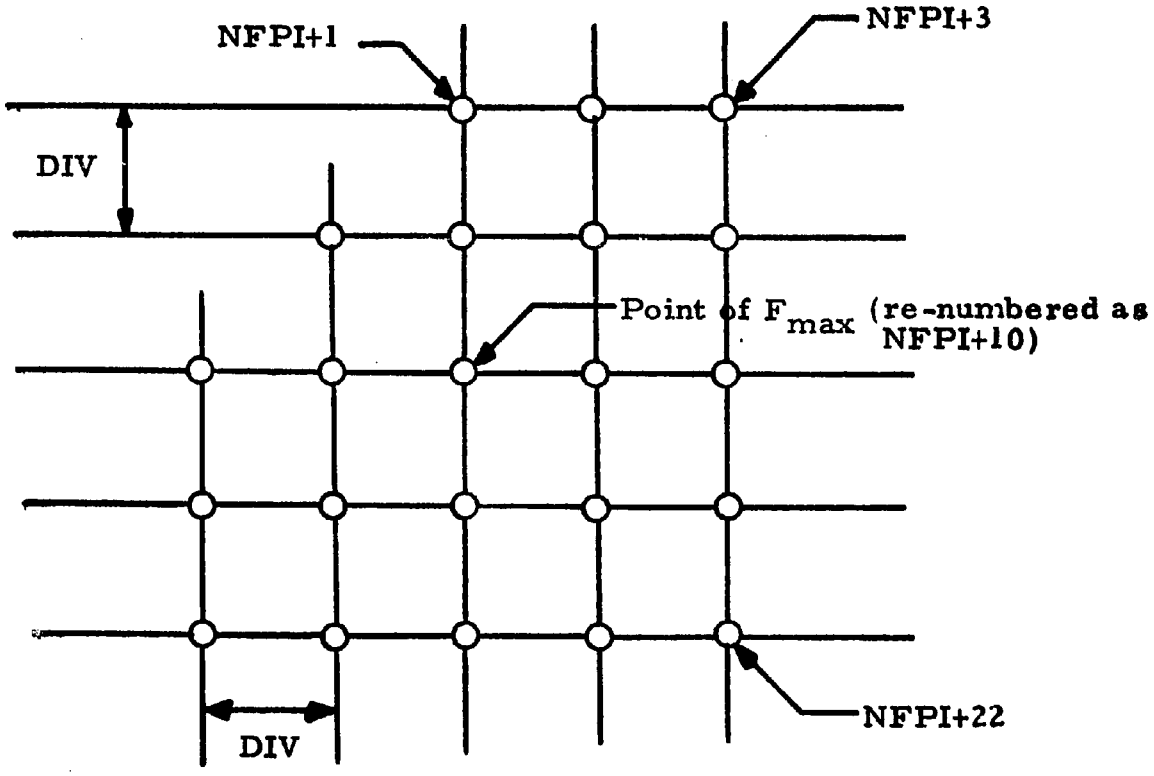


FIGURE B-1 REFINEMENT OF FIELD IN VICINITY OF F_{max}

APPENDIX C

POLYNOMIAL FITS OF $\bar{\sigma} = \bar{\sigma}(\bar{\sigma}_m)$ AND $\bar{\tau} = \bar{\tau}(\bar{\sigma}_m)$ FOR BLAIR DOLOMITE AND QUARTZITE

The coefficients α_i , β_i of equations (2.16) were obtained in the following way. Normals were drawn to the Mohr envelope of the material at a number of points spanning the range of interest. The intercepts of these normals with the $\bar{\sigma}$ axis determine the values of $\bar{\sigma}_m$ and the corresponding points on the Mohr envelope determine the corresponding values of $\bar{\sigma}$, $\bar{\tau}$. Data points obtained in this way are shown in Table C-1 for Blair dolomite and Table C-2 for quartzite. Polynomial curves were then fit to these data points using the computer program developed in reference [38] . Polynomials of orders 1 through 9 were fit to the data of Tables C-1 and C-2 and the best of these fits was chosen in each case. The coefficients found are given in Table C-3.

TABLE C-1

Points Obtained from Mohr Envelope of Blair Dolomite

$\bar{\sigma}_m$ (kb)	$\bar{\tau}$ (kb)	$\bar{\sigma}$ (kb)
- .7	.25	.4
- .9	.5	.3
- 1.4	1.0	0.0
- 2.0	1.3	- .25
- 2.5	1.6	- .45
- 3.6	2.4	- 1.2
- 4.4	3.1	- 1.95
- 5.9	4.2	- 3.5
- 6.45	4.75	- 4.65
- 7.1	5.1	- 5.7
- 8.2	5.5	- 7.4
- 9.1	5.6	- 9.0
-10.0	5.6	-10.0
-11.0	5.6	-11.0

TABLE C-2

Points Obtained from Mohr Envelope of Quartzite

$\bar{\sigma}_m$(kb)	$\bar{\tau}$ (kb)	$\bar{\sigma}$ (kb)
- .2	.2	.3
- 1.2	.6	.1
- 3.4	1.5	- .4
- 4.7	2.2	- .8
- 6.2	3.3	- 1.5
- 9.0	4.6	- 2.4
-11.0	6.0	- 3.6
-11.65	7.2	- 4.6
-12.65	8.1	- 5.55
-14.0	8.75	- 6.4
-14.8	9.55	- 7.35
-15.8	10.4	- 8.5
-16.95	11.4	-10.1
-17.5	12.3	-12.0

TABLE C-3

Coefficients of Least Squares Polynomial Fits
for Blair Dolomite and Quartzite

	Blair dolomite	Quartzite
α_0	- .90932523	.14589997
α_1	-2.2527893	-.39293411
α_2	- .98623052	-.11661122
α_3	- .27366620	-.07536858
α_4	- .03557571	-.01643163
α_5	- .00211718	-.00168279
α_6	- .00004702	-.00008117
α_7	.00000000	-.00000149
S	.058635	.257773
β_0	.64800776	.37275022
β_1	.25671860	.44518983
β_2	- .22792865	.32929945
β_3	- .10632980	.14898031
β_4	- .02453351	.02914393
β_5	- .00222438	.00282896
β_6	- .00006876	.00013247
β_7	.00000000	.00000239
S	.113464	.205440

APPENDIX D

"FRACTURE" COMPUTER PROGRAM-
NONLINEAR FRACTURE ENVELOPE

The computer program of Appendix B can be modified so as to handle nonlinear fracture envelopes. These modifications are:

1. Replace the section C ISOTROPIC CASE - LINEAR CRITERION with C ISOTROPIC CASE - NONLINEAR CRITERION found in this appendix.
2. Replace the section C DETERMINATION OF F(I) AND PSI(I) with C DETERMINATION OF K(I) AND PSI(I) found in this appendix.
3. Input Data: Replace MU with MUI (initial choice of μ : $\mu^{(0)}$), and add:

   CI - initial choice of C : $C^{(0)}$ (in kb)

   T0,$\cdots$,T7 - coefficients α_i, equation (2.16)

   S0,$\cdots$,S7 - coefficients β_i, equation (2.16)

   SIGMAX - value of $\bar{\sigma}$ at which Mohr envelope is essentially equal to asymptote (in kb)

   TAUMAX - maximum value of $\bar{\tau}$ for Mohr envelope (in kb)

   SGMAH - hydrostatic stress (in kb)
4. Output Data: The same output is obtained as in the linear case except that the fracture function is now K rather than F and the value at the point of fracture initiation is KMIN rather than FMAX. Also, for each iteration, the following is obtained:

(SGMAM(I), MU(I), C(I), I = 1, NFP)

- the mean stress and slope and $\overline{\tau}$ - intercept of a linear envelope tangent to the real Mohr envelope at a point defined by the mean stress at each point.

```
C ISOTROPIC CASE - NONLINEAR CRITERION
      REAL MUF
      REAL MUI
      REAL MU(164)
      REAL K(164,10)
      REAL KMIN
      DIMENSION S(96),XB(96),YB(96),ANX(96),ANY(96),
     1  PX(96),PY(96),B1(96,96),B2(96,96),B3(96,96),
     2  PXS(96),PYS(96),PXSN(96),PYSN(96),SUMX(96),
     3  SUMY(96),XF(164),YF(164),SGMAXX(164),SGMAYY(164),
     4  SGMAXY(164),SGMAA(164),SGMAB(164),SGMA1(164),
     5  SGMA2(164),ALPHAA(164),ALPHAB(164),ALPHA1(164),
     6  ALPHA2(164),PSI1(164),PSI2(164),LOCT(164),C(164),
     7  SGMAM(164),SIG(164),TAU(164)
 100  FORMAT ('1')
 201  FORMAT ('0LOCT',19X,'XB',35X,'YB'/'0'/
     1  (I4,8X,E20.8,16X,E20.8))
 301  FORMAT ('0LOCT',19X,'PX',35X,'PY'/'0'/
     1  (I4,8X,E20.8,16X,E20.8))
 401  FORMAT ('0CICLE =',I4/'0'/'LOCT',18X,'PXS',34X,
     1  'PYS'/'0'/(I4,8X,E20.8,16X,E20.8))
 501  FORMAT ('0LOCT',19X,'XF',35X,'YF'/'0'/
     1  (I4,8X,E20.8,16X,E20.8))
 601  FORMAT ('0LOCT',17X,'SGMAXX',30X,'SGMAYY',30X,
     1  'SGMAXY'/'0'/(I4,8X,E20.8,16X,E20.8,16X,E20.8))
 701  FORMAT ('0LOCT',17X,'SGMA1',21X,'SGMA2',20X,
     1  'ALPHA1',20X,'ALPHA2'/'0'/
     2  (I4,8X,E20.8,6X,E20.8,6X,E20.8,6X,E20.8))
 800  FORMAT ('0ITERATION  =',I3)
 801  FORMAT ('0LOCT',17X,'SGMAM',22X,'MU',25X,'C'/'0'/
     1  (I4,8X,E20.8,6X,E20.8,6X,E20.8))
 802  FORMAT ('0LOCT',19X,'K',34X,'PSI1',32X,'PSI2'/'0'/
     1  (I4,8X,E20.8,16X,E20.8,16X,E20.8))
 901  FORMAT ('0CICLES =',I4,10X,'KMIN  =',E20.8)
      NAMELIST/DATA1/NNL,NDB,NSA,S,PC,AL,NFPI,XF,YF,DIV,
     1  THETA,MUF,M
      NAMELIST/DATA2/MUI,CI,T0,T1,T2,T3,T4,T5,T6,T7,S0,
     1  S1,S2,S3,S4,S5,S6,S7,
     2  SIGMAX,TAUMAX,SGMAM
      READ (5,DATA1)
      WRITE (6,DATA1)
      DO 2 I=1,164
    2 LOCT(I)=I
C
C DETERMINATION OF K(I) AND PSI(I)
      IF (N.GT.1) GO TO 47
   48 READ (5,DATA2)
      WRITE (6,DATA2)
   47 J=1
      DO 42 I=L,NPP
```

```
      MU(I)=MUI
      C(I)=CI
      K(I,J)=(2.0*(C(I)-MU(I)*SGMAH))/(MU(I)*(SGMA1(I)+
     1 SGMA2(I))+(SQRT(1.0+MU(I)**2))*(SGMA1(I)-SGMA2(I)))
      PSI1(I)=ALPHA1(I)+45.0-((ATAN(MU(I)))/2.0)*
     1 (180.0/PI)
      PSI2(I)=ALPHA1(I)-45.0+((ATAN(MU(I)))/2.0)*
     1 (180.0/PI)
42    CONTINUE
      WRITE (6,800) J
      WRITE (6,802) (LOCT(I),K(I,J),PSI1(I),PSI2(I),
     1 I=L,NFP)
43    J=J+1
      JP=J-1
      DO 44 I=L,NFP
      SGMAM(I)=(K(I,JP)*(SGMA1(I)+SGMA2(I))/2.0)+SGMAH
      IF (SGMAM(I).LT.SIGMAX) GO TO 61
      TAU(I)=T0+T1*(SGMAM(I))+T2*(SGMAM(I)**2)+T3*
     1 (SGMAM(I)**3)+T4*(SGMAM(I)**4)
     2 +T5*(SGMAM(I)**5)+T6*(SGMAM(I)**6)+
     3 T7*(SGMAM(I)**7)
      SIG(I)=S0+S1*(SGMAM(I))+S2*(SGMAM(I)**2)+S3*
     1 (SGMAM(I)**3)+S4*(SGMAM(I)**4)
     2 +S5*(SGMAM(I)**5)+S6*(SGMAM(I)**6)+
     3 S7*(SGMAM(I)**7)
      MU(I)=(SIG(I)-SGMAM(I))/TAU(I)
      C(I)=TAU(I)+SIG(I)*MU(I)
      GO TO 62
61    MU(I)=0.0
      C(I)=TAUMAX
62    K(I,J)=(2.0*(C(I)-MU(I)*SGMAH))/(MU(I)*
     1 (SGMA1(I)+SGMA2(I))+(SQRT(1.0+MU(I)**2))*
     2 (SGMA1(I)-SGMA2(I)))
      PSI1(I)=ALPHA1(I)+45.0-((ATAN(MU(I)))/2.0)*(180.0/PI)
      PSI2(I)=ALPHA1(I)-45.0+((ATAN(MU(I)))/2.0)*(180.0/PI)
44    CONTINUE
      WRITE (6,800) J
      WRITE (6,801) (LOCT(I),SGMAM(I),MU(I),C(I),  I=L,NFP)
      WRITE (6,802) (LOCT(I),K(I,J),PSI1(I),PSI2(I),  I=L,NFP)
      IF (J.GT.9) GO TO 46
      DO 45 I=L,NFP
      EK=0.010*ABS(K(I,JP))
      DK=ABS(K(I,J)-K(I,JP))
      IF (DK.GT.EK) GO TO 43
45    CONTINUE
46    CONTINUE
      KMIN=K(L,J)
      X=XF(L)
      Y=YF(L)
      LT=L+1
```

```
      DO 49 I=II,NPP
      IF (K(I,J).LT.0.0) GO TO 49
      IF (K(I,J).GE.KMIN) GO TO 49
      KMIN=K(I,J)
      X=XF(I)
      Y=YF(I)
49    CONTINUE
      WRITE (6,901) J,KMIN
```

APPENDIX E

FINITE ELEMENT SOLUTION TO MIXED BOUNDARY-VALUE PROBLEM

A finite element program, developed by Weaver [39] has been used to solve for the stress field in the mixed boundary-value problem of section III.3. In figures E-1 and E-2, the problem geometry is shown with elements and nodes labeled. (Due to symmetry, one-half the model is considered.) A vertical displacement of -.001" was specified for all nodes along boundary BE; the normal traction on boundary DB was specified as zero; and all shear tractions were specified as zero. The material constants, determined in section III.2, are $E = 4.2 \times 10^5$ psi and $\nu = 0.24$.

The values of the $\bar{\sigma}_{\tilde{y}}$ stress component determined by the finite element program are tabulated in Table E-1 for elements along BE $(2, 4, 6, 8, \cdots, 32)$. These values are then integrated over the element length and nondimensionalized (see Table E-1) to yield the equivalent line load applied to each surface element. The traction distribution is plotted in figure E-3. (The shape of this distribution was in fact verified photoelastically.)

The loading found in this way is then used as input for the integral equation method in the "fracture" program.

The two solutions (finite element and integral method) are compared at the points shown in figure E-4. The results are tabulated in Table E-2.

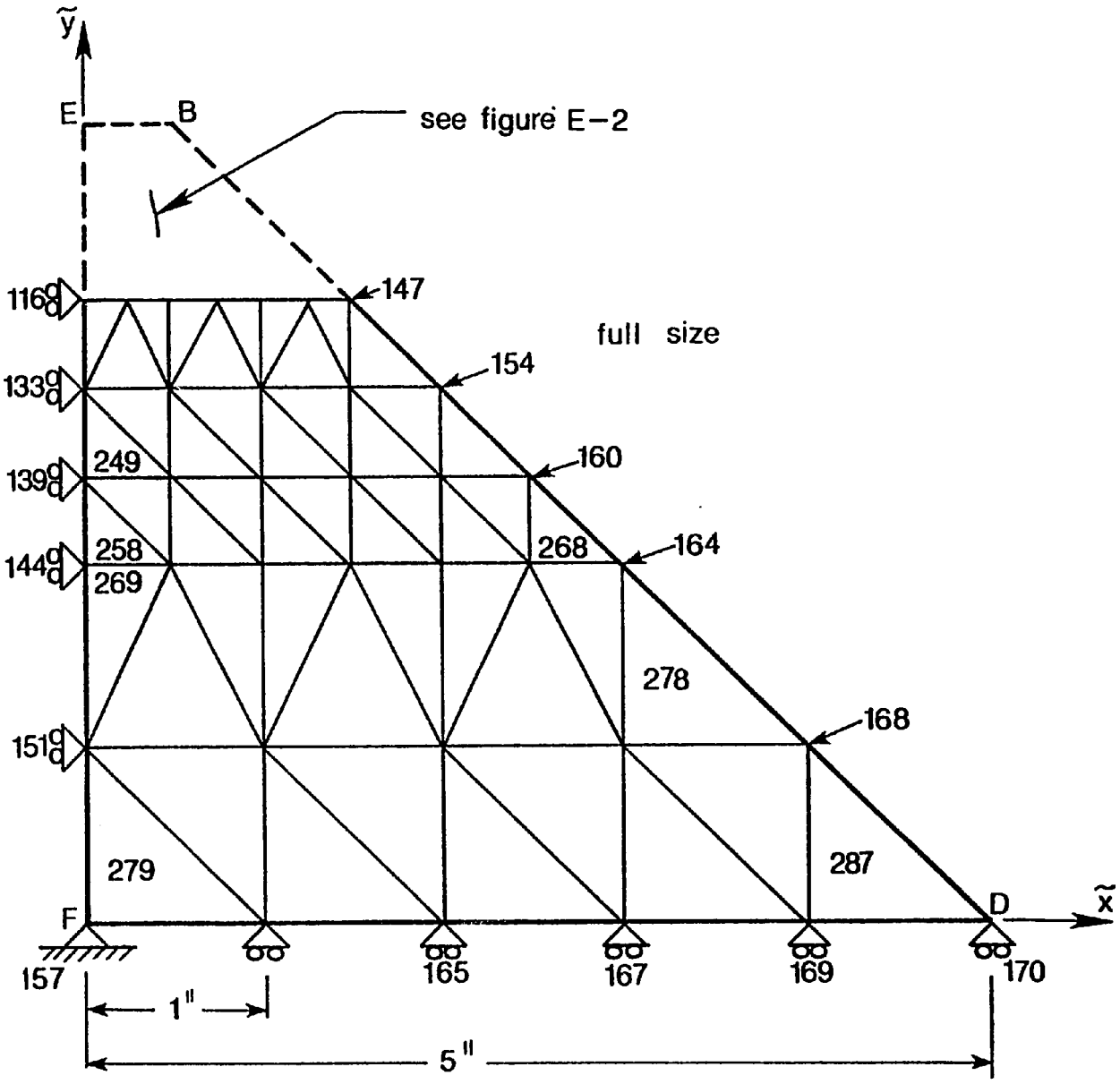


FIGURE E-1 NODE AND ELEMENT LABELS FOR FINITE ELEMENT ANALYSIS OF MIXED BOUNDARY-VALUE PROBLEM

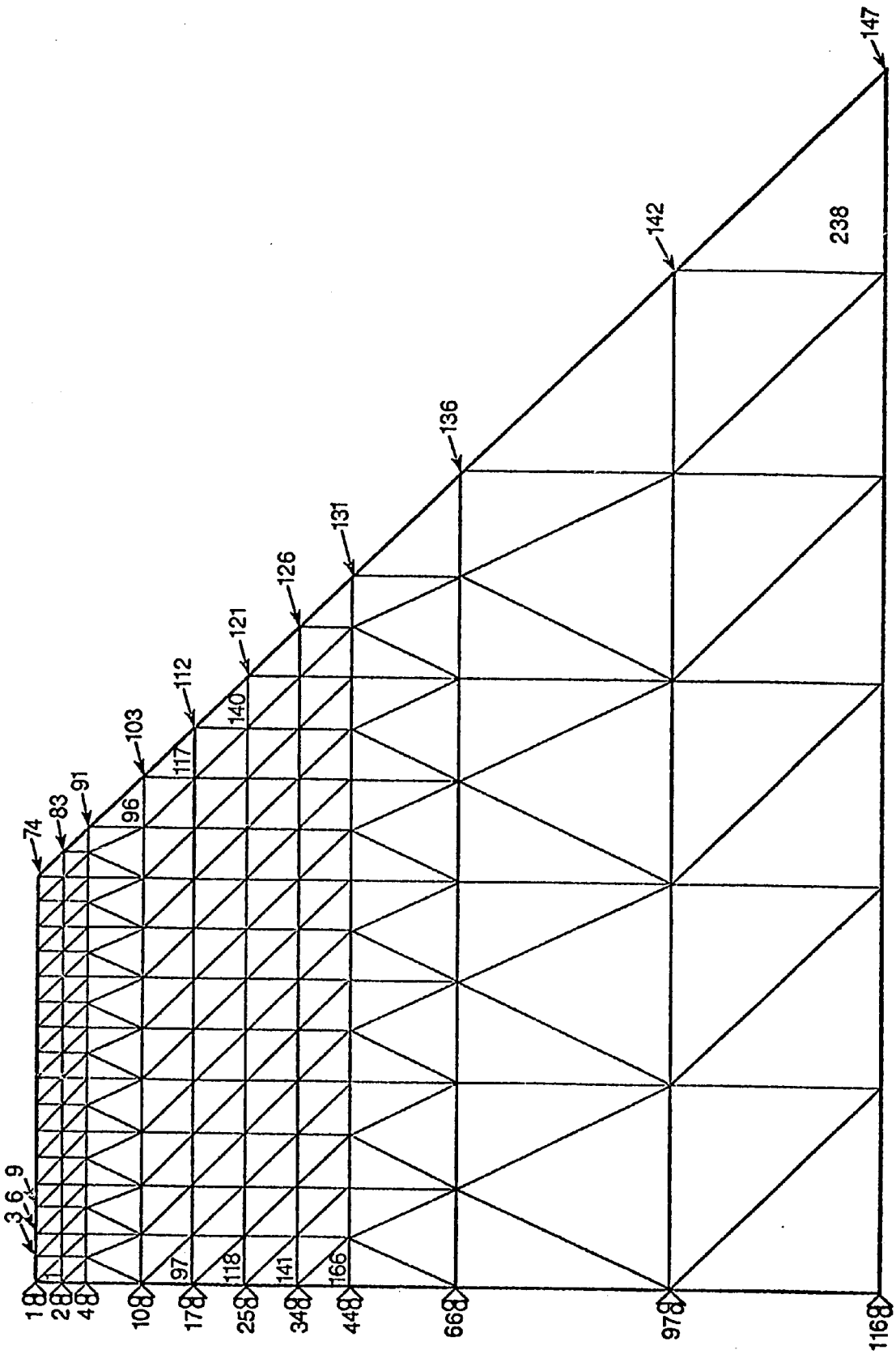


FIGURE E-2 ENLARGEMENT OF REGION FROM FIGURE E-1

TABLE E-1

Traction Components on Truncated Edge
Due to Uniform Displacement Condition

Element	$\bar{\sigma}_{\tilde{y}}$ (psi)	P_n
32	-669.1	.08009
30	-448.8	.05372
28	-347.8	.04162
26	-290.9	.03487
24	-259.6	.03112
22	-236.0	.02828
20	-222.3	.02659
18	-209.7	.02514
16	-202.3	.02422
14	-194.7	.02330
12	-190.3	.02276
10	-185.6	.02223
8	-183.0	.02192
6	-180.1	.02154
4	-178.8	.02138
2	-177.2	.02123

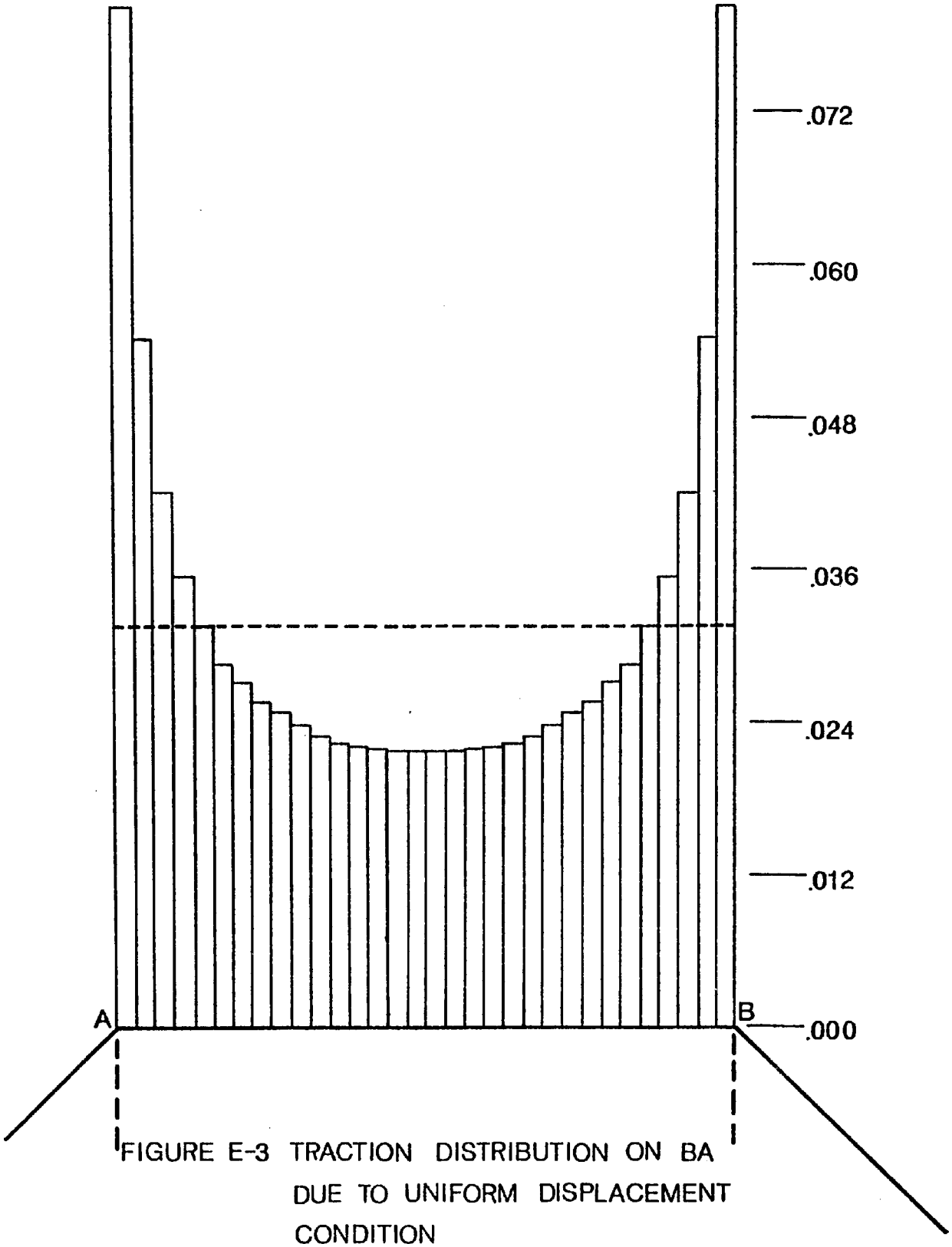


FIGURE E-3 TRACTION DISTRIBUTION ON BA DUE TO UNIFORM DISPLACEMENT CONDITION

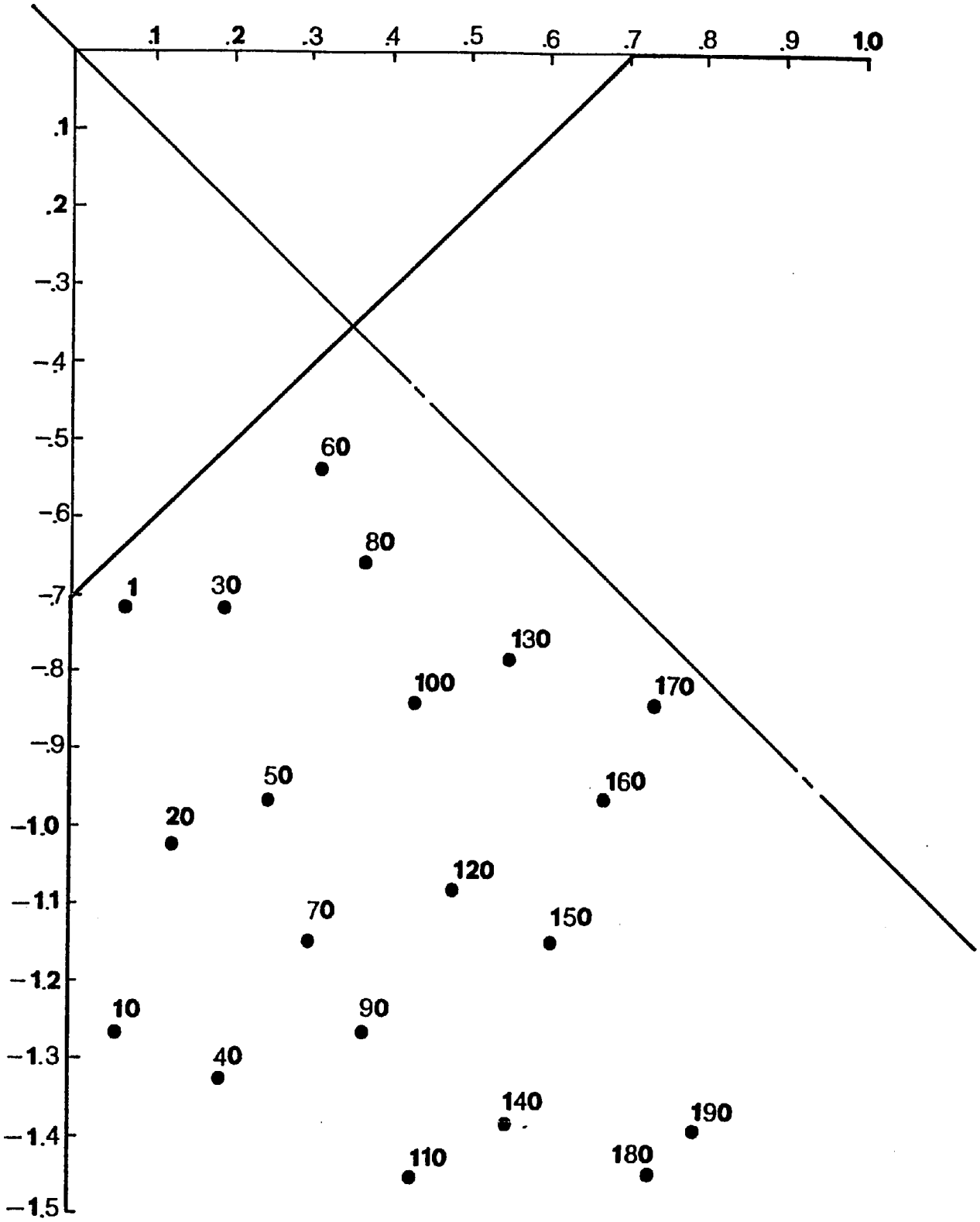


FIGURE E-4 LOCATION OF POINTS FOR COMPARISON OF FINITE ELEMENT AND INTEGRAL METHOD SOLUTIONS

It should be noted that the problems solved by these two methods are not quite the same. The finite element method is applied to a finite geometry (figure E-1) whereas the integral method, as it appears in the "fracture" program, is applied to the infinite truncated quarter plane (figure 7). Thus, Table E-2 is useful in assessing the effect of the boundary DF on the stress field. This effect appears to be restricted to points 40, 180 and 190 where the differences are greater than 10%. Thus in the region of interest for the fracture analysis, the effect of the boundary DF is quite small, being generally less than 5%.

Of the two methods, the integral method is felt to be more accurate. The accuracy of this method is examined in section II.2 where it is found to be within 1% of an analytical solution at points away from the boundary. Since the field, rather than the boundary, is subdivided in the finite element method, the errors are throughout the field. Furthermore, the integral method yields stress at a point whereas the finite element method yields "averaged" stresses for each element. Thus the accuracy of the finite element method is also dependent on the element size.

TABLE E-2

Comparison of Finite Element Solution
and Integral Equation Solution

Point (integral method)	σ_1	σ_2	Element (finite elements)	σ_1	σ_2	σ_2 %diff
1	-.43	-1.68	63	-.62	-1.58	- 6.0
10	.00	- .42	213	.02	- .44	4.8
20	-.01	- .63	161	-.04	- .65	3.2
30	-.32	-1.04	108	-.36	- .98	- 5.8
40	.00	- .46	224	-.01	- .51	10.9
50	-.05	- .74	182	-.05	- .74	0.0
60	-.46	- .74	76	-.38	- .73	- 1.4
70	-.02	- .60	221	-.00	- .62	3.3
80	-.32	- .78	124	-.24	- .75	- 3.8
90	-.01	- .53	222	-.02	- .51	- 3.8
100	-.14	- .75	199	-.13	- .72	- 4.0
110	-.01	- .46	233	.02	- .43	- 6.5
120	-.05	- .63	219	-.06	- .63	0.0
130	-.17	- .72	196	-.18	- .70	- 2.8
140	-.01	- .50	232	.00	- .52	4.0
150	-.04	- .59	219	-.05	- .63	6.8
160	-.07	- .64	217	-.09	- .63	- 1.6
170	-.10	- .66	215	-.11	- .64	- 3.0
180	-.01	- .47	241	.02	- .41	-12.8
190	-.02	- .48	241	.02	- .41	-14.6

REFERENCES

1. Galileo, G., "Dialogues Concerning Two New Sciences," 1638, (trans. by Crew, H., and De Salvo, A.), Macmillan, New York, 1914.

2. Coulomb, C.A., In "Memoirs de mathematique et de physique," (Academie Royal des Sciences par divers savans), Vol. 7, pp. 343-382, Paris, 1776.

3. Navier, L.M.H., "Résumé des lecons données a l'ecole des ponts et chaussées sur l'application de la mecanique a l'etablissment des constructions et des machines," 1833.

4. Mohr, O., In Zeitschrift des Vereines Deutscher Ingenieure 44, pp. 1524-1530, 1900.

5. Kármán, Th. v., In Zeitschrift des Vereines Deutscher Ingenieure 55, pp. 1749-1757, 1911.

6. Böker, R., in Mitteilungen Forschungsarbiet auf dem Gebiete Ingenieurwesens, pp. 175-176, 1915.

7. Griffith, A.A., "The Phenomena of Rupture and Flow in Solids," Phil. Trans., Vol. 221, 1921, pp. 163-198.

8. Griffith, A.A., "Theory of Rupture," Proc. 1st Int'l. Cong. Appl. Mech., ed. by Bienzeno and Burgess, J. Waltman Jr. Press, Delft, 1925, pp. 53-64.

9. Inglis, C.E., "Stresses in a Plate due to the Presence of Cracks and Sharp Corners," Inst. Naval Arch. (London) Trans., 55, pp. 219-230, 1913.

10. Murrell, S.A.F., "The Strength of Coal Under Triaxial Compression," in Mechanical Properties of Non-metallic Brittle Solids, Interscience, New York, pp. 123-146, 1958.

11. McClintock, F.A., and Walsh, J.B., "Friction on Griffith Cracks in Rocks under Pressure," Proc. of the Fourth U.S. Congress on Applied Mechanics, ASME, pp. 1015-1021, New York, 1963.

12. Brace, W.F., "An Extension of the Griffith Theory of Fracture to Rocks," Journal of Geophysical Research, Vol. 65, No. 10, Oct., 1960, pp. 3477-3480.

13. Robertson, E.C., "Experimental Study of the Strength of Rocks," Bull. Geol. Soc. Am., 66, pp. 1275-1314, 1955.

14. Cook, N.G.W., Thesis, Univ. of Witwaterstrand, 1962.

15. Fairhurst, C., and Cook, N.G.W., In Proc. of the 1st Congress of International Soc. on Rock Mechanics, Lisbon, Vol. 1, pp. 687-692, 1966.

16. Brace, W.F., "Brittle Fracture of Rocks," State of Stress in the Earth's Crust, (ed. Judd, W.), Elsevier, New York, 1964.

17. Brace, W.F., and Bombolakis, E.G., "A Note on Brittle Crack Growth in Compression," Journal of Geophysical Research, Vol. 68, No. 12, June, 1963, pp. 3709-3713.

18. Hoek, E., and Bieniawski, Z.T., "Brittle Fracture Propagation in Rock Under Compression," Journal of Fracture Mechanics, Vol. 1, No. 3, September, 1965, pp. 137-155.

19. Bieniawski, Z.T., "Mechanism of Brittle Fracture in Rock," Int'l.J. Rock Mech. Min. Sci., Vol. 4, pp. 395-406, Pergamon Press, 1967.

20. Brace, W.F., Paulding, B.W., Jr. and Scholz, C., "Dilatancy in the Fracture of Crystalline Rocks," Journal of Geophysical Research, Vol. 71, 1966, pp. 3939-3953.

21. Cook, N.G.W., "An Experiment Proving that Dilatancy is a Pervasive Volumetric Property of Brittle Rock Loaded to Failure," Rock Mechanics, Vol. 2, 1970, pp. 181-188.

22. Brace, W.F., Silver, E., Hadley, K., and Goetze, C., "Cracks and Pores: A Closer Look," Science, 13 Oct. 1972, pp. 162-164.

23. Paul, B., "Macroscopic Criteria for Plastic Flow and Brittle Fracture," Chapter four of Fracture, Vol. II, ed. by Liebowitz, Academic Press, 1968.

24. Obert, L., "Brittle Fracture of Rock," chapter three of Fracture, Vol. VII, ed. by Liebowitz, Academic Press, 1972.

25. Massonnet, C., "Numerical Use of Integral Procedures," chapter 10 of Stress Analysis - Recent Developments in Numerical and Experimental Methods, ed. by Zienkiewicz, O.C., and Holister, G.S., J. Wiley and Sons, 1965.

26. Benjumea, R., and Sikarskie, D. L., "On the Solution of Plane, Orthotropic Elasticity Problems by an Integral Method," Journal of Applied Mechanics, Vol. 39, No. 3, Trans. ASME, Vol. 94, Series E, Sept. 1972, pp. 801-808.

27. Sikarskie, D. L. and Cheatham, J. B., "Penetration Problems in Rock Mechanics," Rock Mechanics Symposium, ed. by Sikarskie, D. L., ASME AMD-Vol. 3, November, 1973, pp. 41-72.

28. Timoshenko, S., and Goodier, J.N., Theory of Elasticity, 3rd edition, McGraw-Hill, Inc., 1970.

29. Hildebrand, F.B., Introduction to Numerical Analysis, McGraw-Hill, Inc., 1956.

30. Cheatham, J. B., "Rock-Bit Tooth Friction Analysis," Society of Petroleum Enginers of ASME, Monograph, Dec. 1963.

31. Sikarskie, D. L., "Experiments on Wedge Indentation in Rocks," Ingersoll-Rand TN-262, Ingersoll-Rand Research Center, Princeton, N.J., May, 1966.

32. Gnirk, P.F., and Cheatham, J.B., "An Experimental Study of Single Bit-Tooth Penetration into Dry Rock at Confining Pressures of 0 to 5000 psi," Society of Petroleum Engineers Journal, AIME Trans., Vol. 234, 1965, pp. 117-130.

33. Stimpson, B., "Modelling Materials for Engineering Rock Mechanics," Int'l. J. Rock Mech. Mining Sci., Vol. 7, 1970, pp. 77-121.

34. Ishii, F., Ida, R., Yugeta, H., Kishimoto, S., and Tendou, H., "On the Strength Characteristics of Bedded Rock," Proceedings of the First Congress of the Intl'. Society of Rock Mechanics, Lisbon, Vol. 1, pp. 525-529 (1966).

35. Roark, R.J., and Hartenburg, R.S., "Predicting the Strength of Structures from Tests of Plaster Models," Bulletin of the Univ. of Wisconsin Engineering Experiment Station Series, No. 81, 1935.

36. Barron, K., and Larocque, G.E., "Development of a Model for a Mine Structure," Proc. Rock Mech. Symp., McGill Univ., Sept., 1962, pp. 145-185.

37. Fairhurst, C., "On the Validity of the 'Brazilian' Test for Brittle Materials," Int'l. J. Rock Mech. and Mining Sci., Vol. 1, pp. 535-546, Pergamon Press, 1964.

38. Carnahan, B., Luther, H.A., and Wilkes, J.O., Applied Numerical Methods, John Wiley and Sons, Inc., New York, 1969, pp. 574-584.

39. Weaver, W., "Finite Element Program PS2," unpublished notes for short course Finite Element Methods in Structural Mechanics, Stanford Univ., August, 1969.